ÓBUDA UNIVERSITY

Doctoral (Ph. D.) Dissertation

STUDY OF CARBON NANOFILLERS REINFORCED SILICON NITRIDE COMPOSITES

AWAIS QADIR

Supervisors:

Prof. Dr. Ján DUSZA

Dr. Péter PINKE

DOCTORAL SCHOOL OF MATERIALS SCIENCES & TECHNOLOGIES,
ÓBUDA UNIVERSITY

April 2021

Jury for Public Defense

President: Réger Mihály DSc.

Reviewers:

1. Szépvölgyi János DSc, Emeritus Professor, ELKH TTK
2. Marosné Berkes Mária PhD, ME GEIK ATI

Secretary: Horváth Richárd PhD, ÓE

Jury Members:

1. Orbulov Imre DSc, BME GK ATT
2. Károly Zoltán PhD, ELKH TTK
3. Takács Erzsébet DSc, Emeritus Professor, EK

Abstract in English

The presented work focuses on the mechanical and tribological properties of different kinds of – unoxidized monolithic, oxidized monolithic, and carbon nanofillers reinforced – silicon nitride composites. For the oxidized monolithic silicon nitride systems, α - Si_3N_4 as starting powders were oxidized at 1000 °C for 10 and 20 hours. This oxidation process developed a nanosized film of SiO_2 on the α - Si_3N_4 powder particles, which causes the nucleation of the Si_2N_2O phase in the matrix during the sintering process. In the case of carbon nanofillers composites, multiwalled carbon nanotubes (MWCNTs) and graphene nanoplatelets (GnPs) were used as reinforcement in the silicon nitride matrix. The starting powders were milled by the attritor mill equipped with zirconia balls and a zirconia-made agitator. Hot isostatic pressing (HIP) and gas pressure sintering (GPS) techniques were used to densify the powders. Following characterization techniques were used: Archimedes method for measuring the density, scanning electron microscopy (SEM) for examining the microstructure, X-ray diffraction (XRD) for phase analysis, transmission electron microscope (TEM), and high-resolution transmission electron microscope (HRTEM) for crystallographic structure analysis and confocal microscopy for calculating the material loss due to wearing after tribological tests. The fundamental mechanical properties and tribological properties of the investigated systems were determined. A fractographic analysis was carried out to determine the nature of the fracture. Wear tracks were examined by scanning electron microscope (SEM) to identify the wear mechanisms. Monolithic silicon nitride materials exhibited better mechanical properties as compared to the carbon nanofillers reinforced silicon nitride composites. Carbon nanofillers reinforced composites behaved very well in terms of tribological properties and showed a low wear rate. At the end of this work, possible solutions have been suggested to overcome the challenges which arise in developing silicon nitride composites.

Keywords: silicon nitride, multiwalled carbon nanotubes, graphene, hot isostatic pressing, mechanical properties, tribological properties

Abstract in Hungarian

Jelen dolgozat különböző - monolit, oxidált és szén nanorészecskékkel erősített - szilícium-nitrid kompozit mechanikai és tribológiai tulajdonságainak vizsgálatával foglalkozik. Az oxidált szilícium-nitrid-kompozitok esetében az α-Si_3N_4 por alapanyagokat 1000 ° C-on 10 és 20 órán át oxidáltuk. Az oxidációs folyamat nanoméretű SiO_2-film kialakulásához vezetett az α - Si_3N_4 szemcséken, amely a szinterelési folyamat során Si_2N_2O fázis nukleációját eredményezte. A szén nanorészecskékkel töltött kompozitok esetében a szilícium-nitrid mátrixban erősítőanyagként többfalú szén nanocsövet (MWCNT) és grafén nanolemezt (GnP) alkalmaztunk. A poranyagok őrlését attritor malomban hajtottuk végre cirkóniumgolyókkal, cirkónium-dioxid keverőanyag adagolása mellett. A poranyagok zsugorítására meleg izosztatikus sajtolást (HIP) és gáznyomású szinterelési (GPS) technikát alkalmaztunk. A vizsgálatok során a következő technikákat alkalmaztuk: Archimedes módszert a sűrűség mérésére, pásztázó elektronmikroszkópot (SEM) a mikroszerkezet vizsgálatára, röntgendiffrakciót (XRD) fáziselemzésre, transzmissziós elektronmikroszkópot (TEM) és nagy felbontású transzmissziós elektronmikroszkópot (HRTEM) a kristálytani szerkezetelemzéshez és konfokális mikroszkópot a tribológiai vizsgálatok utáni anyagveszteség megállapításához. Mérésekkel meghatároztam a kompozitok alapvető mechanikai és tribológiai tulajdonságait. Fraktográfiai elemzést végeztem a törési folyamat behatárolása céljából. A kopási nyomokat pásztázó elektronmikroszkóppal (SEM) vizsgáltam a kopási mechanizmus megállapítása érdekében. A monolit szilícium-nitrid anyagok jobb mechanikai tulajdonságokat mutattak, mint a szén nanorészecskékkel erősített szilícium-nitrid kompozitok. A szén nanorészecskékkel erősített kompozitok esetében kedvezőbb tribológiai tulajdonságokat és kisebb kopási sebességet mértem, mint a monolit kerámia esetében. A dolgozat záró részében megfogalmazásra került több javaslat a szilícium-nitrid-kompozitok fejlesztésével kapcsolatos további kutatásokkal összefüggésben.

Kulcsszavak: szilícium-nitrid, többfalú szén nanocsövek, grafén, meleg izosztatikus sajtolás, mechanikai tulajdonságok, tribológiai tulajdonságok

Dedications

This dissertation is affectionately dedicated to my Late parents – ***Qadir Bakhsh & Bakht***

Wadi *– brothers and sisters for their endless love, support, and encouragement*

Declaration

I declare that this thesis is my original work and effort. I acknowledged and cited adequately, where I used other sources of information.

Budapest, 21 April, 2021.

.....

Signature

Acknowledgement

Firstly, I would like to thank my Ph.D. supervisors **Professor Dr. Ján Dusza** and **Dr. Péter Pinke,** for accepting me as a Ph.D. student in a difficult time, and I consider it my fortune to have worked under their excellent guidance. I am also very grateful to my previous supervisors, **Dr. Csaba Balázsi** and **Dr. Katalin Balázsi**, for their superb supervision, advice, and support in the first two years of my Ph.D. This thesis could not have materialized without their impeccable support and encouragement. I am thankful to the Centre for Energy Research, Hungarian Academy of Sciences, for providing me facilities at the lab. Most of the work was done at the labs of the Hungarian Academy of Sciences. I am very grateful to all the colleagues, researchers, and technicians for their help and support. I am also thankful to the Institute of Materials Research (IMR), Slovak Academy of Sciences, for providing me the lab facilities to continue the remaining part of my Ph.D. I also thank **Viktor Varga**, **Levente Illés**, **Ing. Michal Ivor**, **Dr. Dávid Medved**, **Dr. Haroune Ben Zine**, **Dr. Zsolt Horváth Endre** and **Dr. Zsolt Fogarassy** for their valuable collaboration and technical assistance to perform experiments.

I acknowledge the financial support from Govt. of Hungary under the Stipendium Hungaricum Program. I acknowledge the composites' tribological study was supported by the ÚNKP-20-3 New National Excellence Program of The Ministry for Innovation and Technology from the source of the National Research, Development, and Innovation Fund.

I would like to thank my family back in Pakistan for giving me the strength, confidence, and instilled in me a scientific eagerness, and supported me heartedly to follow my dreams. Finally, I am grateful to Miss **Ferenczy Anna Júlia** and **Ferenczy's family** for their care and moral support during my studies and thesis writing. Thanks to **Anna Ferenczy,** who supported me throughout my Ph.D. studies and kept my motivation level up. Last but not least, I also thank my friends and colleagues, especially **Maryam Aslam, Dr. Hamza Khan**, **Saifullah Memon**, **Ahsan Khalid**, **Shoaib Ali**, **Saad Tariq**, **RituRaj**, **Dr. Yatish, Mahmud Al-bkree,** and **Sanjay Kumar.** Their best wishes were always with me during my Ph.D. journey.

Table of Contents

List of Symbols and Abbreviations

α	Alpha
β	Beta
CCVD	Catalytic chemical vapor deposition
CNTs	Carbon nanotubes
COF	Coefficient of friction
EDX	Energy dispersive X-ray
GNPs	Graphene nanoparticles
GO	Graphene oxide
GPa	Giga Pascal
GPLs	Graphene platelets
GPS	Gas pressure sintering
HIP	Hot isostatic pressing
HP	Hot pressing
HRTEM	High resolution transmission electron microscopy
H_V	Vickers Hardness
K_{IC}	Fracture toughness
K_{IIFR}	Indentation fracture resistance
MPa	Mega Pascal
MWCNTs	Multi-walled carbon nanotubes
PEG	Polyethylene glycol
rGO	Reduced graphene oxide
ρ_s	Apparent Density
SEM	Scanning electron microscopy
SEPB	Single edge pre-cracked beam
SEVNB	Single-edge-V-notched beam
Si_3N_4	Silicon nitride
Si_2N_2O	Silicon oxynitride
SPS	Spark plasma sintering
SWCNTs	Single-walled carbon nanotubes
TEM	Transmission electron microscopy
UMT	Universal Mechanical Tester

XRD	X-ray Diffraction

1. Introduction and objectives of the work

In 1859, Sainte-Claire Deville and F. Wohler reported the synthesis of Si_3N_4 for the first time by [1]. In 1955, J. F. Collins and R. W. Gerby found that silicon nitride-based ceramics have potential thermal and mechanical properties at high temperatures [2]. Simultaneously, the silicon nitride was not developed fully dense until then, and it was fabricated by a reaction bonding method only. In the 1960s, Deeley et al. [3] developed, for the first time, highly dense silicon nitride materials with sintering additives by hot pressing (HP). In the early 1970s, researchers focused on silicon nitride-based ceramics for gas turbine application [4]. Later on, different sintering techniques were developed, such as pressureless sintering [5] and gas pressure sintering (GPS) [6] which made it possible to produce complex-shaped components with high density. Silicon nitride is considered a structural ceramic material with several excellent properties such as excellent flexural strength, fracture resistance, high hardness, oxidation resistance, thermal properties at the room, and elevated temperatures. Despite having unique properties, silicon nitride also exhibits some negative properties, such as brittleness, low flaw tolerance, limited-slip systems, and low reliability, limiting its broader applications. To overcome such flaws, the addition of reinforcement in the silicon nitride matrix was proposed.

Another problem is the formation of amorphous glassy phases at grain boundaries of sintered silicon nitride. Due to covalent bonds and low solid-state diffusion in Si_3N_4, sintering is very difficult. Oxide additives such as Y_2O_3, Al_2O_3, CaO, MgO, etc., are used to provide conditions for liquid phase sintering of this ceramic material. These additives create liquid phases that enhance silicon nitride's densification and its transformation from the α-Si_3N_4 to the β-Si_3N_4 (Jack, 1976). Upon cooling, these liquid phases appear in the grain boundaries or at triple points of silicon nitride as amorphous oxide glasses. These glassy phases are detrimental to the mechanical properties of sintered silicon nitride at high temperatures. The glassy phases become soften at grain boundaries at a temperature above 1000 °C and affect the mechanical properties. These glassy phases are needed to eliminate or convert from amorphous to a crystalline phase which could play a role in improving properties at high temperature.

Many researchers developed silicon nitride with different reinforcements and achieved success to some extent. With the discovery of carbon nanotubes (CNTs) in 1991 and graphene in 2004, a new research horizon arose in the materials science field. Since their discoveries,

carbon nanofillers are being exploited to improve the mechanical, tribological, and electrical properties of advanced ceramics, including silicon nitride. The carbon nanofillers are promising candidates as reinforcements in the silicon nitride matrix to improve the composite properties.

Therefore, researchers utilize different carbon nanofillers with varying concentrations, adopting various milling methods and parameters and applying different sintering techniques with varying parameters to explore the mechanical, tribological, thermal, and functional properties of silicon nitride composites. The carbon nanofillers are not exploited well yet; there is still a need for much more focused research to exploit the nanofillers as reinforcement to improve silicon nitride's several properties.

The current work proposed that glassy phases might be eliminated or converted from amorphous to glassy phases by surface oxidation of silicon nitride's starting powders at high temperatures. The current work is also a contribution towards the exploration of silicon nitride's mechanical and tribological properties with the addition of carbon nanofillers. In this work, different techniques and parameters were adopted to optimize and obtain better results. The objectives of the current work are:

- To develop silicon nitride materials without glassy phases at the grain boundaries
- To study the effect of oxidation of starting powders on structural, mechanical, and tribological properties of sintered silicon nitride.
- To develop MWCNTs reinforced silicon nitride composites processed from oxidized α-Si_3N_4 powders and to study their mechanical and tribological properties.
- To investigate the microstructure of starting powders by scanning electron microscopy (SEM), transmission electron microscopy (TEM), and high-resolution transmission electron microscopy (HRTEM), and phases analysis by X-ray diffraction (XRD) technique.

The thesis work mainly consists of two parts – the theoretical part, which describes the literature, and the practical part, which illustrates the author's work about the development of composites, their testing, and results. ***Chapter 1*** describes a brief history of the development of silicon nitride and the problem and presents the main aims of the current work. ***Chapter 2*** is devoted to the theoretical background and literature review of silicon nitride and carbon nanofillers. It presents processing techniques, mechanical, tribological properties, and testing methods of silicon nitride-based composites. ***Chapter 3*** describes the experimental program, characterization techniques, and testing methods that were used for the current work. ***Chapter***

4 is the start of the experimental part of the thesis, and it deals with the development of monolithic silicon nitride systems. The chapter starts with the detailed method of oxidation of starting powders, preparation of composites, characterization of starting powders and sintered samples, mechanical properties, and tribological properties to identify wear mechanism. ***Chapter 5*** focuses on the preparation of MWCNTs reinforced Si_3N_4 composites, their mechanical and tribological properties. ***Chapter 6*** presents the brief results and discussions on graphene reinforced silicon nitride composites. Due to the limited time for this project, only the composites' tribological properties were done, and my colleagues have already published the other presented results. ***Chapter 7*** consists of a conclusion and the further challenges in developing silicon nitride composites with carbon nanofillers, which may help researchers in this field. ***Chapter 8*** comprises publications, conferences, and the impact of research. ***Chapter 9*** ends with the references used in this thesis work.

2. Theoretical Background and Literature Review

2.1. Advanced ceramic materials

In general, ceramics are non-metals that are hard, brittle, and heat resistant. Many definitions of ceramics are available in the literature. But most widely accepted definition of ceramics is presented by Kingery et al. [7]. According to them, the definition of ceramic is "*a ceramic is non-metallic, inorganic solid*." Based on production methods, properties, and application of ceramics, they can be classified into further classes (Figure 2.1):

1. traditional ceramics,
2. advanced ceramics.

Traditional ceramics are composed of clay minerals (e.g., porcelain, bricks, tiles, toilet bowls, and pottery), and they possess high hardness, extreme brittleness, and very susceptible to fracture. Advanced ceramics are also inorganic and non-metallic, but their microstructure is highly engineered to reflect its impact on ceramics' final mechanical properties. Grain size, grain shape, porosity, and phase compositions are carefully engineered to enhance the product's properties. Advanced ceramics are also called *engineering ceramics*, *technical ceramics*, *structural ceramics*, or *special ceramics*. Traditional ceramics have been using since the stone age, and advanced ceramics have been developed within the last 100 years. Ceramics is a multibillion dollars industry, and 17% of the sector is occupied by advanced ceramics [8].

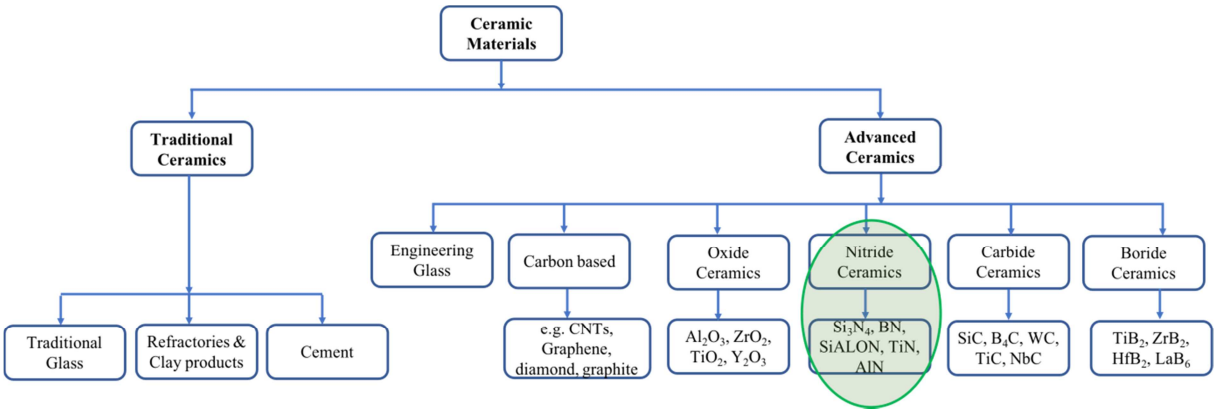

Figure 2.1 - Classification of ceramics based on processing and applications. The current work focuses on Si_3N_4 based ceramics which lie in the advanced ceramics class (highlighted by green circle) Author's work.

The advanced ceramics can be classified further based on their chemical composition (Figure 2.1.). Here, a brief introduction about the classified advanced ceramics will be presented, and the focus will be on Si_3N_4 based ceramics in the following chapters.

1. Oxide ceramics: these ceramics materials are based on metals or metalloids elements combined with oxygen—for example, Al_2O_3, ZrO_2, TiO_2, and Y_2O_3.
2. Nitride ceramics: nitride ceramics are a class of ceramics based on nitrogen combined with other elements—for instance, Si_3N_4, SiAlON, TiN, AlN.
3. Carbide ceramics: These are based on carbides, and SiC is one of the most important and widely used ceramic materials. e.g., SiC, B_4C, WC, TiC, NbC.
4. Boride Ceramics: Boride ceramics are a class of ceramics that have boron as one of the essential elements combined with rare earth elements or transition metals such as LaB_6, TiB_2, ZrB_2, HfB_2.

2.1.1. Silicon nitride (Si_3N_4)

Silicon nitride (Si_3N_4) is classified as an advanced structural ceramic with a high melting point, high hardness, and is relatively chemically inert. Si_3N_4 is the stoichiometric compound in the Si–N binary system [9]. Other silicon nitrides (Si_2N_3 [10], SiN [11], Si_3N [12], $Si(N_3)_4$) in this Si–N binary system have been reported, but their existence was considered doubtful. The calculated phase diagram of the Si–N system is given in Figure 2.2.

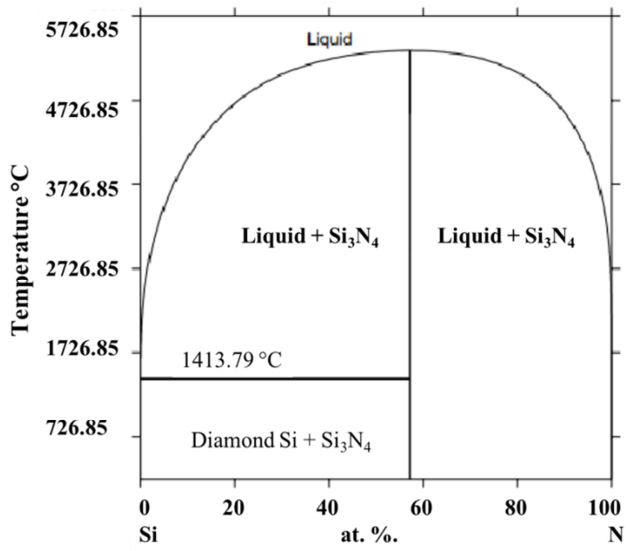

Figure 2.2 - Calculated phase diagram of Si-N system based on [9].

Si_3N_4 has three crystallographic structures at room temperature, which are named as α, β and ϒ. α and β are the most common crystallographic phases of silicon nitride and have

technological applications in advanced ceramics [13] [14]. Every crystallographic structure has its own characteristics whose presence influences the final properties of the silicon nitride composite. The ϒ phase of silicon nitride has a cubic structure, and therefore it is the hardest phase, with a value of up to 35 GPa, and is not widely used for structural applications [14][15]. The β phase has an elongated hexagonal structure and high toughness. The α phase has a trigonal structure and is harder than the β phase [15].

Silicon nitride-based materials have been used as cutting tools, bearings, sealings, parts of gas turbines, engines, etc., due to their exceptional combination of mechanical properties as flexural strength, hardness, resistance to oxidation, tribological and thermal properties [16]–[22].

2.2. Carbon-based nanostructures

The era of carbon nanostructure started with the discovery of fullerenes (C_{60}) in 1985 [23] [24]. Later, discoveries of carbon nanotubes (CNTs) by Ijima [25] and graphene by Geim and Novoselov [26] strengthened further development in carbon nanotechnology. Due to the importance, the discovery of two (fullerenes, graphene) of the carbon nanostructures got Nobel prizes. A new horizon of research opened up, and the properties of carbon nanostructures were exploited to develop novel materials in the last two decades.

Based on structure, carbon nanostructures can be divided into further types, as illustrated in Figure 2.3:

1. Fullerene,
2. Carbon nanotubes (CNTs),
3. Graphene,
4. Diamond-like carbon.

Here, only carbon nanotubes and graphene will be discussed.

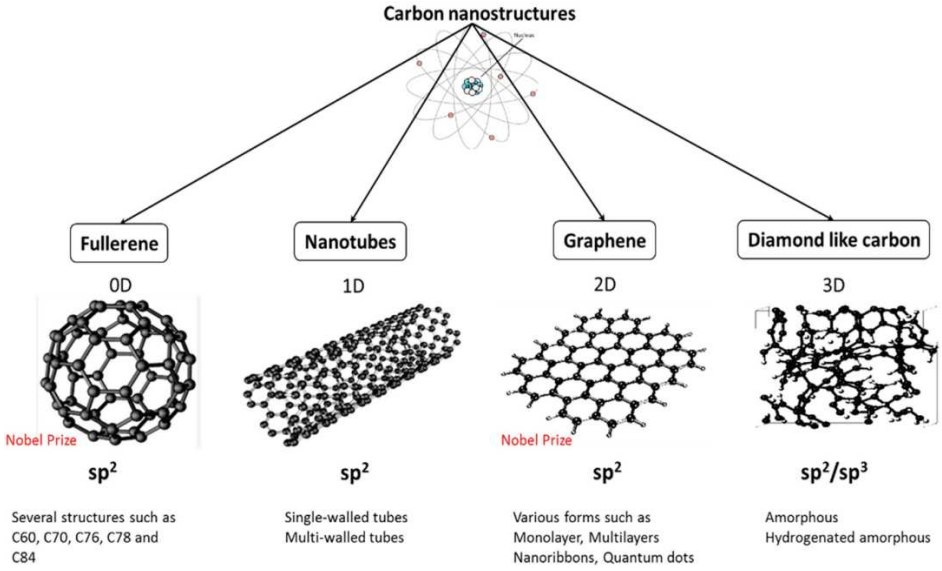

Figure 2.3 - Type of carbon-based nanostructures and classified based on sp-hybridization and 0D to 3D [23].

2.2.1. Carbon nanotubes

During the production of carbon C60 and fullerene by arc evaporation of graphite, Ijima examined the deposited carbon layer on the graphite by a high-resolution transmission electron microscope (HRTEM) [25]. He discovered a new form of carbon, which consisted of a graphene cylindrical tube with 10 nm diameter, and the end-cap was like a fullerene structure. This new form of carbon was named a carbon nanotube (CNT) based on its physical appearance. A CNT has three basic orientations (Figure 2.4) [27]:

Armchair orientation: Graphene cylinder along a five-fold axis with a fullerene-like cap at the end (Figure 2.4-a).

Zigzag orientation: Graphene cylinder along a three-fold axis with a fullerene-like cap at the end (Figure 2.4-b).

Chiral orientation: Graphene cylinder along with a helical arrangement with a fullerene-like cap at the end (Figure 2.4-c).

Carbon nanotubes (CNTs) are classified into two groups: multi-walled carbon nanotubes (MWCNTs) and single-walled carbon nanotubes (SWCNTs) [28]. MWCNTs consist of multiple concentric graphene cylinders, while SWCNTs comprise a single layer of a graphene cylinder. The diameter of CNT ranges between 1 and 50 nm, and the length ranges from a few nm to a few µm [29][30][31][32]. A CNT has a tensile strength 10 times greater than that of steel, and its stiffness is 15 times higher than that of steel (Table 2.1). The comparison of the properties of different materials is given in Table 2.1.

Table 2.1 - Comparison of properties of CNT and other materials. Reproduced from [33]

Material	Density (g/cm^3)	Tensile Strength (GPa)	Stiffness (GPa)
CNTs	1.3–2	10–60	1000
Wood	0.6	0.008	16
Steel	7.8	0.4	208
Carbon Fiber	1.7–2.2	1.7–3.3	200–960
Epoxy	1.25	0.005	3.5

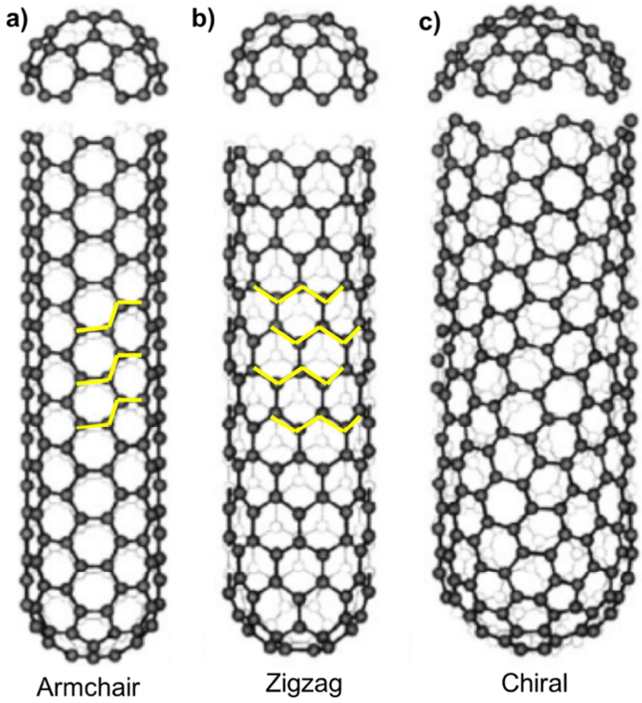

*Figure 2.4 - Three types of carbon nanotubes (CNTs): (**a**) armchair (n, m) = (5, 5); (**b**) zigzag (n, m) = (9, 0); (**c**) chiral (n, m) = (10, 5) [27].*

CNTs can be produced in two main ways:

(i) Arc Evaporation Method: A 50 Ampere current is applied between graphite electrodes to evaporate the graphite, and this is done in a helium environment. CNTs are condensed at the cathode. Ijima also used this method to produce CNTs [25]. This method can produce SWCNTs with the addition of Ni and Co at graphite anode electrode [33].

(ii) Catalytic Method: CNTs are produced by the decomposition of hydrocarbons over the metallic catalysts (Fe, Co, Ni) [34][35]. This method has the one disadvantage that CNTs are produced with lattice defects more than that of the arc evaporation method. These defects can be reduced by heat treatment after production [36].

2.2.2. Graphene

Graphene is a 2D single and thin layer of graphite with sp^2 hybridization arranged in hexagons. Graphite is an allotrope of carbon; graphite and graphene contain the same atoms, but a different arrangement of atoms gives different properties. In 2004, Andre Geim and Konstantin Novoselov discovered graphene by using scotch tape to polish a large block of graphite; the researchers spotted very thin flakes on the tape [37]. They continuously peeled layer by layer from the flakes of graphite and fabricated a thin sample layer as a single layer of graphite, which is now called graphene. The structure of graphene is illustrated in Figure 2.5.

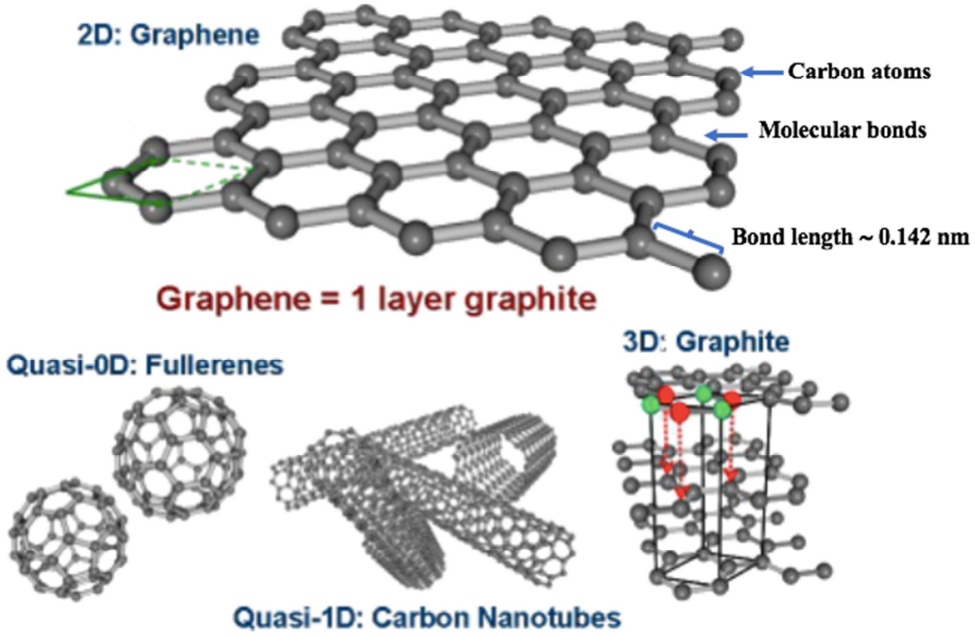

Figure 2.5 - Honeycomb lattice of graphene. Graphene layers can be stacked into graphite or rolled up into carbon nanotubes [38].

Due to the strength of its carbon bonds, graphene is the strongest material, with a tensile strength of 130 GPa and Young's modulus close to 1 TPa [39] [40]. The Class for Physics of the Royal Swedish Academy of Sciences enlightened in their Nobel Prize announcement that a 1 m^2 graphene hammock would support a cat of 4 kg but would weigh only as much as one of the cat's whiskers, at 0.77 mg, which is about 0.001% of the weight of 1 m^2 of a paper [41]. They also illustrated that graphene is more than 100 times stronger than the strongest steel [41].

2.3. Silicon nitride-based composites with carbon nanofillers reinforcement

To enhance the properties, several studies have been done on the carbon nanofillers reinforced silicon nitride composites. To some extent, the addition of carbon nanostructures was useful to enhance the mechanical, tribological, and electrical properties. The use of carbon nanostructures has not been exploited well because of the challenges in integrating nanostructures in the silicon nitride matrix. The main problems are non-uniform dispersion of reinforcement, incomplete densification, and porosity induced by the nanostructures. There is still a need to work done to address such problems.

However, Si_3N_4 is a structural ceramic material with many excellent properties, but at the same time, it has some negative properties which limit its applications in many sectors. The negative properties are brittleness, low flaw tolerance, and limited-slip systems. To overcome these negative characteristics, researchers proposed an idea to develop a composite by combining the properties of two or more constituents by adding a second phase to the silicon nitride matrix. The second phase should have such properties whose combination could give an optimum property. An improvement was achieved to some extent, but many challenges came up as well. Different silicon nitride-based composites have been developed with fine-grained matrix and ex-situ or in-situ introduced elongated β-Si_3N_4 grains [42]–[45].

One of the positive effects is the toughening mechanism induced by the CNTs and graphene. Several researchers reported the enhancement of fracture toughness of the composite with the addition of carbon nanotubes and graphene than that of monolithic material [46]–[49] [50]–[52].

Pasupuleti et al. [46] prepared 1 wt% CNTs reinforced Si_3N_4 composites by hot pressing (HP) technique. They reported an increase in fracture toughness with the addition of CNTs, which is because of the toughening mechanism by crack-bridging and pulling-out effect of CNTs. Moreover, R-curve behavior increased with the addition of CNTs, which enhance the composite's toughening behavior. So far, Matsuoka et al. [47] have also reported the highest value of fracture toughness (8.6 $MPa \cdot m^{1/2}$) of 1 wt% MWCNT-reinforced silicon nitride composite.

But some researchers also reported a decrease in fracture toughness of silicon nitride with the addition of CNTs [53][54]. Kovalcıkova et al. [53] reported a decrease in hardness and toughness of silicon nitride composite due to the high level of porosity, which was induced by the addition of MWCNTs.

Walker et al. [51] developed a uniform and homogeneously dispersed graphene platelets (GPLs) reinforced silicon nitride composites by spark plasma sintering. The reported significant increase in fracture toughness with a value of 6.6 MPa.m$^{1/2}$ for 1.5 vol% GPLs reinforced Si_3N_4 than that of monolithic silicon nitride material. The increase in fracture toughness is attributed to the toughening mechanisms in the form of graphene necking, crack bridging, crack deflection, and pull-out. The observed toughening mechanisms by graphene platelets are evidenced by SEM image (Figure 2.6)

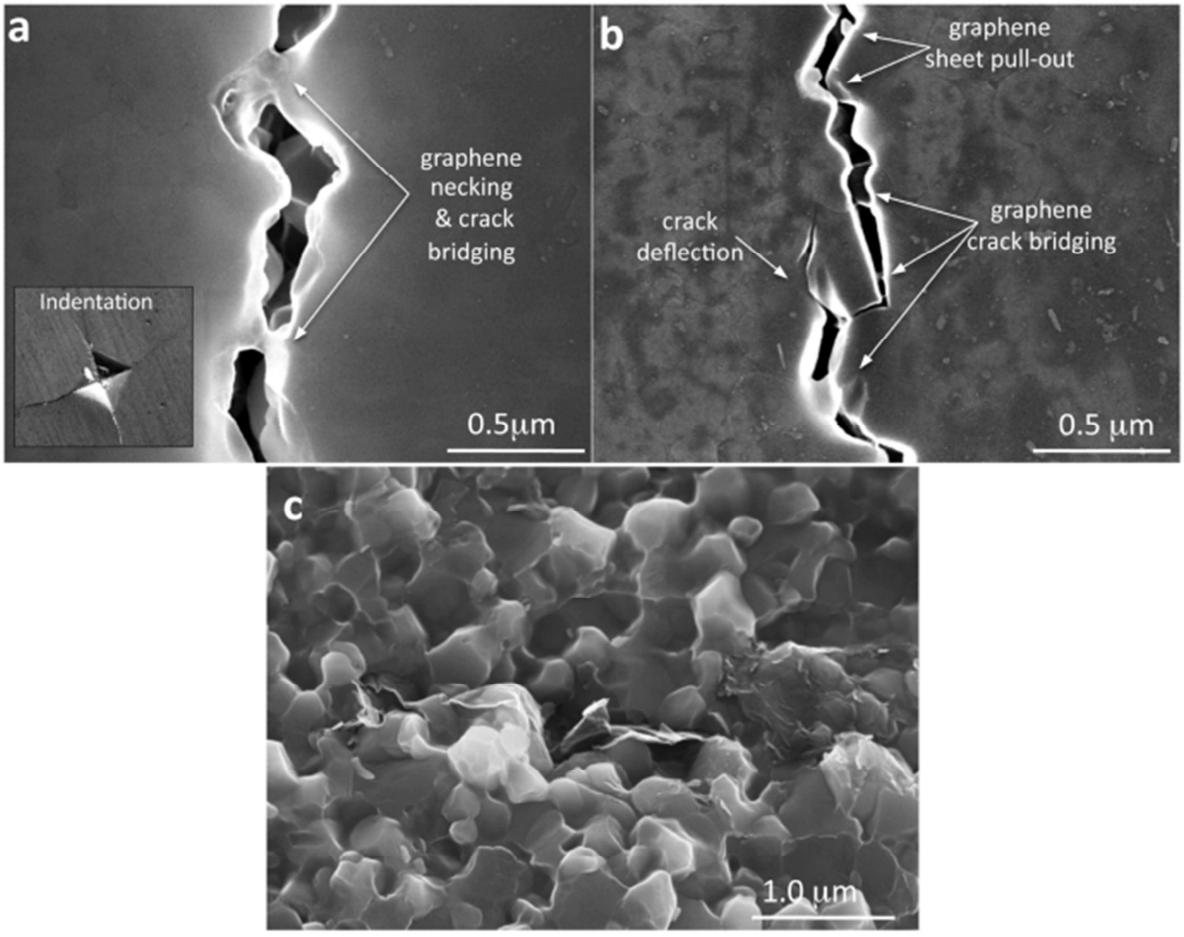

Figure 2.6 - Toughening mechanisms in GPL-Si_3N_4 nanocomposites. (a) Microhardness testing resulting in the creation of radial cracks stemming from the microhardness indent. Closer examination of the radial cracks reveals GPL bridging the crack at several locations, two of which are shown in this high-resolution SEM image. (b) Further examination of the radial cracks indicates that they follow a tortuous crack propagation path. (c) Fracture surface of the bulk sample indicates the presence of three-dimensional toughening mechanisms for the GPL-Si_3N_4 nanocomposite [51].

Despite the positive effect of carbon nanostructures' addition, several challenges have to be dealt such as preservation of reinforcements, interfacial bonding between matrix and reinforcements, uniform dispersion, load transferability, and amount of reinforcement.

Effective load transfer plays a role in enhancing the toughness, and it depends on the interfacial strength between CNTs and silicon nitride grains. Without the optimum interfacial strength, the effective load transfer is not possible, which leads to the diminishing of crack-bridging and pulling-out mechanisms on the fracture surface.

It is difficult to compare the influence of graphene and CNTs on the properties of Si_3N_4-based composites because of limited and ambiguous results reported in the literature. Tables 2.2 and 2.3 comprise the effect of CNT/graphene on the mechanical and tribological properties of silicon nitride. Only selected results from the literature have been presented in tables 2.2 and 2.3. Both CNTs and Graphene are promising candidates to enhance ceramics' mechanical, tribological, and functional properties.

Table 2.2 – Mechanical properties of carbon nanofillers reinforced silicon nitride with processing parameters from literature.

Si_3N_4 +	Milling Parameter	Sintering Parameters	Sintering Additives	Theoretical/ Apparent Density (g/cm^3)	Load (N)	HV (GPa)	Flexural Strength (MPa)	K_{IC} ($MPa \cdot m^{1/2}$)	Ref.
1 wt% MWCNTs	Planetary	GRF/1000~1450 °C/40 h + 550 °C/2 h	MgO, Al_2O_3, SiO_2	89.4 %	-	8.2	280	2.3	[55]
1 wt% MWCNTs	Ball/3 h	SPS/1500 °C/5 min/50 MPa	Al_2O_3, Y_2O_3	3.17 g/cm^3	10	16.6 ± 0.4	~279	5.3	[56]
1 wt% MWCNTs	Ball/24 h	HP/1750 °C /1 h/30 MPa	Al_2O_3, Y_2O_3, ZrO_2	98.7 %	98	15.0 ± 0.1	996 (4 pt.)	6.6 ± 0.6	[46]
3 wt% MWCNTs	Attritor/5 h	HIP/1700 °C/ 3 h/20 MPa	Al_2O_3, Y_2O_3	-	98	10.41			[48]
3 wt% MWCNTs	Attritor/5 h	SPS/1650 °C/3–5 min/50 MPa	Al_2O_3, Y_2O_3	-	98	18.73			
3 wt% SWCNTs	Attritor/5h	SPS/1650°C/3–5 min/50 MPa	Al_2O_3, Y_2O_3	-	98	16.97			
5 wt% MWCNTs	Ball/16 h	HP/1700 °C/1 h/ 30 MPa	Al_2O_3, Y_2O_3	-	29	~13.75	525	6.7	[49]
1 wt% MWCNTs	Ball/3 h	SPS/1500 °C/5 min/100 MPa	Y_2O_3, Al_2O_3	3.17 g/cm^3	-	16.6			[57]
1 wt% MWCNTs	Ball/3 h	SPS/1500 °C/3 min/50 MPa	Y_2O_3, Al_2O_3	3.19 g/cm^3	-	19.1			
1 wt% MWCNTs	Bead/2 h	GPS/1600–1750 °C/2 h + HIP/1700°/1 h/100 MPa	Y_2O_3, Al_2O_3, AlN. HfO_2, TiO_2	99.6 %	98	14.8	~980	7.1	[47]
1 wt% MWCNTs	Ball/24 h	GPS/1600–1750 °C/2 h + HIP/1700°/1 h/100 MPa	Y_2O_3, Al_2O_3, AlN. HfO_2, TiO_2	93.5 %	98	11.3	834	8.6	
1 vol% SWCNTs	Ball/12 h	SPS/1600 °C/3 min	CTAB *	95.4 %	2.45	17.6			[58]
6 vol% SWCNTs	Ball/12 h	SPS/1600 °C/3 min	CTAB *	91.0 %	2.45	10.7			
0 wt% GNP	Ball/25 min	HP/1650 °C/ 2h/ 40 MPa	AlF_3, MgF_2	3.079	10	15.61	516	5.08	[59]
1 wt% GNP	Ball/25 min	HP/1650 °C/ 2h/ 40 MPa	AlF_3, MgF_2	3.071	10	18.76	593	8.48	
2 wt% GNP	Ball/25 min	HP/1650 °C/ 2h/ 40 MPa	AlF_3, MgF_2	3.07	10	18.89	617	11.26	
3 wt% GNP	Ball/25 min	HP/1650 °C/ 2h/ 40 MPa	AlF_3, MgF_2	3.74	10	18.62	599	9.51	

Si_3N_4 +	Milling Parameter	Sintering Parameters	Sintering Additives	Theoretical/ Apparent Density (g/cm^3)	Load (N)	HV (GPa)	Flexural Strength (MPa)	K_{IC} ($MPa \cdot m^{1/2}$)	Ref.
0 wt% rGO	Ball/2h h	HP/ 1700°C/1h/30MPa	Y_2O_3, Al_2O_3	99.79	196	16.6	608	6.17	[60]
0.75 wt% rGO	Ball/2h h	HP/ 1700°C/1h/30MPa	Y_2O_3, Al_2O_3	99.92	196	18.6	784	7.63	
1.50 wt% rGO	Ball/2h h	HP/ 1700°C/1h/30MPa	Y_2O_3, Al_2O_3	99.51	196	17.9	962	9.26	
2.25 wt% rGO	Ball/2h h	HP/ 1700°C/1h/30MPa	Y_2O_3, Al_2O_3	99.06	196	17.3	1116.4	10.3	
0 wt% GNP	Ball mill/-	SPS/1700°C/10 min/vacuum	Y_2O_3, Al_2O_3	3.31	98	17.5	-	5.1	[61]
3 wt% GNP	Ball mill/-	SPS/1700°C/10 min/vacuum	Y_2O_3, Al_2O_3	3.27	98	13.5	-	6.6	
5 wt% GNP	Ball mill/-	SPS/1700°C/10 min/vacuum	Y_2O_3, Al_2O_3	3.21	98	12.8	-	7.5	
3 wt% FL-GNP	Ball mill/-	SPS/1700°C/10 min/vacuum	Y_2O_3, Al_2O_3	3.29	98	13.7	-	10.5	
5 wt% FL-GNP	Ball mill/-	SPS/1700°C/10 min/vacuum	Y_2O_3, Al_2O_3	3.29	98	9.8	-	7.6	
0 vol% GNP	Ball mill/2h	SPS/1700°C/10 min/vacuum	Y_2O_3, Al_2O_3	3.23	9.8	20.4	~950	~4.5	[62]
4.3 vol% GNP	Ball/2h	SPS/1625°C/5 min/50 MPa	Y_2O_3, Al_2O_3	3.18	9.8	17.7	~925	~6.5	
7.2 vol% GNP	Ball/2h	SPS/1625°C/5 min/50 MPa	Y_2O_3, Al_2O_3	3.16	9.8	16.4	-	~5.5	
4.3 vol% rGO	Ball/2h	SPS/1625°C/5 min/50 MPa	Y_2O_3, Al_2O_3	3.19	9.8	15.9	~1040	~10	
7.2 vol% rGO	Ball/2h	SPS/1625°C/5 min/50 MPa	Y_2O_3, Al_2O_3	3.16	9.8	14.6	-	~9.2	
0 wt%	Attritor/5h	SPS/1600°C/10 min/50 MPa	Y_2O_3, Al_2O_3	~98.2%	19.6	17.5	-	5.4	[63]
1 wt% MLG	Attritor/5h	SPS/1600°C/10 min/50 MPa	Y_2O_3, Al_2O_3	~97.60	19.6	18.4	-	4.4	
3 wt% MLG	Attritor/5h	SPS/1600°C/10 min/50 MPa	Y_2O_3, Al_2O_3	~97.25	19.6	15.2	-	4.9	
5 wt% MLG	Attritor/5h	SPS/1600°C/10 min/50 MPa	Y_2O_3, Al_2O_3	~97.09	19.6	13.7	-	5.4	
0 wt% GPLs	Ball/12h	HP/1750°C/1h/20 MPa	Y_2O_3, Al_2O_3, MgO	3.1			296	5.32	[52]
0.2 wt% GPLs	Ball/12h	HP/1750°C/1h/20 MPa	Y_2O_3, Al_2O_3, MgO	3.14			305	5.86	
2 wt% GPLs	Ball/12h	HP/1750°C/1h/20 MPa	Y_2O_3, Al_2O_3, MgO	3.06			270	1.87	
0 wt% MLG	Attritor/5h	SPS/1600°C/10min/50 MPa	Y_2O_3, Al_2O_3	~98%	19.6	~17.5		~5.3	[64]
1 wt% MLG	Attritor/5h	SPS/1600°C/10min/50 MPa	Y_2O_3, Al_2O_3	~96.5%	19.6	~18.37		~4.8	
3 wt% MLG	Attritor/5h	SPS/1600°C/10min/50 MPa	Y_2O_3, Al_2O_3	~93.8%	19.6	~15.25		~4.8	

Si_3N_4 +	Milling Parameter	Sintering Parameters	Sintering Additives	Theoretical/ Apparent Density (g/cm^3)	Load (N)	HV (GPa)	Flexural Strength (MPa)	K_{IC} ($MPa \cdot m^{1/2}$)	Ref.
								7	
5 wt% MLG	Attritor/5h	SPS/1600°C/10min/50 MPa	Y_2O_3, Al_2O_3	~90.1%	19.6	~13.80		~5.0	
3 wt% MLG	Attritor/4.5h	HIP/1700 °C/ 3 h/20 MPa	Y_2O_3, Al_2O_3	2.8 (88.6%)	5	5.8 ± 0.65		5.7	[65]

Table 2.3 – Tribological properties of carbon nanofillers reinforced silicon nitride with the processing parameters from literature.

Si_3N_4 +	Milling Parameter	Sintering Parameters	Sintering Additives	Theoretical/Apparent Density (g/cm^3)	Load (N)	Test Conditions	Wear rate	Ref.
0 wt% MWCNTs	Attritor/5h	HIP/1700°C/3h/20 MPa	Y_2O_3, Al_2O_3	-	5	Dry	~ 1.10×10^{-5}	[66]
1 wt% MWCNTs	Attritor/5h	HIP/1700°C/3h/20 MPa	Y_2O_3, Al_2O_3	-	5	Dry	~ 2.0×10^{-5}	
3 wt% MWCNTs	Attritor/5h	HIP/1700°C/3h/20 MPa	Y_2O_3, Al_2O_3	-	5	Dry	~ 4.9×10^{-5}	
5 wt% MWCNTs	Attritor/5h	HIP/1700°C/3h/20 MPa	Y_2O_3, Al_2O_3	-	5	Dry	~ 1.10×10^{-5}	
10 wt% MWCNTs	Attritor/5h	HIP/1700°C/3h/20 MPa	Y_2O_3, Al_2O_3	-	5	Dry	~ 8.0×10^{-5}	
0 vol% MWCNTs	Ultrasonic stir	SPS/1585°C/5min/50 MPa	Y_2O_3, Al_2O_3	3.23	50	Isooctane lubricant	~ 0.61×10^{-6}	[67]
1.8 vol% MWCNTs	Ultrasonic stir	SPS/1585°C/5min/50 MPa	Y_2O_3, Al_2O_3	3.20	50	Isooctane lubricant	~ 0.47×10^{-6}	
5.3 vol% MWCNTs	Ultrasonic stir	SPS/1585°C/5min/50 MPa	Y_2O_3, Al_2O_3	3.15	50	Isooctane lubricant	~ 0.33×10^{-6}	
8.6 vol% MWCNTs	Ultrasonic stir	SPS/1585°C/5min/50 MPa	Y_2O_3, Al_2O_3	3.12	50	Isooctane lubricant	~ 0.16×10^{-6}	
0 wt% MWCNTs	Attritor/5h	HIP/1700°C/3h/20 MPa	Y_2O_3, Al_2O_3	-	5	Dry	~ 3.02×10^{-6}	[68]
3 wt% MWCNTs	Attritor/5h	HIP/1700°C/3h/20 MPa	Y_2O_3, Al_2O_3	-	5	Dry	~ 3.34×10^{-7}	
0 wt% MWCNTs	Attritor/5h	HIP/1700°C/3h/20 MPa	Y_2O_3, Al_2O_3	-	5	Dry	~ 1.8×10^{-7}	[69]

Si_3N_4 +	Milling Parameter	Sintering Parameters	Sintering Additives	Theoretical/Apparent Density (g/cm^3)	Load (N)	Test Conditions	Wear rate	Ref.
1 wt% MWCNTs	Attritor/5h	HIP/1700°C/3h/20 MPa	Y_2O_3, Al_2O_3	-	5	Dry	~ 3.5×10^{-5}	
3 wt% MWCNTs	Attritor/5h	HIP/1700°C/3h/20 MPa	Y_2O_3, Al_2O_3	-	5	Dry	~ 0.9×10^{-5}	
10 wt% MWCNTs	Attritor/5h	HIP/1700°C/3h/20 MPa	Y_2O_3, Al_2O_3	-	5	Dry	~ 8.05×10^{-5}	
0 wt% GNP	Attritor/5h	SPS/1700°C/10min	Y_2O_3, Al_2O_3	3.32	5	Dry	~ 1.2×10^{-5}	[70]
3 wt% GNP	Attritor/5h	SPS/1700°C/10min	Y_2O_3, Al_2O_3	3.28	5	Dry	~ 9.8×10^{-6}	
3 wt% FL-GNP	Attritor/5h	SPS/1700°C/10min	Y_2O_3, Al_2O_3	3.3	5	Dry	~ 6.5×10^{-6}	
5 wt% FL-GNP	Attritor/5h	SPS/1700°C/10min	Y_2O_3, Al_2O_3	3.13	5	Dry	~ 2.1×10^{-7}	
0 wt% GNP	Ball/2h	SPS/1625°C/5min/50 MPa	Y_2O_3, Al_2O_3	3.23	50	Isooctane lubricant	~ 6.94×10^{-8}	[71]
3 wt% GNP	Ball/2h	SPS/1625°C/5min/50 MPa	Y_2O_3, Al_2O_3	3.18	50	Isooctane lubricant	~ 5.83×10^{-8}	
0 wt% GNP	Ball/2h	SPS/1625°C/5min/50 MPa	Y_2O_3, Al_2O_3	3.23	100	Isooctane lubricant	~ 5.0×10^{-8}	
3 wt% GNP	Ball/2h	SPS/1625°C/5min/50 MPa	Y_2O_3, Al_2O_3	3.18	100	Isooctane lubricant	~ 3.33×10^{-8}	
0 wt% GNP	Ball/2h	SPS/1625°C/5min/50 MPa	Y_2O_3, Al_2O_3	3.23	200	Isooctane lubricant	~ 4.86×10^{-8}	
3 wt% GNP	Ball/2h	SPS/1625°C/5min/50 MPa	Y_2O_3, Al_2O_3	3.18	200	Isooctane lubricant	~ 2.06×10^{-8}	
0 wt% MLG	Attritor/5h	HIP/1625°C/3h/20 MPa	Y_2O_3, Al_2O_3	-	5	Dry	~ 7.5×10^{-6}	[72]
1 wt% MLG	Attritor/5h	HIP/1625°C/3h/20 MPa	Y_2O_3, Al_2O_3	-	5	Dry	~ 7.0×10^{-6}	
3 wt% MLG	Attritor/5h	HIP/1625°C/3h/20 MPa	Y_2O_3, Al_2O_3	-	5	Dry	~ 2.4×10^{-5}	

2.3.1. Effect of carbon nanofillers on hardness

The effect of CNTs and graphene on silicon nitride composites' microhardness is not positive as the positive effect on fracture toughness, electrical and tribological properties. According to the results, the hardness values are in a strong relationship with the values of densities. Due to the tendency of agglomeration of CNTs and graphene, the porosity of silicon nitride-based composites increased. Balazsi et al. [73] reported decreased Vickers hardness of silicon nitride composites with increasing amount of multi-layered graphene (MLG). The hardness increased with the addition of 1 wt% MLG and then started decreasing with the higher amount of MLG. The decrease in Vickers hardness attributed to the soften-carbon parts and high porosity because of the addition of MLG. Similarly, in CNTs added silicon nitride, the decreasing tendency in microhardness has been observed. More study is needed to understand the negative phenomenon of carbon nanofillers on the hardness of silicon nitride.

Recently, Hu et al. [60] reported the addition of reduced graphene (rGO) sheets to Si_3N_4 results in superior mechanical properties to a monolithic Si_3N_4. They prepared a novel reduced graphene oxide-encapsulated silicon nitride (Si_3N_4@rGO) particle via electrostatic interaction between amino-functionalized Si_3N_4 particles and graphene oxide (GO). The improvement in Vickers hardness is attributed to the refined microstructure of the composites. The addition of rGO leads to microstructure refinement, which increased the hardness by hindering the silicon nitride grains' dislocation.

2.3.2. Effect of carbon nanofillers on flexural strength

The flexural strength of CNTs and graphene added silicon nitride composites is comparable with the strength of the monolithic material. No significant improvement in flexural strength has been reported so far. Technological and surface defects such as clusters of reinforcements, impurities, pores, and non-densified areas cause the fracture origin. In service under loads, these defects serve as a fracture origin and decrease the strength as per their character, size, and location in the microstructure.

But some studies found a slight improvement in flexural strength, but the reason behind the improvement is still not clear. Balazsi et al. [57] developed the silicon nitride composite with 1 wt% of MWCNTs, and the bending strength was found to be higher than that of silicon nitride without MWCNTs. By pulling out, the MWCNTs' strengthening mechanism was observed in the composite [57]. Yoshio et al. [74] reported that bead milling results in well-

pulverized agglomerates of CNTs, uniformly dispersed in ethanol, and prepared Si_3N_4 + CNT ceramics in such a way, and the bending strength was improved.

Hu et al. [60] reported 83.5% increased flexural strength and reached a maximum value of 1116.4 MPa, and the fracture toughness increased by 67.7% to 10.35 $MPa \cdot m^{1/2}$ with the addition of 2,25 wt% rGO as reinforcement in the silicon nitride matrix.

2.3.3. Effect of carbon nanofillers on tribological properties

The carbon nanostructures have attracted much attention to be used as self-lubricating nanofillers in silicon nitride composites working under severe friction and wear conditions. The tribological study of graphene added ceramics started in 2013 after the publication by Hvizdos et al. [72] and Belmonte et al. [71]. Hvizdos et al. [72] studied mechanical and tribological properties of nanocomposites with silicon nitride matrix with the addition of 1 and 3 wt% of various types of graphene platelets. They observed that 1 wt% graphene phase does not lower the coefficient of friction in dry conditions but, 3 wt% of larger sized graphene reinforced showed higher wear resistance. Belmonte et al. [71] investigated the tribological properties of graphene nanoplatelets (GNPs)/Si_3N_4 composites using a reciprocating ball-on-plate configuration under isooctane lubrication. They observed that exfoliated graphene nanoplatelets formed an adhered protective tribofilm, which acted as lubrication and enhanced up to 56% wear resistance.

Similarly, CNTs are also beneficial to enhance the tribological properties of silicon nitride composites. Gonzalez-Julian et al. [67] found the better tribological properties in terms of low wear rate with the addition of 8.6 vol% MWCNT in silicon nitride matrix than the monolithic Si_3N_4 ceramics under the load of 50 N in isooctane lubrication condition. The improved wear properties were attributed to the homogeneous dispersion of CNTs and the extra effect of lubrication by CNTs. It was observed that Si_3N_4 + MWCNT composites showed 40% lower friction coefficient and 80% lower wear rates than that of the monolithic silicon nitride materials.

Balko et al. [69] prepared the silicon nitride composite with 1, 3, 5, and 10 wt% of multi-walled carbon nanotubes (MWCNTs) at 1700 °C by the HIP sintering technique. They performed the tribological tests on these composites using a ball on desk configuration in dry conditions. Notably, 1 and 3 wt% of MWCNTs did not significantly decrease the coefficient of friction and wear rate, but the MWCNTs higher than 5 wt% had a positive effect in

reducing the wear rate and coefficient of friction (COF). Besides, 10 wt% MWCNT-reinforced Si_3N_4 reduced the coefficient of friction (COF) by 46% compared to that of 1 wt%.

There are some models and wear maps developed by researchers which can be simulated to predict the wear characteristics of a material. Maros et al. [75] developed the 2D and 3D wear maps for multi-layered graphene (MLG) added Si_3N_4 composites which help the researchers to predict the wear performance of the composites under various loading and different speed conditions.

In monolithic silicon nitride ceramics, the general wear mechanism is that the grains are detached from the surface during the sliding. These grains cause the abrasion and pronounce the effect of wearing. In general, wear debris is formed by the action of the micro-abrasion mechanism, being compacted during the motion of the sliding pairs. If CNTs are present in the debris wear, then the debris wear serves as lubrication and overcomes friction. One of the examples was observed by Gonzalez-Julian et al. [76] in situ CNTs + Si_3N_4 composites; the debris areas appeared well adhered to the surface, which protected it against wear [76].

2.4. Processing of ceramic matrix composites

It is difficult to sinter Si_3N_4 to achieve full density due to covalent bonds between Si and N atoms. The processing of carbon nanostructures based on Si_3N_4 composites is even more difficult because of integrating a reinforcement phase at the nanometric scale; therefore, the processing routes have to be optimized before manufacturing the Si_3N_4 + CNT/graphene composites. The main processing routes of a Si_3N_4 + carbon nanostructures (CNTs/graphene) composite are schematically illustrated in Figure 2.7, in which the powder preparation phase before sintering can be in the form of:

(i) Powder processing
(ii) Colloidal Processing
(iii) Sol-gel/precursor (in situ growth of CNTs/graphene).

After the processing route of starting powders, the next step is to consolidate the powders into a shaped preform under dry pressing called a green sample, green body, or green compact. The last step is densifying these green bodies by utilizing heating or application of temperature and pressure to allow the bonding reaction between powder particles to achieve full density; this process is called the sintering process. For the sintering process, several techniques (i.e., hot pressing, hot isostatic pressing, gas pressure sintering, and spark plasma

sintering) have been applied to densify the silicon nitride-based powders. As it was mentioned above, sinter silicon nitride powders to achieve full density is difficult. Sintering aids require to aid in the sintering process to achieve full density. Many sintering aids have been used to improve the sintering process. In addition to the positive influence, the sintering additives have a negative aspect; they segregate at grain boundaries and negatively affect the high-temperature mechanical properties.

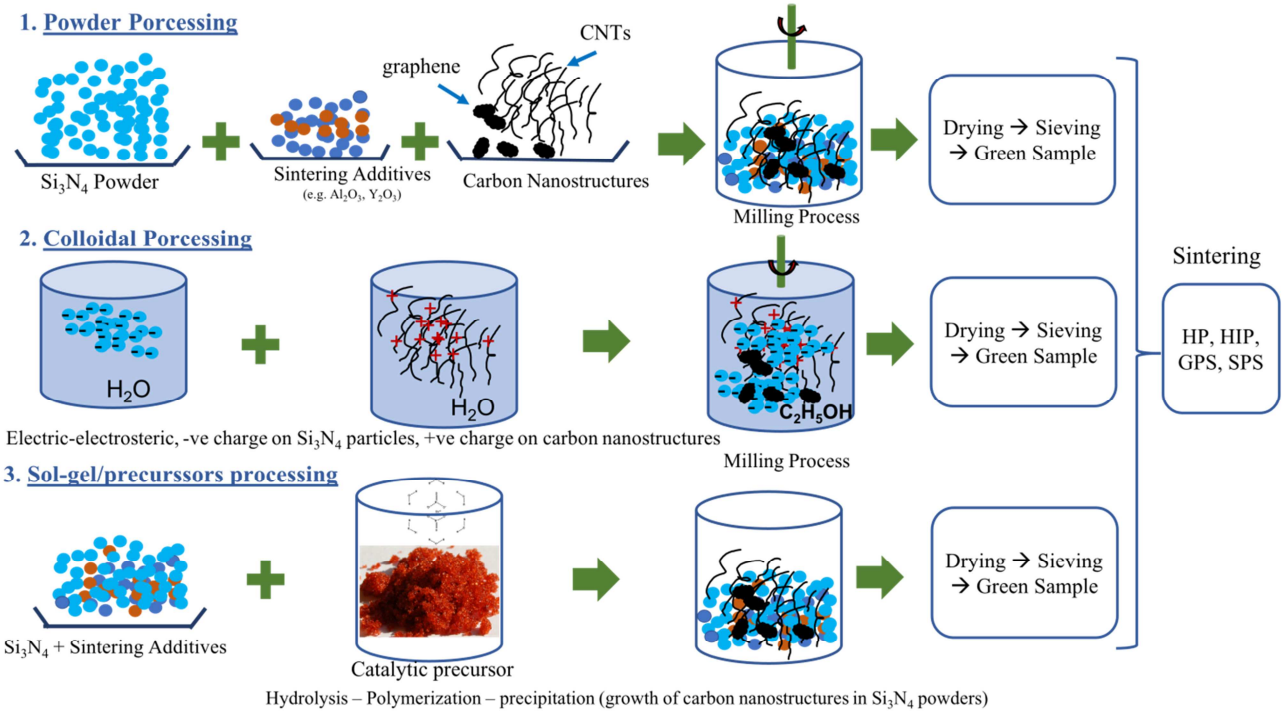

Figure 2.7 - Illustration of the main processing routes used for the processing of carbon reinforced Si_3N_4 composites. Author's work

2.4.1. Sintering aids

Due to covalent bonding and low diffusivity between the Si-N, Si_3N_4 cannot be fully densified by solid-state sintering without any additives. The addition of sintering additives introduces a so-called liquid-phase sintering process, which results in higher densification [2]. In the case of carbon nanostructures-reinforced silicon nitride composites, a wide range of sintering additives of metal oxides or non-oxides were used. So far in the literature, these additives (TiO_2, Y_2O_3, Al_2O_3, MgO, SiO_2, AlN, HfO_2, and ZrO_2) were reported as sintering additives for the fabrication of CNT-reinforced silicon nitride composites [77][78][46][79][80][81]. Recently, Matsuoka et al. [77] added HfO_2 to Y_2O_3-Al_2O_3-AlN additives to prevent the CNTs from reacting and disappearing from the composite. They reported that the addition of HfO_2 resulted in higher electrical conductivity (~102 S/m) and higher bending strength (~1086 MPa).

2.4.2. Milling Process

The degree of dispersion of carbon nanostructures in the silicon nitride matrix significantly affects the composite's final properties. To achieve excellent properties of carbon nanostructures-reinforced silicon nitride composites, fully densified composites with uniformly dispersed, undamaged, and un-agglomerated incorporation of nanostructures are inevitable. One of the major issues during the integration of nanostructures in the silicon nitride matrix is the difficulty in obtaining the nano-fillers' uniform dispersion due to their tendency of agglomeration due to van der Waals forces. Agglomerates occur due to high surface area and high aspect ratio of reinforcement, which critically affects composites' mechanical properties.

Several researchers emphasized improving the milling process and sonication before the sintering process, which enhances the uniform dispersion of CNTs/graphene in the matrix. Eventually, uniform dispersal improves the density of the sintered composites [82], [83]. Ball milling can break the interlayer van der Waals forces between graphene sheets, which results in higher chances of uniform dispersion [84]. Exfoliation of graphite is also possible by ball milling, which breaks the van der Waals forces and separates the sheets.

2.4.3. Sintering Routes

Several researchers have used several sintering techniques for the densification of CNT-reinforced silicon nitride composites over the last decade. Hot pressing (HP), hot isostatic pressing (HIP), gas pressure sintering (GPS), and spark plasma sintering, or the combination of GPS and HIP have been used so far to produce Si_3N_4 + CNT composites [45–60]. Here, extensively used techniques will be discussed.

Hot Pressing (HP): In hot-pressing (HP) technique, mechanical pressure is applied along with high temperature (1500–1800 °C) to densify the powders, and the mechanical pressure acts as a driving force to accelerate the rearrangement and sintering of particles. A schematic diagram of the hot-pressing technique is given in Figure 2.8. This process can achieve highly dense silicon nitride composites, and it is effective in improving the mechanical properties than pressure-less sintering. Based on heating sources, it can be divided into three types: a) inductive hot pressing, b) indirect resistance hot pressing, and c) field-assisted sintering technique (FAST). In inductive hot pressing, the high-frequency electromagnetic field is

applied by an induction coil. In case of indirect resistance hot pressing, the electric current is used to heat the chamber, and the convection process heats the mold. The third way of heating the sample is by applying an applied electric field, and this process was the base of a novel technique called spark plasma sintering (SPS). This process shortened the sintering time, lowered the grain growth, and saved energy.

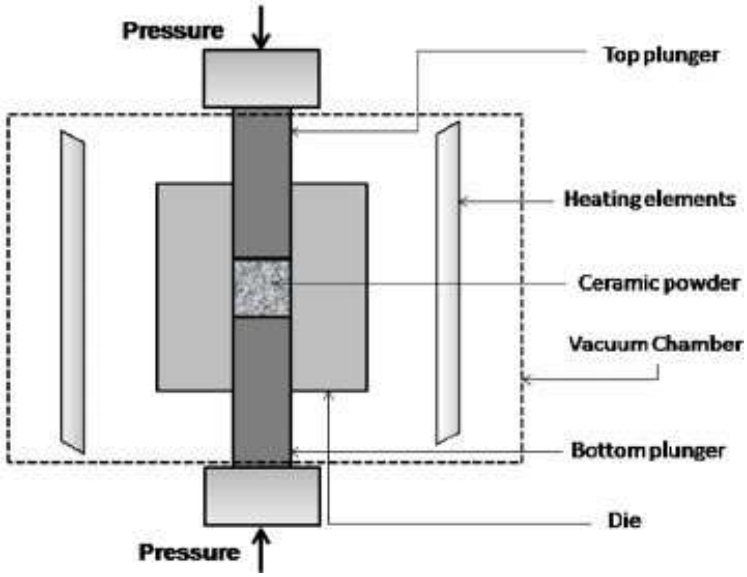

Figure 2.8 - Schematic diagram of hot-pressing technique to densify the ceramic powders [85].

Pasupuleti et al. [44] produced the monolithic and 1 wt% CNT-reinforced silicon nitride composite by hot pressing at 1750 °C under 30 MPa pressure for 1 h holding time. They achieved above 99% density of a monolithic silicon nitride, which results in high hardness (HV = 15.7 GPa) and flexural strength (1046 MPa). In the case of 1 wt% CNT-reinforced silicon nitride composite, they achieved >98.7% density with hardness (HV = 15.0 GPa) and flexural strength (996 MPa).

*Hot isostatic pressing (HIP)**:*** The hot isostatic pressing (HIP) technique has been used widely in densifying the powders, including ceramic and metallic powders. High hydrostatic pressure and high temperature are applied to compress and densify powder particles into coherent parts [86]. Hydrostatic pressure is important to mention while describing the hot isostatic pressing technique; otherwise, it will be considered hot-pressing. If only hydrostatic pressure is applied without heating, then the process will be called cold isostatic pressing (CIP). In 1976, Howmet Corporation company introduced a hot isostatic pressing technique for the first time for the application to the aerospace industry [86]. The schematic diagram of the hot isostatic pressing technique is shown in Figure 2.9. Usually, the HIP pressure is about several

hundreds of MPa, and the optimum temperature range is 1600–1700 °C to achieve the highly-dense material.

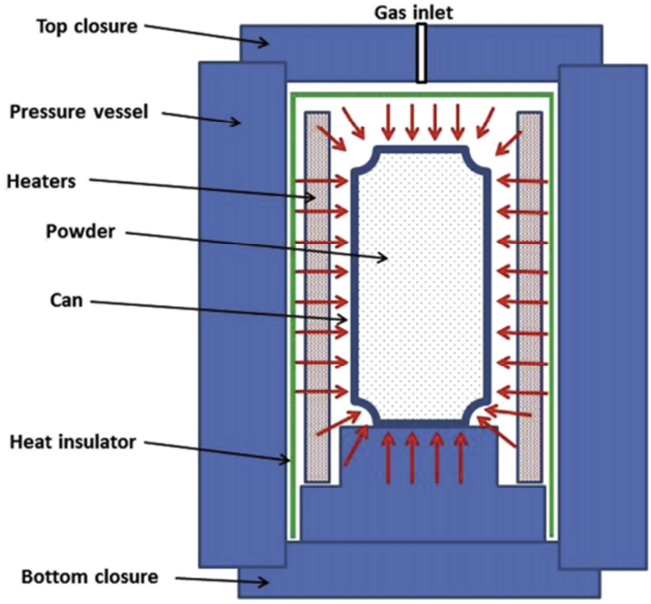

Figure 2.9 - Schematic diagram of hot isostatic pressing technique to densify the powders [87].

HIP's fundamental procedure is to place powder mixtures into a steel container, and the container is subjected to a high temperature in a vacuum environment to eliminate air and moisture from the powder mixture. The container is sealed and subjected to a hot isostatic process under inert gas pressure and high temperature, which promotes necking the powder particles, eliminate voids (porosity) and establish strong bonds between particles and results in a highly dense composite at the end of the process. Balázsi et al. [15] and Kovalcikova et al. [48] prepared a CNT-reinforced silicon nitride composite by hot isostatic pressing and achieved high density with better results in mechanical properties.

Both HIP and GPS are useful processes for densifying powders into complex shapes. However, each process has pros and cons associated with the technique. From the perspective of materials properties – high strength and reliability – the hot isostatic pressing (HIP) process is the preferred technique for densification. It has ability to produce material with uniform microstructures and compositional stability. But at the same time, high equipment and processing costs needed for HIP are concerns.

Gas pressure sintering (GPS) can produce tailored microstructures with low costs but there are some problems such as loss of volatile components (because no cladding during sintering process, the volatile compounds can escape), reaction with the gas environment and low efficiency to close surface pores. Low efficiency of closing pores might be unwanted for the

densification of some specific ceramic components, such as bearings, where high surface or near net-shape is required. Generally, GPS requires higher temperature than for HIP, hence coarser microstructure is produced by GPS. However, overall processing cost are lower for the GPS. The HIP has many advantages over other sintering techniques such as industrial, economical, multiple samples can be densified in one-time, clean process and produce the structure with uniform microstructure, highly dense, and good bonding.

*Spark plasma sintering (SPS)**:*** Spark plasma sintering is considered a hot-pressing successor because an electrical current is used to activate the sintering process. The name SPS has been widely used in literature, even considering that pulse electric current sintering (PECS) is more appropriate for such a sintering process [87]. Because plasma is not produced during this process, and the name "plasma" for such a process does not make sense. In this novel technique, the pulses of direct current (DC) and uniaxial pressure are applied to the sample within a conductive die. The main difference between SPS and hot-pressing (HP) is the application of current as many pulses for a very short interval of time, but, in the case of hot pressing, one pulse of current is applied for a long time period [87]. During SPS, a shorter sintering time is applied, restricting the grain growth and producing composites with a higher density than other sintering techniques. The general principle is illustrated in Figure 2.10. The device consists of a graphite die connected with graphite punches and a direct current (DC) source. The graphite punches exert pressure up to 100 MPa, and the pulse of DC (10 V, 10kA) passes through punches, die, and powder particles [88]. The current pulses activate the sintering between powder particles.

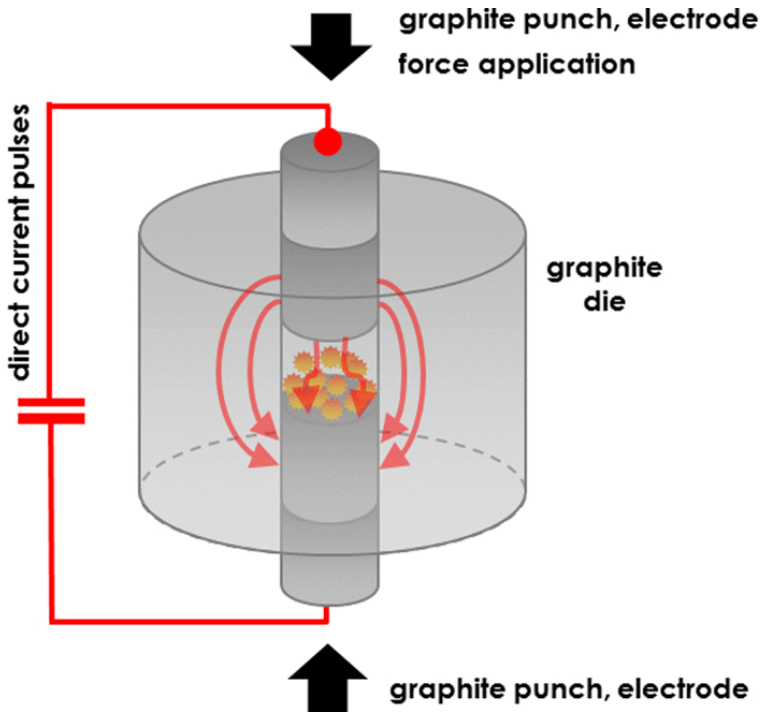

Figure 2.10 - General principle of spark plasma sintering (SPS) [88].

SPS has been applied widely in producing the Si_3N_4 + CNT composites [14,49–52,55]. An optimum time range of 3–5 min has been reported to fabricate the silicon nitride-based composites in the literature. The type of sintering technique has a significant role in achieving a highly dense composite with mechanical improvement. It is always difficult to compare the results produced by different conditions in different laboratories.

2.4.4. Role of porosity

The amount of porosity plays a detrimental role in many mechanical properties, and CNTs are susceptible to inducing porosity in the composite during sintering. Balázsi et al. found that CNTs (0 to 5 wt%) induced porosity, which caused the lowering of the elastic modulus from approximately 260 to 70 GPa [18].

2.4.5. Interfacial reaction between Si_3N_4 and reinforcement

During the sintering process at a high temperature and under high pressure for a long holding time, an interfacial reaction may occur between Si_3N_4 and carbon nanostructures. Mechanical properties depend upon the interaction between matrix and reinforcement. If the interfacial bonding is strong enough, the crack deflects along with the interface; the reinforcement remains intact, which enhances the composites' toughening effect. If interfacial bonding is

weak enough, then the crack propagates easily through the intergranular path. If the interfacial bond is too strong, the composite remains brittle, and transgranular fracture happens.

The layer of SiO_2 on Si_3N_4 particle may react with CNTs and graphene, which results in the formation of CO/CO_2 gases. The surface reaction between SiO_2 and graphene produces the interfacial pores, which induce porosity and inhibit the bonding between graphene and silicon nitride grains. If there are too many pores between graphene and silicon nitride grains, it will have a negative impact on the strength. If there are a few micropores and some areas of graphene in good contact with the silicon nitride grains, it positively impacts fracture toughness. If graphene content is dispersed evenly and has a large area in contact with the silicon nitride grains, the composites' external load may be transferred to graphene. If there are a few intergranular nanopores, they lead to Si_3N_4 and graphene sliding along with each other. The graphene can be pulled-out upon loading, and it enhances the energy dissipation capacity of the composite. It has a positive and negative impact on the strength of the composite. Bodis et al. [63] studied the effect of graphene incorporation on the toughening of Si_3N_4 containing 1, 3, and 5 wt% multi-layer graphene, with special attention to the interface phenomena between the matrix and the graphene reinforcement. They found that nanopore developed at the Si_3N_4-multilayer graphene interface due to the reaction between carbon and oxygen (i.e., SiO_2) available on the topmost layer of the silicon nitride particles. Other researchers also reported intergranular porosity formation in graphene-based ceramic composites [89][84].

Ge et al. reported [61] the formation of SiC due to the reaction between CNTs and Si_3N_4 during the sintering. The equilibrium reaction between carbon and Si_3N_4 is given below (Equation 2.1) [62,63]:

$$Si_3N_4 + 3C \xleftrightarrow{1510-1550\,℃} 3SiC + 2N_2 \text{ ---------- Equation 2.1}$$

Si_3N_4 powder particles possess the surface oxygen in the form of the SiO_2 nanolayer. This oxygen-containing phase may react with the carbon phase (CNTs/graphene) at higher temperatures and produce the CO and CO_2 gases (Equation 2.2). The diameter of CNTs might be reduced due to the loss of carbon due to a surface reaction between C and SiO_2. Carbon may cause a mass loss in the sintered samples during sintering because of the reduction of SiO_2.

$$3SiO_2\,(l) + 6C\,(s) + 2N_2\,(g) \xleftrightarrow{1547\,°C} Si_3N_4 + 6CO \text{ ---------- Equation 2.2} \quad (2)$$

During sintering, it is more likely that the SiO_2 is completely consumed in the partial oxidation of carbon nanostructures (CNTs, graphene), and CO is no longer formed due to the limited reactant oxygen.

2.5. Testing methods for mechanical and tribological properties

It is essential to know the mechanical properties, structural integrity, and tribological properties of a material in order to apply these materials in a specific environment where they can sustain. For measuring these properties, there are testing methods that give us the characteristics of a material. Due to the existence of many testing methods, comparing the properties of materials was difficult because the materials preparation methods were different by researchers. It was necessary to develop standard testing methods that are universally acceptable and apply to all the materials prepared by various methods. Many testing methods have been standardized and accepted by the international community. However, there are still few testing methods are not considered very accurate to measure the specific property of a material. Here, I will discuss the testing methods used to measure this work's properties and give an insight into the testing methods.

2.5.1. Hardness

In general, hardness is a measure of resistance to localized plastic deformation caused by indentation or abrasion, or scratch. There are different hardness testing forms, such as indentation hardness, scratch hardness, electromagnetic hardness, and rebound hardness. Indentation hardness testing is widely used to measure the hardness of a material, including ceramics. Because indentation hardness testing is simple, more reliable, commonly practiced, and the values can be compared easily with other researchers' results. The indentation hardness is measured by applying a load (indenter) on a polished surface of a ceramic for a specific period of time. The indenter leaves its impression (penetration) on the body and then the depth of penetration is measured.

Indentation hardness measurements have several testing methods or scales, such as:

- Berkovich indenter method,
- Brinell hardness method,
- Vickers microhardness method (square-based diamond pyramid),
- Knoop method (rhombohedral-diamond pyramid),
- Rockwell method (diamond cone).

2.5.1.1. *Vickers microhardness method*

The basic principle of Vickers hardness is to measure the ability of a material to resist plastic deformation. The method was developed by Robert L. Smith and George E. Sandland in 1921 at a British company Vickers Limited [90]. They presented an indentation hardness method as an alternative to the Brinell hardness method. A fundamental principle of the Vickers hardness method and equipment are illustrated in Figure 2.11. The Vickers hardness testing for ceramic materials is governed by this standard BS EN 843-4:2005 [91].

The Vickers hardness value is calculated according to the following formula (Equation 2.3):

$$H_v = 0.189 \frac{F}{d^2} \text{ ---------- Equation 2.3}$$

Where, F is the applied load in N unit, d is a mean value of diagonals length in mm unit.

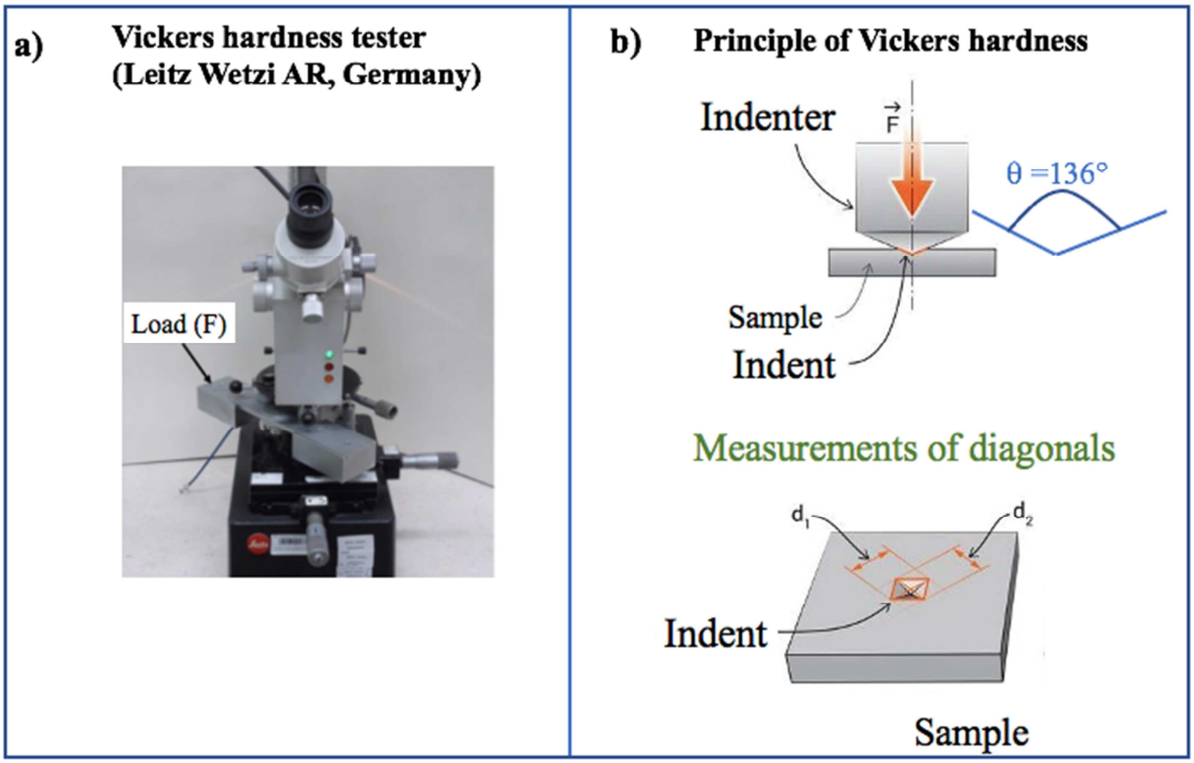

Figure 2.11 Vickers hardness test equipment was used for the current research work and b) principle of Vickers hardness method. Author's work

2.5.2. Fracture toughness

Fracture toughness is an essential property of a material that defines a material's ability to resist the fracture. Fracture toughness of carbon nanostructures reinforced silicon nitride

composites mainly depends on the content of β-Si_3N_4, uniform distribution of nanophase, and toughening mechanism (crack bridging, pulling-out, crack deflection) in the composite. There are several methods to measure fracture toughness, such as single-edged pre-cracked beam (SEPB), chevron notched beam (CNB), the surface crack in flexure method (SCF), and single-edged V-notched beam (SEVNB). However, in the literature, the fracture toughness of Si_3N_4 composites was measured by the Vickers indentation fracture (IF) method. Vickers indentation fracture method is a nonconventional and controversial method for measuring fracture toughness, but it is widely used for research purposes. However, the Vickers indentation fracture method (IF) has been criticized by the traditional fracture mechanics' community due to unreliability, inaccuracy, and imprecision of this method [92], [93]. The American Society Testing and Materials (ASTM) and European Committee for Standards (CEN) have not recognized this technique as a standard testing method to measure fracture toughness. But this method is widely used to report the data as a fracture toughness (K_{IC}) of ceramics. The traditional fracture mechanics community suggests that it would be best to report the data as "indentation fracture resistance $K_{IIFR,}$" which may or may not approximate the fracture toughness K_{IC}. The K_{IIFR} measures the resistance to crack extension from a particular type (Vickers) of indentation [94].

Why is the Vickers indentation method being used to measure fracture toughness? Sample preparation is difficult for the traditional testing method because ceramics are brittle and susceptible to fracture. Vickers indentation method has become well-known to measure fracture toughness because (i) a small sample is needed, (ii) test piece preparation is simple, (iii) the crack length is measured optically, and (iv) this method is quick and cheaper [93]. Based on the suggestion from the fracture mechanics community, the term "indentation fracture resistance (K_{IIFR})" will be used instead of "fracture toughness (K_{IC})" in the thesis.

The principle of the test is that the Vickers indenter creates cracks along the edges of the pyramid impression on the sample's polished surface. These crack lengths are measured, and indentation fracture resistance is calculated based on crack lengths, load, hardness, elastic modulus, and indentation diagonal size by using a different formula. Two kinds of cracks occur most of the time: Palmquist cracks and semi-circular (half-penny) cracks. The schematic illustration of cracks created by the indenter is shown in Figure 2.12.

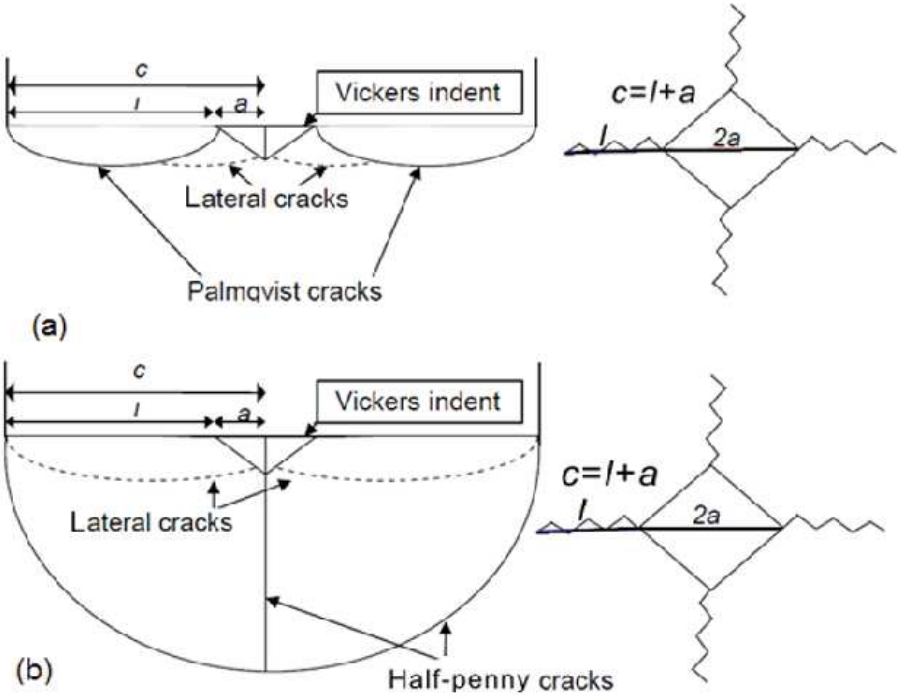

Figure 2.12 – The schematic illustration of cracks created by indenter [95].

In case of indentation cracks of the semi-circular (half-penny) shape, the indentation fracture resistance is calculated by the Anstis Equation 2.4 [96]:

$$K_{IC} = 0.016 \left(\frac{E}{H}\right)^{1/2} \left(\frac{P}{c^{3/2}}\right)$$ ---------- Equation 2.4

Where E is Young's modulus, H is hardness, P is the applied load, c is the length of the crack.

In case of indentation cracks of the Palmquist shape, the indentation fracture resistance is calculated by the Shetty equation [97]:

$$K_{IC} = 0.0889 \left(\frac{H_V \cdot P}{4\ell}\right)^{1/2}$$ ---------- Equation 2.5

Where, H_V is the hardness, P is the applied load, ℓ is the difference of the crack length from the center of the indenter and the half-size of the diagonal ($\ell = c - a$).

2.5.3. Flexural strength

Flexural strength is a material's ability to sustain the maximum stress before it yields or fracture [98]. Flexural strength is measured by bending either 3 – point or 4 – point bending test. Due to ceramics' brittleness, tensile testing is impossible because the preparation of the specimen is difficult. So, the bending test is an alternative to measure the strength and stress-strain curve, and the preparation of specimens is easier. Bar or rod-like specimen is used to subject under the bending test. The bending test has two types: 3 – point and 4 – point bending test.

In a 3 – point bending test, the bar/rod is placed in tension, and the outer fibers are subjected to maximum stress and strain (Figure 2.13 – a). Failure will occur when the strain or elongation exceeds the material's limits.

In the 4 – point bending strength, the stress is on four points in the specimen. The schematic illustration of the bending test is given in Figure 2.13 – b.

A bending test can be also used to measure fracture toughness and fatigue properties. To measure fracture toughness, a notch is created in the specimen and then subject it to a bending test, and the procedure of this test is given in the standard ASTM E-1290. For fatigue properties, the procedure is presented in this standard ASTM D7774.

In the case of 3 – point bending test (Figure 2.13 – a), the flexural strength (σ_{3P}) is measured by the following formula Equation 2.6.

$$\sigma_{3P} = \frac{3FL}{2bd^2} \text{ ---------- Equation 2.6}$$

Where, σ_{3P} is flexural stress, F is the load (force) at the fracture point (N), L is length of the support span, b is width, and d is thickness.

Measuring of flexural strength in case the of 4 – point bending test on rectangular specimen if the loading span is 1/2 of the support span (Figure 2.13 – b) by Equation 2.7.

$$\sigma_{4P} = \frac{3FL}{4bd^2} \text{ ---------- Equation 2.7}$$

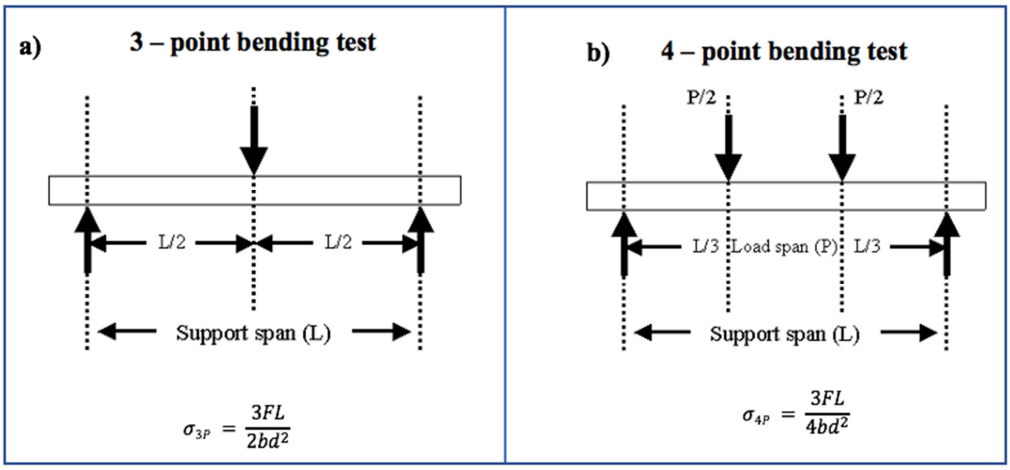

Figure 2.13 – Illustration of bending test: a) 3 – point bending test and its formula to calculate the flexural strength; b) 4 – point bending strength and its formula to calculate the flexural strength. Author's work.

2.5.4. Tribological properties

Tribology is the study of interacting surfaces of two bodies [99]. Friction and wear happen as the result of mechanically contacting and sliding two surfaces. The tribological study deals with adhesion, friction, wear, and lubrication in all contacting areas. The factual knowledge of tribology improves the service life, safety, and reliability of interacting machine components and yields substantial economic benefits. There are two aspects of tribology: the first is science, which deals with the primary mechanism, and the second is technology, which deals with design, manufacture, and maintenance.

The standard test geometries used to study wear are pin-on-flat, four-ball, ring-on-flat, pin and V-block, and rolling/sliding disk contact [100]. The importance of tribology can be realized with an impact on the global economy. According to the calculation, 23% of the world's energy consumption is due to tribological issues. 20% of that is consumed to overcome the friction, and 3% is used to reprocessing the worn parts [101].

Wear test is performed to predict the wear performance and wear mechanism of a material used in tribo-system. Friction and wear are two primary components of the tribo-system. The coefficient of friction (COF) (μ) is a dimensionless quantity and defined as the ratio between frictional force (F_S) and normal force (F_N) (Equation 2.8) [102].

$$\mu = \frac{F_S}{F_N} \text{ ---------- Equation 2.8}$$

Wear is removal material as a result of interacting with surfaces of two bodies. The worn material is quantified as weight loss or volume loss. Measurement of wear is done by different techniques such as precision balance to measure the weight (mass) loss, profiling surfaces, or using a microscope to measure the wear depth or cross-sectional area of a wear track.

The wear rate (*W*) is volume loss (V) per total sliding distance (L) and applied load (F), and its unit is (mm^3/Nm) (Equation 2.9).

$$W = \frac{V}{L \bullet F} \left[\frac{mm^3}{m \bullet N}\right] \text{---------- Equation 2.9}$$

Where, *W* is wear-rate, *V* is volume loss in mm^3, *L* is the length of sliding distance in m, and *F* is load in N.

The different types of wear which are given below:

- Adhesive wear,
- Abrasive wear,
- Fatigue wear,
- Chemical wear,
- Erosional wear,
- Vibrational wear,
- Cavitation wear.

Tribological tests configurations

There are several types of configurations for tribological tests (Figure 2.14):

- Point contact configuration (Ball-on-plate, Ball-on-disc),
- Linear contact (Block-on-ring, Pair V block-on-pin),
- Plane contact (Block-on-plate, Pin-on-disc).

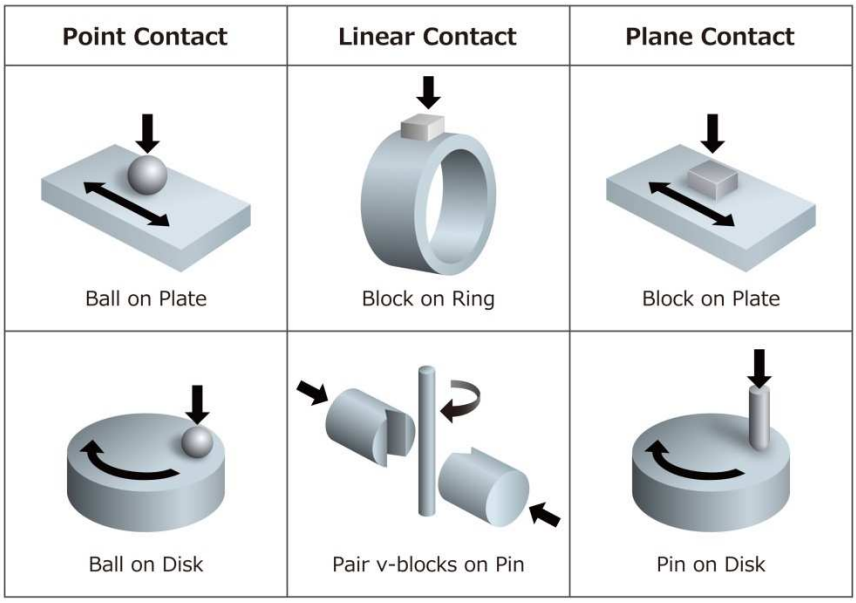

Figure 2.14 – Several types of test configurations to measure the tribological properties of a material [103].

2.5.5. Wear Mechanism

Wear occurs due to the mechanical failure of the local surface and categorizes different types of mechanisms. The deterioration of the surface happened due to a single or combination of multiple wear mechanisms. Friction and wear are not mechanical properties, but they are closely related to materials' mechanical properties. In some instances, silicon nitride's hardness and fracture toughness are considered the most essential properties in meeting wear requirement [104].

The wear rate depends on the degree of abrasive penetration into the surface of the material under abrasion. Particles that cause wear usually have sharp edges to cut or shear the solid under the wear [105]. Several wear mechanisms, such as abrasion, adhesion, micro-fracture, and delamination, separate or combined, contribute to the wear damage in ceramic-ceramic sliding and rolling contacts [106]. Figure 2.15 illustrates a typical wear mechanism in ceramics [106].

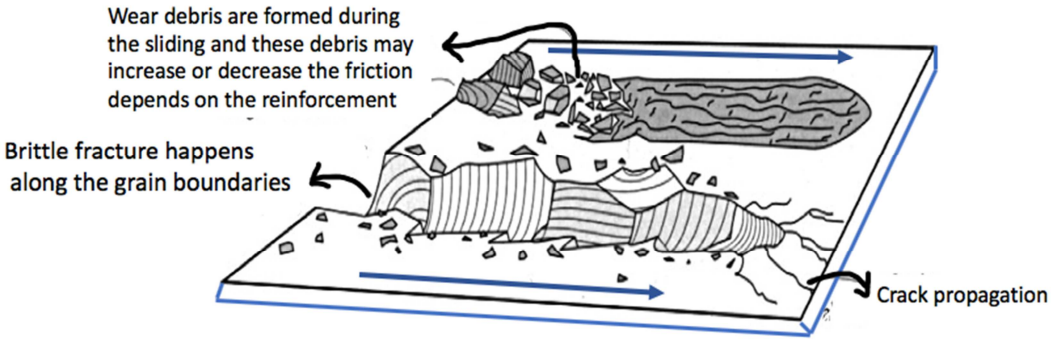

Figure 2.15 – Typical wear mechanism in ceramic materials [106].

The purpose of carbon nanofillers in the silicon nitride matrix is to reduce the friction and wear rate during the sliding of two surfaces. The carbon nanofillers should be enabled to act as lubrication. Lubrication has three main regimes, e.g., fluid film lubrication, boundary lubrication, and mixed lubrication. The graphene and CNTs may protect the surface from mechanical and chemical wear and promotes local hydrodynamic lift. This enables a gradual transition from mixed lubrication conditions to hydrodynamic lubrication in the tribological system.

A general wear mechanism in silicon nitride ceramics, the grains are detached from the surface during the sliding. These grains cause the abrasion and pronounce the effect of wearing. In general, worn debris were formed by the action of the micro-abrasion mechanism, being compacted during the motion of the sliding pairs. If CNTs and graphene are present in the worn debris, then the worn debris serves as lubrication and overcomes friction. Gonzalez-Julian et al. [76] observed one of the examples in in-situ CNTs/Si_3N_4 composites; the debris were well adhered to the surface, which protected it against wear.

In summary, four factors are important in enhancing the tribological properties of carbon nanostructures reinforced silicon nitride composites:

1) uniform distribution of carbon nanostructures in the matrix,
2) load transfer efficiency of carbon nanostructures,
3) structure stability of reinforced nanostructures during processing in the matrix,
4) interfacial bonding between reinforcement and matrix.

3. Experimental Part

3.1. Experimental program

The experimental works were carried out at the Institute of Technical Physics and Materials Science – Hungarian Academy of Sciences (MFA-MTA-EK), Budapest, Hungary and Institute of Materials Research – Slovak Academy of Sciences (Division of Ceramic and Non-Metallic Systems), Košice, Slovakia. The experimental scheme is given in the diagram (Figure 3.1). According to the diagram, three different silicon nitride systems were prepared by hot isostatic pressing (HIP) or gas pressure sintering (GPS), these sintered systems were characterized by different techniques (SEM, TEM, HRTEM, EDX, and XRD) and followed by testing of their mechanical and tribological properties. Each system will be discussed in the following chapters separately and followed by a conclusion with future work.

No.	Systems	Starting powders	Oxidation time (h)	Sintering method	Sintering Temperature	Detailed Study in
1	Monolithic Si_3N_4 systems	$\alpha - Si_3N_4$	0 10 20	HIP	1500 & 1700 °C	Chapter 4
2	Si_3N_4 + 3 wt% MWCNTs	$\alpha - Si_3N_4$	0 10 20	HIP	1700 °C	Chapter 5
3	Si_3N_4 + 1 wt% graphene	$\alpha - Si_3N_4$	0	HIP GPS	1700 °C	Chapter 6

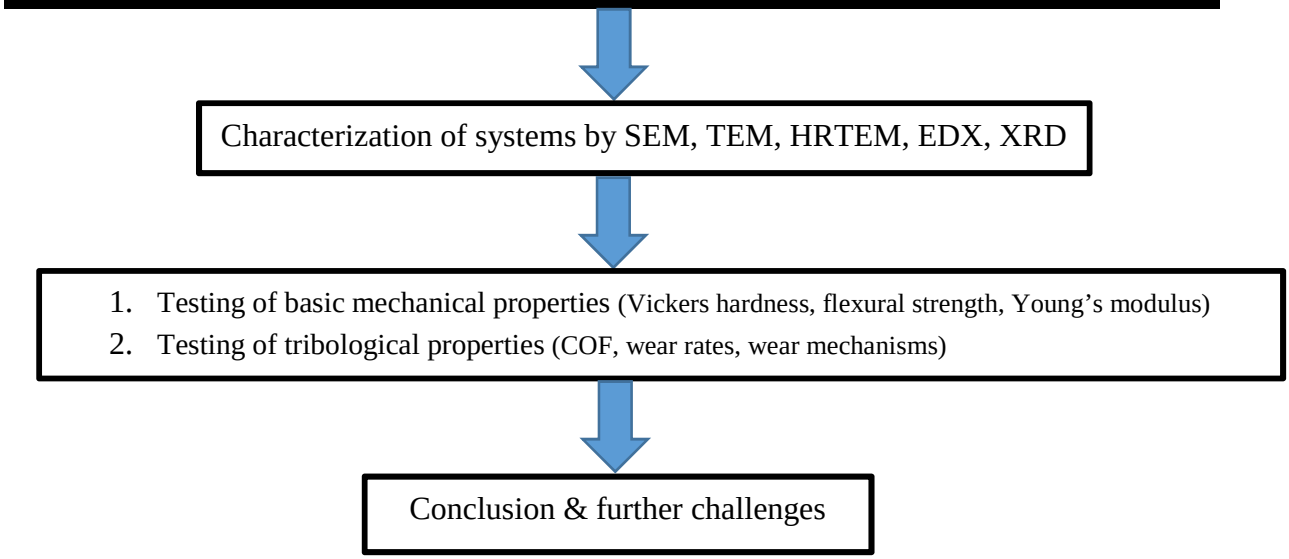

Figure 3.1 – experimental program

3.2. Characterization techniques and methods used for the current work

After a brief discussion about the mechanical and tribological testing methods, the characterization methods and techniques are described, which were used to investigate current work.

3.2.1. Ceramographic preparation of samples

Grinding and polishing

After hot isostatic pressing, the sintered samples were cut into rectangular shape. The sintered samples were subjected to a grinding process to prepare the smooth surface with a precise dimension of 3.5 × 5 × 50 mm. After griding, the samples were polished with polishing papers with a decreasing order of abrasive particles.

3.2.2. Density

The apparent densities of the sintered samples were measured by a standard Archimedes method using distilled water as an immersion medium at room temperature, according to Equation 3.2.

$$\rho_s / \rho_w = m_s / (m_s - m_w) \quad \text{---------- Equation 3.1}$$

$$\rho_s = m_s \cdot \rho_w / (m_s - m_w) \quad \text{---------- Equation 3.2}$$

Where, ρ_s is the density of sintered sample (g/cm^3), ρ_w is the density of water at room temperature (≈ 1 g/cm^3), m_s is the mass of sintered sample in the air (g), and m_w is the mass of the sintered sample in the water (g).

3.2.3. Transmission electron microscopy (TEM)

TEM was carried out only for the base powders of α - Si_3N_4 before and after oxidation. Transmission electron microscopy (TEM, Philips CM-20) with an accelerating 200 kV voltage was used for the microstructural characterization of the oxidized and un-oxidized powders.

3.2.4. Energy dispersive X-ray spectroscopy (EDX)

EDX was carried out only for the base powders of α - Si_3N_4 before and after oxidation. Energy-dispersive X-ray spectroscopy (EDS) was used for the qualitative analysis of the base powders (un-oxidized and oxidized Si_3N_4 powders) to quantify elemental compositions. EDX was used to quantify the atomic oxygen percent in the powder before and after oxidation.

3.2.5. High resolution transmission electron microscopy (HRTEM)

High-resolution transmission electron microscopy (HRTEM, JEOL3010) with an accelerating voltage of 300 kV was used for the nano structural analysis of the oxidized powders and sintered samples. HRTEM helped to figure out the nano-layer of SiO_2 film on the α - Si_3N_4 powder particles after the oxidation.

3.2.6. Scanning electron microscopy (SEM)

The microstructures, fractured surfaces, and wear mechanisms of the tested materials were examined by scanning electron microscopy (SEM, LEO 1540 XB).

3.2.7. X-ray diffraction spectroscopy (XRD)

XRD is a rapid analytical technique primarily used to identify phases of a crystalline material and provide information on unit cell dimensions. The phase composition of starting powders

and sintered samples were analyzed using an X-ray diffractometer (Bruker AXS D8) with Cu Kα radiation.

3.3. Mechanical and tribological testing used for the current work

The following techniques were used to measure the mechanical and tribological properties of sintered samples.

3.3.1. Vickers hardness

Vickers hardness tester (Leitz Wetzi AR, Germany) was used to indent the polished surface of all investigated systems by an indenter of a squared diamond pyramid with a top angle of 136° into a material by an applied load F (10 N), for 10 seconds. 10 Vickers indentation per sample were introduced after the polishing to a 0.1 µm surface roughness. The Vickers hardness (H_v) was calculated through the formula (Equation 2.3). The Vickers hardness testing standard (BS EN 843-4:2005) for ceramic materials was followed to measure samples' hardness.

3.3.2. Indentation fracture resistance (K_{IIFR})

To determine the fracture indentation resistance of investigated systems, the Vickers indentation method was used. At least 10 Vickers imprints per samples were introduced with a load of 10 N. Optical microscopy with a scale was used to determine the length of propagated radial cracks, and the Shetty formula (Eq. 2.5) was used to determine the fracture indentation resistance (K_{IIFR}).

3.3.3. Elastic modulus and flexural strength

Elastic modulus and flexural strength (3 – and 4 – point bending strength) of sintered samples was measured by bending tests on a tensile/loading machine (INSTRON-1112). The flexural strength was calculated using formulae (Equations 2.6 and 2.7).

3.3.4. Tribological Properties

As there are several configurations for tribological tests, which have been described above in Figure 2.14. Here, the point contact configuration (Ball-on-plate, Ball-on-disc) was adopted to

analyze experimental materials' tribological behavior. For monolithic Si_3N_4 systems, ball-on-disc point contact configuration was used while ball-on-plate for carbon nanofillers reinforced silicon nitride composites (Si_3N_4 + 3 wt% MWCNTs and Si_3N_4 + 1 wt% Graphene).

For monolithic Si_3N_4 systems, the tribological measurements were performed using High-Temperature Tribometer THT (CSM, Switzerland) and a Si_3N_4 ball (D=5 mm) with roughness $R_a = 0.025\ \mu m$ under dry sliding conditions at room temperature with 51 ± 10% humidity. The normal applied load was 5 N, which corresponds to a Hertzian pressure of ~ 1.27 GPa, the sliding speed was 0.05 m/s with a data acquisition rate of 5.2 Hz and the sliding distance was 1000 m. Before the tribological measurements, the sample surfaces have been polished to a surface roughness below Ra = 0.05 μm.

For carbon nanofillers reinforced Si_3N_4, the tribology measurements were carried out on equipment UMT 3 (Bruker) using the reciprocating ball-on-plate technique. The wear behavior of the experimental materials was studied in dry sliding in air. The tribological partner was a highly polished (roughness Ra < 0.10 μm according to ISO 3290) Si_3N_4 ball with a 6.35 mm diameter.

For Si_3N_4 + 3 wt% MWCNTs systems, the applied load was 13.5 N with sliding speed of 10 cm/s and sliding distance of 720 m. The Hertzian contact pressure was ~ 2 GPa. The experiments were realized at room temperature at the relative humidity of 40 ± 5%.

For Si_3N_4 + 1 wt% graphene systems, the tribological tests were carried under two different loads of 13.5 N and 5 N with sliding speed of 10 cm/s and sliding distance of 720 m. The Hertzian contact pressures was 2 GPa under 13.5 N load and 0.8 ~ 0.9 GPa under 5 N load.
The experiments were realized at room temperature at the relative humidity of 40 ± 5%.

3.3.5. Coefficient of friction and wear rate

Coefficient of friction (COF) (μ) was measured by a formula (Equation 2.8). The wear rates (W) were measured based on the volume loss (V) per total sliding distance (L) and load (F) according to the Equation 2.9.

4. Monolithic Si_3N_4 systems

4.1. Starting powders

Commercial α – Si_3N_4 powders (supplied by Ube, SN-ESP) containing >95% α-phase were used as starting powders to fabricate specimens. The compositional details of the starting powder are given in Table 4.1.

Table 4.1 - Compositional details of starting powder Si_3N_4. [107]

Type	**Grade**	**Specific Surface Area (SSA) m^2/g**	**Oxygen (wt%)**	**C (wt%)**	**Cl (ppm)**	**Fe (ppm)**	**Ca (ppm)**	**Al (ppm)**	**α-phase content (wt%)**
Standard Grade (E-Series)	SN-ESP	6~8	< 2	0.1	< 100	16	1	3	>95

The starting silicon nitride powders, containing high fractions of α-phase, were subjected to the oxidation process and divided into three groups:

Batch 1: As received un-oxidized α – Si_3N_4 powder

Batch 2: α – Si_3N_4 powder was oxidized at 1000 °C for 10 hours in an ambient air environment

Batch 3: α – Si_3N_4 powder was oxidized at 1000 °C for 20 hours in an ambient air environment

4.1.1. Oxidation process of starting powders

The oxidation of the starting powder was done at a high temperature for two different time regimes to introduce oxide phases in the form of amorphous SiO_2 films on nanoparticles (approximately average size in between 100 nm ~ 600 nm) of α – Si_3N_4 powders. The oxidation process is demonstrated in Figure 4.1. The 100 grams of bulk powder was placed in a muffle furnace (type NABERTHERM L 1) in an ambient air environment. The process was carried out carefully to follow the industrial practice. Two following strategies of oxidation were adopted:

1. Oxidation of α – Si_3N_4 powder at 1000 °C for 10 hours in the ambient air environment.

2. Oxidation of α – Si_3N_4 powder at 1000 °C for 20 hours in the ambient air environment.

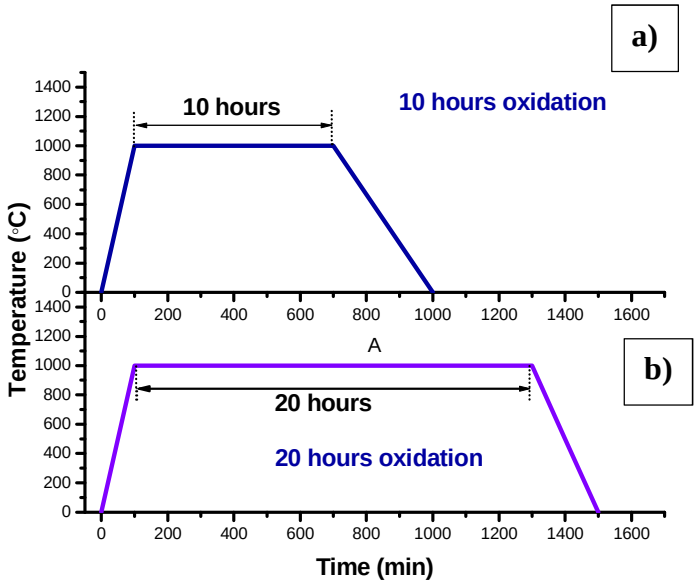

Figure 4.1 – Oxidation process of starting powders: a) Batch 2 oxidized at 1000 °C for 10 hours; b) Batch 3 oxidized at 1000 °C for 20 hours.

4.1.2. Sintering aids

Due to covalent bonding and low diffusivity, Si_3N_4 cannot be densified by dry sintering without any additives. The addition of sintering additives is needed to create a liquid-phase sintering process, which results in full densification [16]. In the present work, Al_2O_3 and Y_2O_3 were used as sintering aids. Al_2O_3 and Y_2O_3, as sintering additives, have been widely used in several works [42] [108]. Al_2O_3 (Alcoa, A16) and Y_2O_3 (H. C. Starck, grade C) were used 4 wt% and 6 wt% of the total amount of powder, respectively (Table 4.2). Before the milling process, polyethylene glycol (PEG) as a surfactant agent and ethanol were added to powder mixture. The surfactant helps neutralize electrostatic charges, lower the surface tension, and improve the solution's rheological properties.

Table 4.2 – Composition of powder mixture.

	α – Si_3N_4 (wt%)	Al_2O_3 (wt%)	Y_2O_3 (wt%)
Batch 1: Unoxidized	90	4	6
Batch 2: 10 hours oxidized	90	4	6
Batch 3: 20 hours oxidized	90	4	6

4.1.3. Milling process

Wet milling was chosen to mill the powder mixtures because it is a useful technique in achieving fine powder [109]. Ethanol (C_2H_6O) was used for wet milling. The use of ethanol is

helpful to lower the surface energies of the powder particles, less deterioration of milling media (jar, balls and agitators). These three powder mixtures were subjected to the ball milling one by one to mix and reduce the size of the powder particles. The particles' average size was in the range of 50 nm ~ 500 nm. The attritor ball mill (Union Process, type 01-HD/HDDM) is equipped with a jar, a cooling water pipe connection, a metallic shaft equipped with zirconia-agitating discs, and zirconia balls as grinding media. Zirconia (ZrO_2) balls (1 mm diameter) were used as grinding media. The combined impact and shearing actions of balls enhance the milling efficiency. The powders have milled at a speed of 4000 rpm for 4 hours. The powder was dried at 150 °C and sieved through sieving with a mesh number of 150 µm.

4.1.4. Fabrication of green samples

The powder was pressed in a metallic mold by a hydraulic pressing (H Type Frame, 4-Pillar Type) under 200 MPa pressure for 5 seconds to fabricate green samples. These prepared samples are called green samples or green bodies before a firing process to eliminate retained ethanol (C_2H_6O) and PEG from the samples. The schematic diagram explains the fabrication of green samples (dry pressing process) (Figure 4.2).

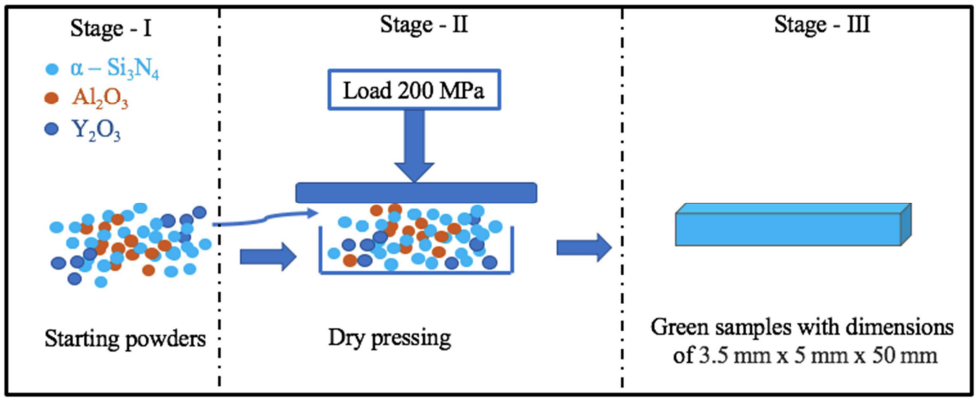

Figure 4.2 - Dry pressing process (Fabrication process of green bodies).

4.1.5. Densification of powders by hot isostatic pressing (HIP)

Hot isostatic pressing (HIP) densifies the powder in a furnace at a high temperature and pressure. The inert gas is used to act pressure uniformly in all directions to provide isotropic properties and full densification. The sintering process was carried out in the hot isostatic pressing (HIP) – ABRA SHIRP 8/16-200-2000 machine for the present work.

The green samples were densified by HIP at two different temperatures:

1. Densified at 1500 °C and 20 MPa pressure in the N_2 gas environment for 3 hours a holding time.
2. Densified at 1700 °C and 20 MPa pressure in the N_2 gas environment for 3 hours a holding time.

Two different temperatures were selected to optimize the effect of sintering temperature on the final product's structural and mechanical properties. The heating regime is given in Figure 4.3. The heating rate was 25 °C/min. The detail of sintered samples is given in Table 4.3.

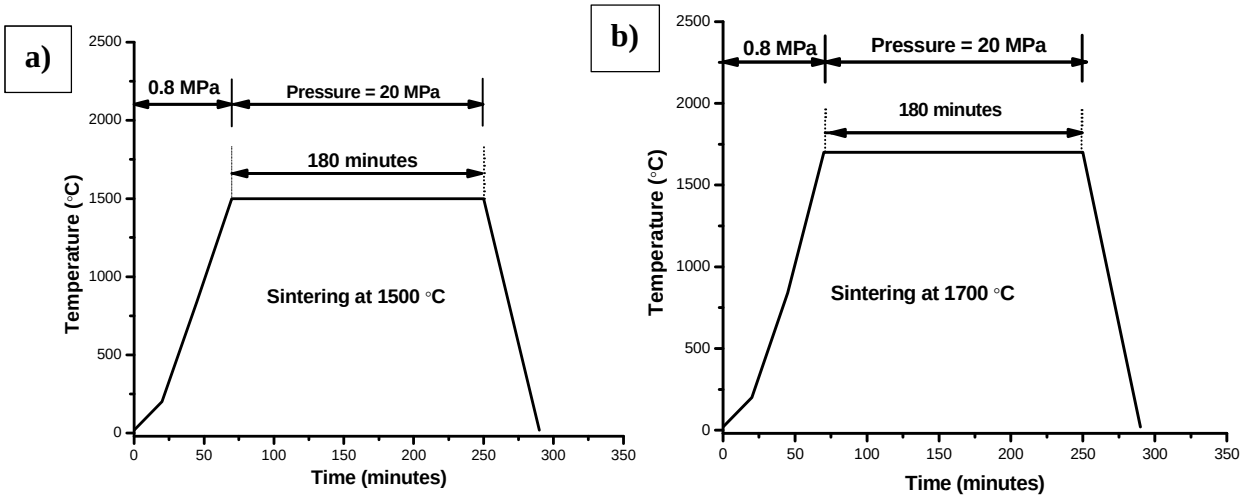

Figure 4.3 - Heating scheme during sintering process.

Table 4.3 – Detailed information of sintered samples

No.	**SN-15/0**	**SN-15/10h**	**SN-15/20h**	**SN-17/0**	**SN-17/10h**	**SN-17/20h**
Oxidation Time (hrs)	0	10	20	0	10	20
Sintering Temperature (˚C)	1500	1500	1500	1700	1700	1700
Apparent Density (g/cm^3)	3.330	3.303	3.27	3.431	3.387	3.352
$\frac{\beta - Si_3N_4}{Si_2N_2O}$	$\frac{12.8}{12.6}$, (1 : 1)	$\frac{5}{17.8}$, (0.28:1)	$\frac{10}{23}$, (0.43:1)	$\frac{78}{6.7}$, (11:1)	$\frac{60}{20.5}$, (2.9:1)	$\frac{56.4}{25.8}$, (2.2:1)

Average size of β-Si_3N_4 (nm)	39.39 ± 4.4	39.65 ± 4.5	37.14 ± 4.1	60.81± 8.4	56.75 ± 8.3	56.37 ± 8.5
Average size of Si_2N_2O (nm)	52.53 ± 4.4	55.18 ± 4.5	51.90 ± 4.1	37.72 ± 8.4	62.71 ± 8.3	64.18 8.5

4.2. Investigation of starting powders

The oxidized and un-oxidized α – Si_3N_4 powders were examined using SEM and TEM techniques. The SEM and TEM images of oxidized and un-oxidized starting powders are given in Figure 4.4.

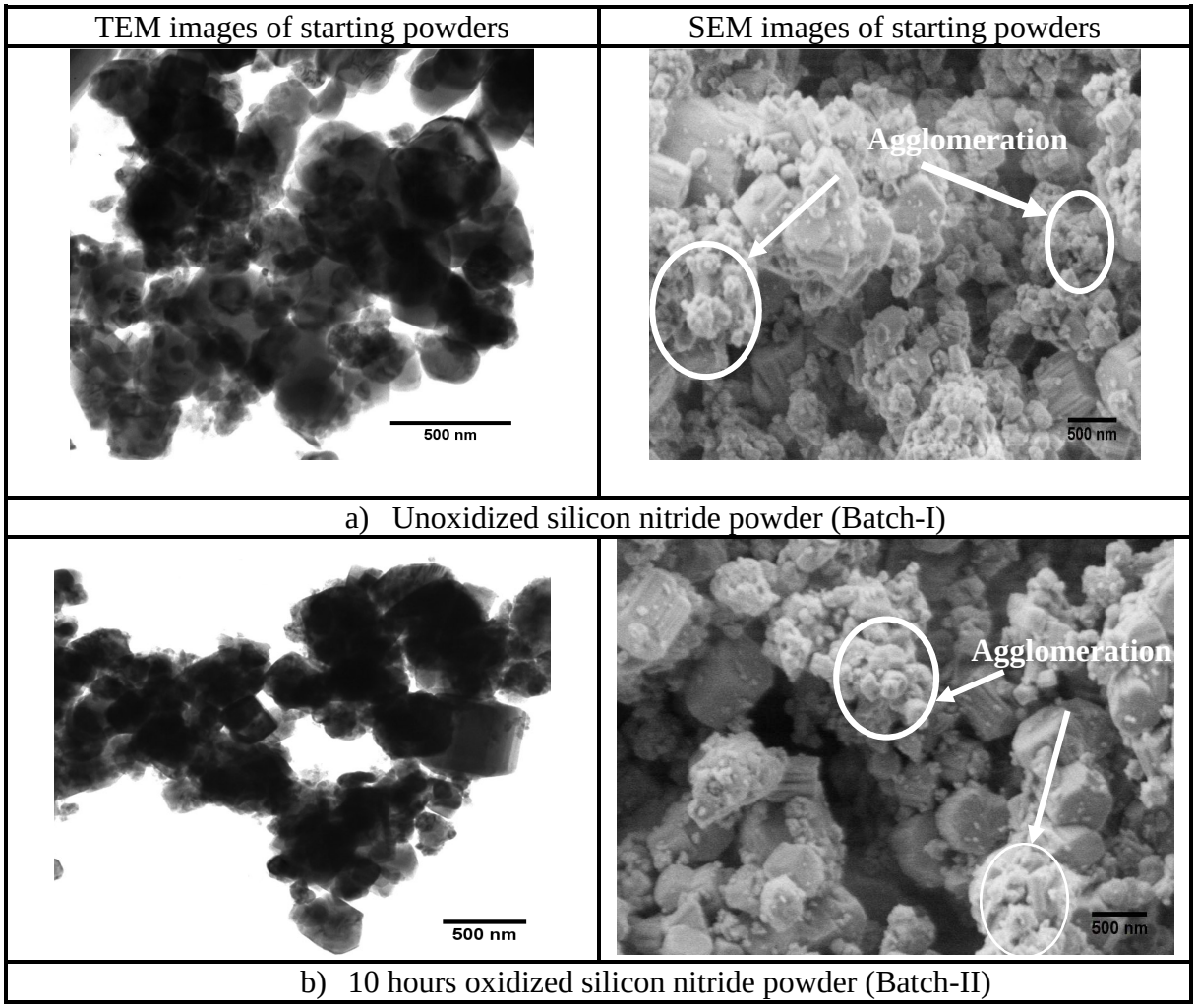

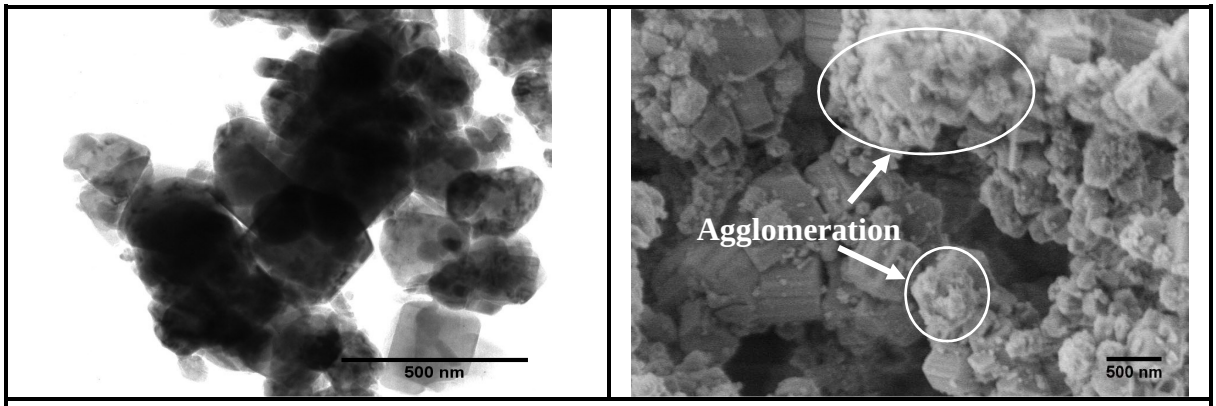

c) 20 hours oxidized silicon nitride powder (Batch-III)

Figure 4.4 - TEM and SEM images of starting powders: a) Un-oxidized silicon nitride powders (Batch-I); b) 10 hours oxidized silicon nitride powders (Batch-II) and c) 20 hours oxidized silicon nitride powders (Batch-III).

Based on SEM and TEM results, it was observed that the morphology, shape, and size of powder particles were similar before and after oxidation (Figure 4.4). Some agglomeration of smaller particles of powder was also observed in both oxidized and unoxidized powders. The particle size of starting powders was in the range of 50 ~ 500 nm range. On microscopic examination, it was challenging to observe the effect of oxidation on powders. Further investigation was needed to analyze the impact of oxidation.

To analyze the oxidation process's effectiveness, EDX was performed for quantitative analysis to confirm the presence of atomic oxygen in the powders before and after oxidation. Figures 4.5 and 4.6 present the energy dispersive spectroscopy results of starting powders with the possible present amount of atomic oxygen. According to EDX results, it was observed that the atomic percent of oxygen increased in the powders with the oxidation time. As increase of atomic oxygen in powders, it confirms that the oxidation process was successful.

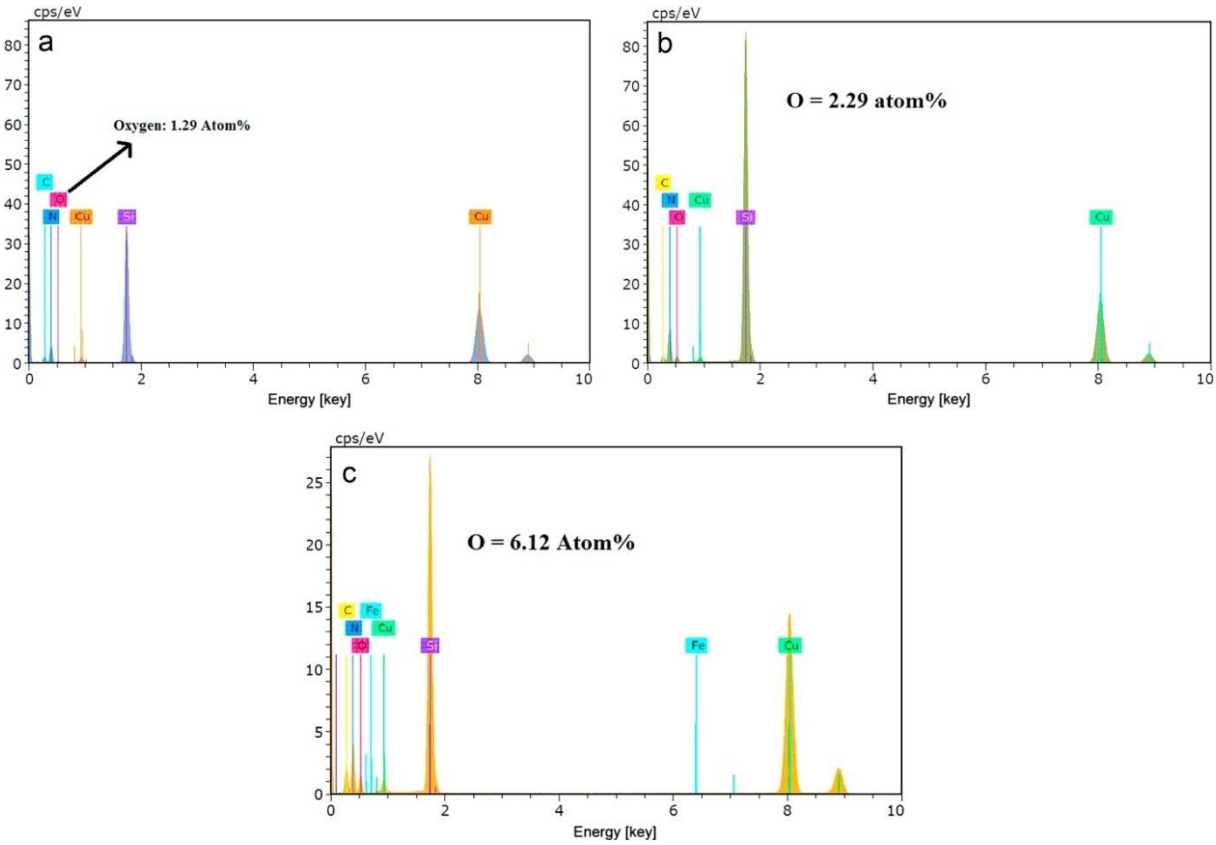

Figure 4.5 – Energy Dispersive Spectroscopy (EDS) results of starting powder silicon nitride: a) without oxidation; b) after 10 hours oxidation; c) after 20 hours oxidation.

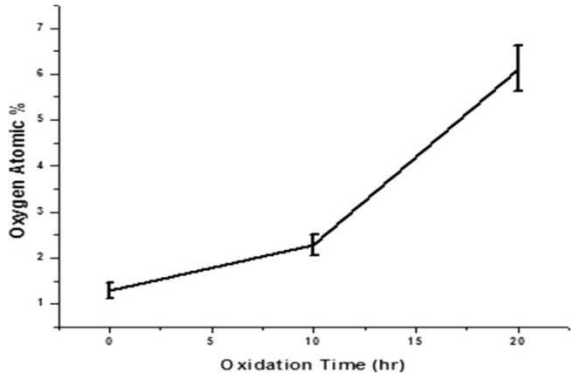

Figure 4.6 - Oxygen atomic percent present in the powders with respect to their oxidation time.

For further analysis of oxidized powders, the high-resolution transmission electron microscopy (HRTEM) was carried out. Based on HRTEM results, an amorphous SiO_2 film was observed on the silicon nitride powder particles after oxidation (Figure 4.7). No film was detected on particle surface of un-oxidized powder. In case of 10 hours oxidized powders, up to 1.5 nm thick SiO2 film was witnessed. Up to 4 nm thick silica (SiO2) was found on powders oxidized for 20 hours at 1000 °C. The thickness of this amorphous layer increased with the increase of oxidation time. The thick film might act as a protective layer on the particles and slows down further oxidation. The formation of SiO_2 layer on the silicon nitride

powder particles was a result of a reaction between Si_3N_4 and O_2 at a higher temperature (Equation 4.1)[110].

$$Si_3N_4 + 3O_2 \xrightarrow{1000\ ^\circ C} 3SiO_2 + 2N_2 \text{ ---------- Equation 4.1}$$

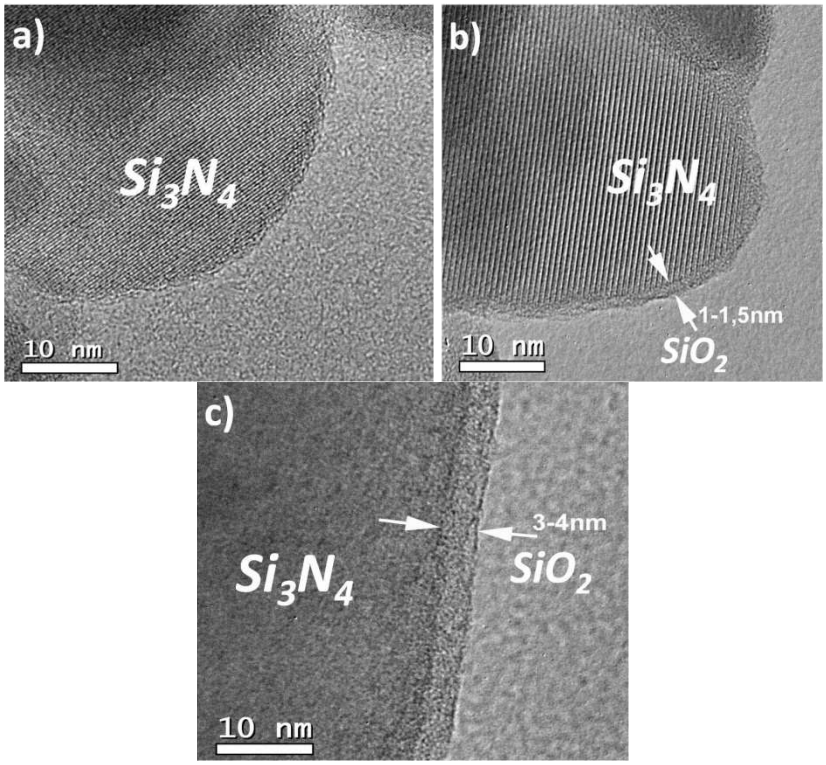

Figure 4.7 - HRTEM results of starting powders: a) before oxidation, Batch-I; b) after 10 hours oxidation, Batch-II; c) after 20 hours oxidation, Batch-III.

X-ray diffraction (XRD) was performed to identify phases in starting powders before and after oxidation. XRD results of as received starting powder Si_3N_4 confirmed the presence of only α phase according to the JCPDS PDF (01–076-1407) (Figure 4.8). XRD could not find any structural or phase change in the powders after the 10- and 20-hours of oxidation. A bump of overlapped peaks (no sharp peak with high intensity except a peak of crystalline α - Si_3N_4 phase, indicated with a red circle) was observed in the range of 2θ = 15–22° in XRD spectra. (Figure 4.8). The bump behavior in spectra represents the presence of an amorphous phase. This amorphous phase was SiO_2, which was formed as a result of oxidation 1000 ºC. XRD detected the main Brag's peaks of silicon oxynitride (Si_2N_2O) in the same range of 2θ = 15–22° after the sintering process. It confirms that SiO_2 was formed after the oxidation (Figure 4.9). The amount of amorphous SiO_2 phase is less than the threshold amount for detection by XRD. So, no significant peak for SiO_2 was observed in the oxidized powders.

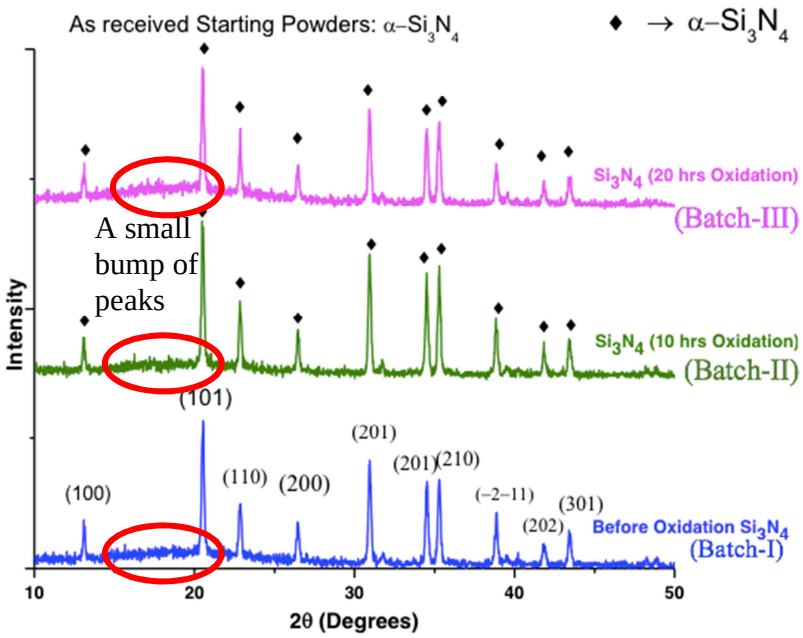

Figure 4.8 - X-ray Diffractograms of as received starting powder Silicon Nitride before and after oxidation.

4.3. Investigation of sintered samples

4.3.1. Structural investigation

A few new phases were detected in the sintered samples by XRD. The XRD spectra revealed, the structural peaks of the α phase and β phase of Si_3N_4, silicon oxynitride (Si_2N_2O), and ZrO_2 phases were detected (Figure 4.9). ZrO_2 is hypothesized as the contamination originated from the milling media (ZrO_2 balls). The α Si_3N_4: JCPDS PDF (01-076-1407), β Si_3N_4: JCPDS PDF (00-33-1160), Si_2N_2O: JCPDS PDF (00-47-1627) and Y- doped ZrO_2: JCPDS PDF (00-83-0944) were identified. Y-doped zirconia is present due to the Y_2O_3 as a sintering additive [111]. The complete transformation of α to β phase of Si_3N_4 was found, and the α grains were dissolved in a liquid phase and precipitated as β phase in the samples sintered at 1700 ˚C. On the other hand, samples sintered at 1500 ˚C, the incomplete transformation was observed because the sintering temperature was lower than the transformational temperature [112] [113].

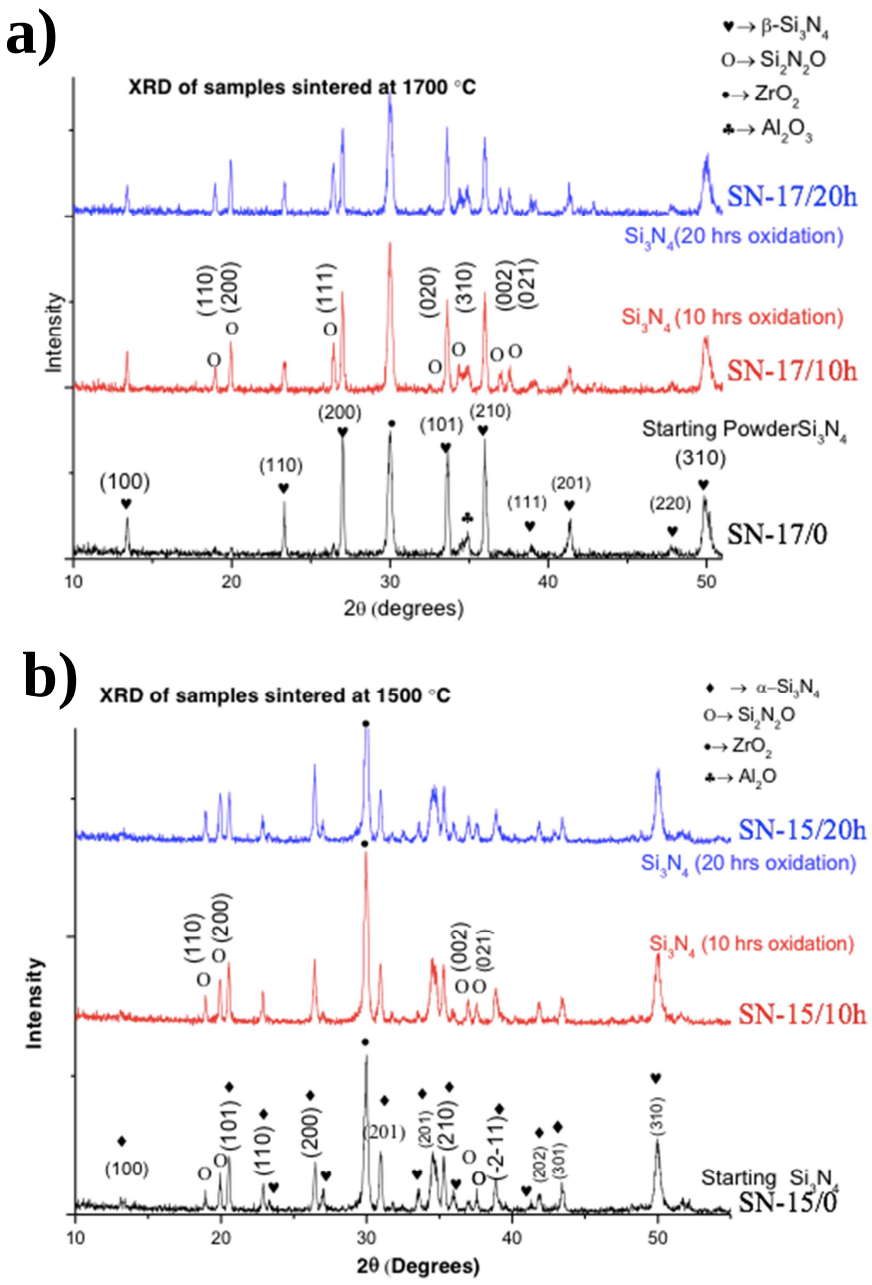

Figure 4.9 - XRD spectra of sintered samples: a) samples sintered at 1700 °C and b) samples sintered at 1500 °C.

4.3.2. Mechanism of in-situ growth of Si_2N_2O and α- to β- Si_3N_4 transformation

Figure 4.10 illustrates the mechanism of the *in-situ* growth of Si_2N_2O in the silicon nitride matrix. Si_2N_2O was formed from the reaction of SiO_2 and Si_3N_4 in the presence of the liquid phase. The oxidized powders contained oxygen, which caused the formation of Si_2N_2O in the presence of the liquid phase.

In the first stage, the SiO_2 formed on the Si_3N_4 powder particles' surface according to Equation 4.1. In the second stage, Si_2N_2O was formed as a result of a reaction between SiO_2 and Si_3N_4 in the presence of an N_2 gas environment during the sintering process (Equation 4.2)[114][115][116].

$$SiO_2 + Si_3N_4 \rightarrow 2Si_2N_2O \text{ ---------- Equation 4.2}$$

During the sintering process, an Al-Y-O-N based supersaturated liquid was formed, and the reaction between SiO_2 and Si_3N_4 occurred (Equation 4.2). In the first step, Si_3N_4 and SiO_2 were dissolved into the liquid phase as Si, N, and O. Then in the second step, these (Si, N, O) diffused through the liquid phase towards the growth of Si_2N_2O and finally attached to the growing Si_2N_2O crystals. Tsai and Raj [114] proposed a model for the Si_2N_2O growth through the dissolution of Si_3N_4 in a glassy phase based on Mg-Si-O-N. The proposed model by Tsai and Raj, with a slight modification, validates the growth mechanism of Si_2N_2O in the present study.

Moreover, α- to β- Si_3N_4 transformation also happened simultaneously with the formation of Si_2N_2O. During the sintering, a supersaturated liquid phase based on Si-Al-Y-O formed, and α-Si_3N_4 was dissolved in this liquid and re-precipitated as a β phase. This hypothesis supports Hampshire and Jack's work [117].

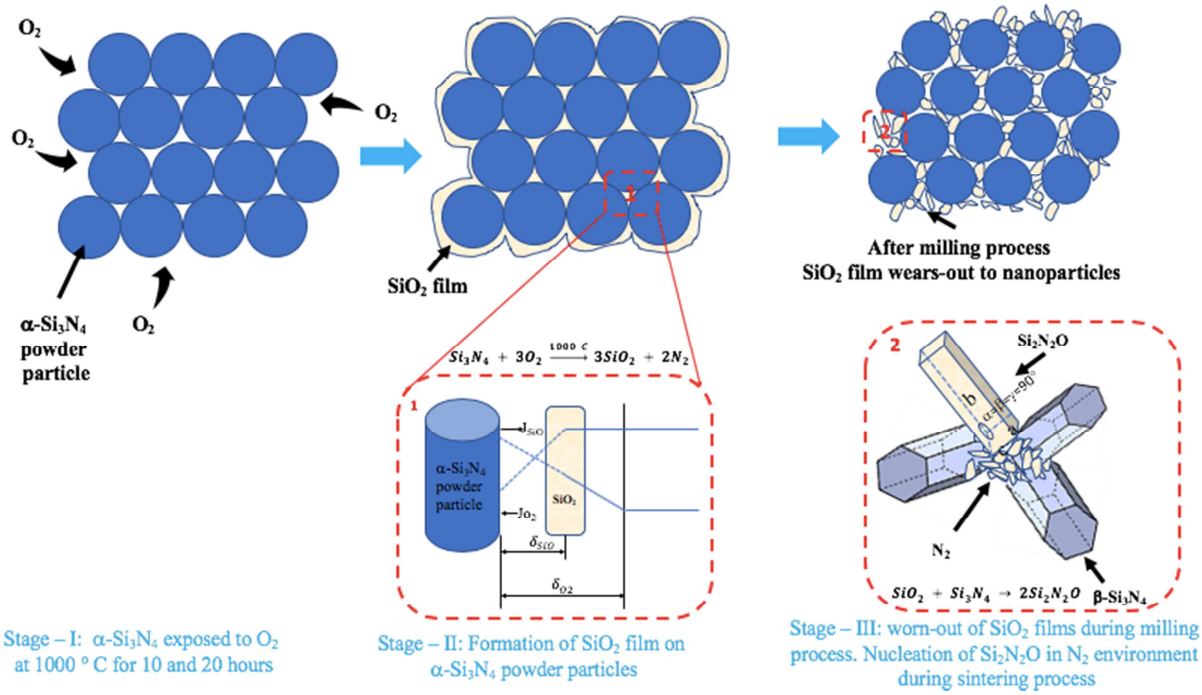

Figure 4.10 - Illustration of mechanism of in-situ growth of Si_2N_2O in Si_3N_4 matrix (Author's work).

The phase composition was calculated from the XRD data using Full Pattern Matching EVA software. Based on the calculation, the maximum content of β- Si_3N_4 was found to be ~ 78 wt% in an un-oxidized sample (SN-17/0), sintered at 1700 °C (Table 4.3). The overall obtained amount of β-phase decreased with the oxidation time (Figure 4.11 – a) while the Si_2N_2O phase increased linearly with the oxidation time (Figure 4.11 – b). These findings are consistent with the study of Park et al. [118]. They also showed that β- phase decreased with the increase of Si_2N_2O.

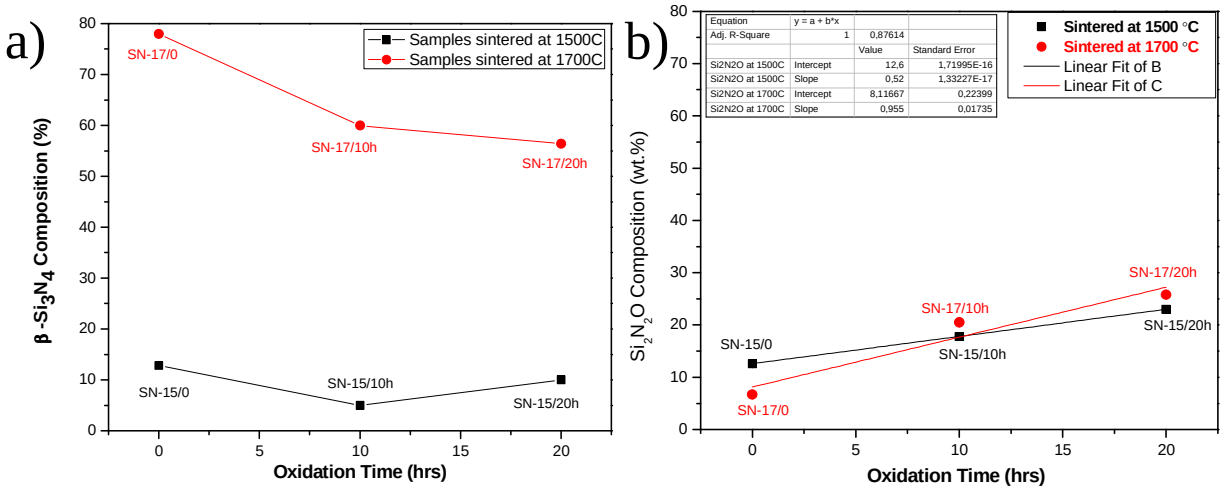

Figure 4.11 – The composition of different phases in the examined systems: a) β - Si_3N_4 phase and b) Si_2N_2O phase.

In samples sintered at 1700 °C, the Si_2N_2O phase increased and β- Si_3N_4 decreased simultaneously (Figure 4.12 – a). The amounts of Si_2N_2O and β-Si_3N_4 phases could be optimized with optimizing the oxidation time; the graph (Figure 4.12 – a) shows Si_2N_2O increases and β- Si_3N_4 decreases equally with increasing oxidation time. In the sample sintered at 1500 °C, the growth rate of the Si_2N_2O phase was slightly higher than the transformation rate of α to β- phase of Si_3N_4 (Figure 4.12 – a). It was hypothesized that the Si_2N_2O's formational temperature was lower than α to β transformational temperature while the Si_2N_2O was almost a similar amount at 1500 °C and 1700 °C. The 23 wt% and 25 wt% of Si_2N_2O was detected in the sintered samples at 1500 °C and 1700 °C, respectively, while β-content was different at both temperatures; this was the indication that Si_2N_2O was formed at a lower temperature than the α to β transformational temperature. The crystallite size of β-phase in all samples decreased with oxidation time, but the crystallite size of Si_2N_2O increased with the increasing oxidation time (Table 4.3). A higher content of oxygen in

starting powders favored the formation of Si_2N_2O and hindered the crystallite growth of β-Si_3N_4.

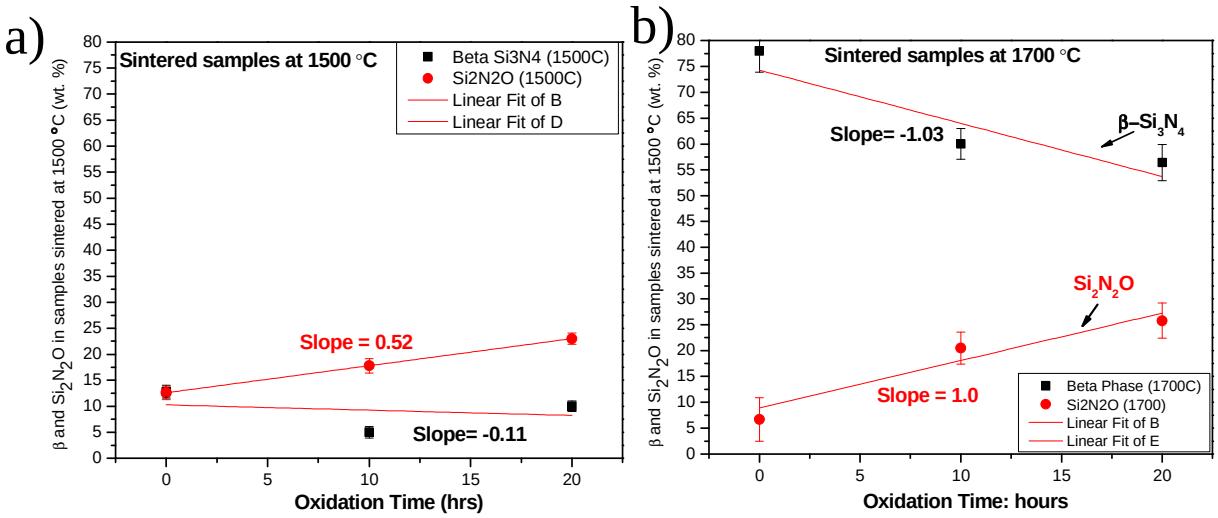

Figure 4.12 - β - Si_3N_4 and Si_2N_2O phases composition in the systems: a) in samples sintered at 1500 ℃ and b) in samples sintered at 1700 ℃.

Based on XRD results, the *in-situ* grown Si_2N_2O phase was an orthorhombic structure, and its amount was a function of oxidation time. A few researchers reported the decomposition of Si_2N_2O phase above 1500 °C (Equations 4.3 and 4.4) due to the addition of sintering aids of Li_2O above their threshold amount [119][120][121].

$$3Si_2N_2O\ (s) \rightarrow 2Si_3N_4(s) + 3SiO(g) + N_2(g) \text{ ------ Equation 4.3}$$

$$2Si_2N_2O(s) + 3O_2(g) \rightarrow 4SiO(g) + 2N_2(g) \text{ ------ Equation 4.4}$$

The current study contradicts such results, no decomposition of Si_2N_2O was observed above 1500 °C; it might be due to the proper selection of sintering aid and their optimized amount. Mitomo et al. [122] reported that high pressure of N_2 (98 to 980 kPa) suppresses the decomposition of Si_2N_2O and the reaction (Equation 4.4) becomes reversible at high pressure of N_2 and in this way the Si_2N_2O is preserved. In the present work, the N_2 pressure was higher (20 MPa) than the suggested pressure of N_2 (0.98 MPa) by Mitomo et al. [122]. So, the adopted parameters for sintering were suitable to preserve the Si_2N_2O in the current work.

4.4. Mechanical properties

4.4.1. Vickers hardness

Figure 4.13 shows the Vickers hardness of sintered samples. The samples sintered at 1500 °C showed higher Vickers hardness than that of samples sintered at 1700 °C. A higher amount of α-Si_3N_4 was present in the samples 1500/0, 1500/10h, and 1500/20h than that of samples 1700/0, 1700/10h, and 1700/20h. The α-phase of Si_3N_4 is harder than the β-Si_3N_4. The α-Si_3N_4 has long stacking sequence ABCDABCD... while β-Si_3N_4 has ABAB…[13]. Longer stacking sequence results in the α-Si_3N_4 higher hardness than the β-Si_3N_4 [123]. The higher content and smaller grain size of α-phase in samples sintered at 1500 °C (1500/0, 1500/10h, and 1500/20h) contributed to the hardening of the material, so higher hardness values were observed in these samples. These Vickers hardness values of the investigated systems are much higher than many reported values in the literature [46]–[49], [53], [55], [124]. The higher Vickers hardness was attributed to higher density and presence of hard phase Si_2N_2O in the systems.

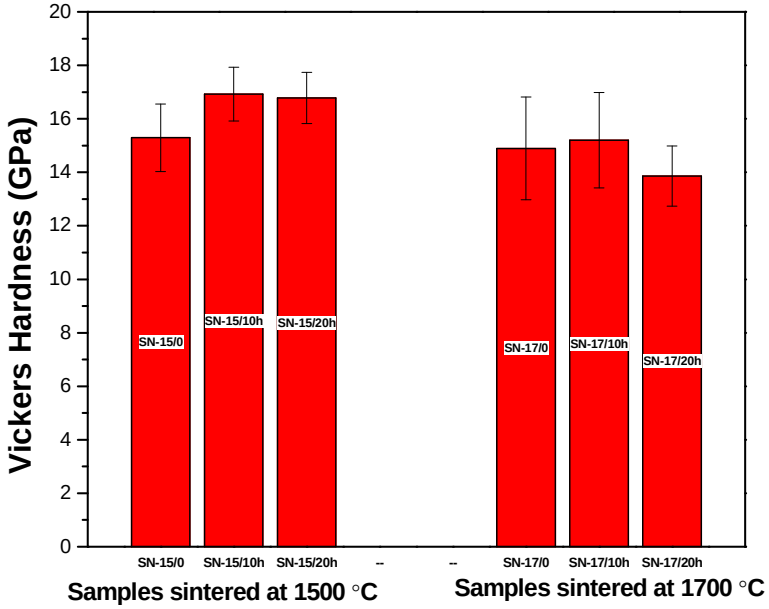

Figure 4.13 - Vickers hardness (HV) values of samples sintered at 1500 ℃ and 1700 ℃.

4.4.2. Flexural Strength

The α/β ratio and Si_2N_2O phases influence the mechanical properties. The 4 – point bending strength of samples sintered at 1500 ˚C was in the range of 300 ÷ 320 MPa (Figure 4.14). This value decreased slightly with increasing oxidation time. The samples sintered at 1700 ˚C exhibited two times higher 4 – point bending strength than that of samples sintered at 1500 ˚C, and the values are within the range of 600 ÷ 775 MPa (Figure 4.14). Un-oxidized sample (1700/0) with the highest 78% of β-Si_3N_4 phase showed the highest value and followed by

1700/10h and 1700/20h. The flexural strength started decreasing with the oxidation time. The decrease in flexural strength is because of the reduction in β-phase in the samples. The β-phase is rod-like elongated hexagonal grains which act as a reinforcing agent in the matrix and strengthen the composite. The decrease in strength can be seen with the increase of oxidation time in Figure 4.14. The ratio β-Si_3N_4/Si_2N_2O is a vital factor to optimize the flexural strength. The desired flexural strength can be achieved by optimizing the ratio β-Si_3N_4/Si_2N_2O. The ratio β-Si_3N_4/Si_2N_2O is connected to the oxide phases in the starting powders.

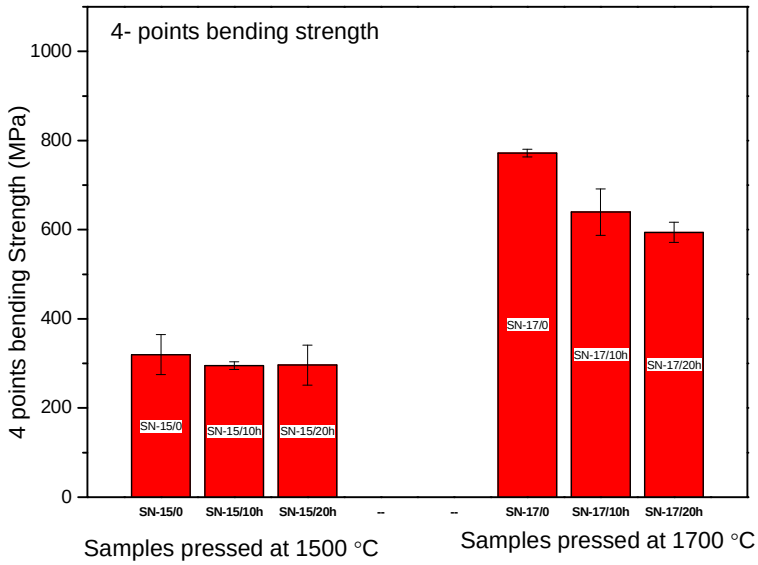

Figure 4.14 - 4- point bending strength of samples sintered at 1500 ℃ and 1700 ℃.

A similar tendency for 3 – point bending strength was observed in all sintered samples (Figure 4.15). The β-Si_3N_4 phase decreased with the increase of oxidation time, which lowered the samples' strength. The strength of sample 1700/0 is higher because it has the highest content of β phase. The reason for reduced flexural strength for samples sintered at 1500 ˚C is porosity and incomplete transformation α to β phase of Si_3N_4. The presence of internal porosity was revealed by the morphological study of fractured surfaces of all samples sintered at 1500 ˚C (Figure 4.18), and the porosity contributed to decreasing the flexural strength. The fracture was nucleated from the porous sites and propagated through inter-granular and trans-granular sites.

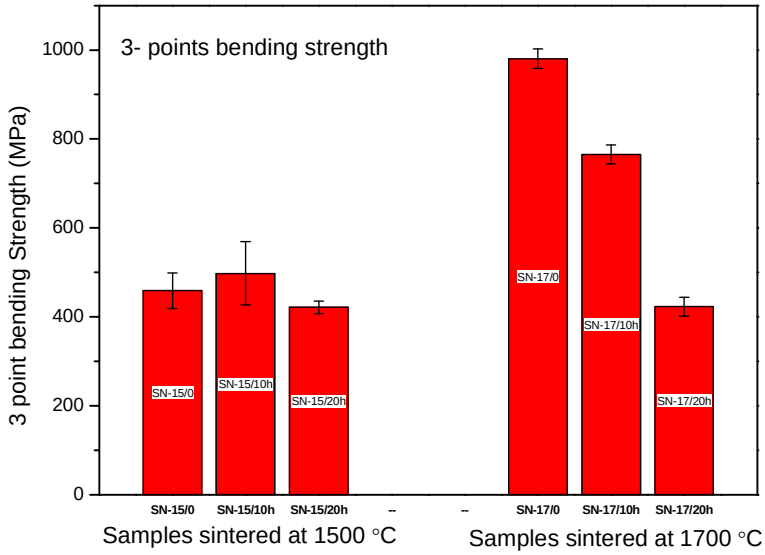

Figure 4.15 – 3 – point bending strength of samples sintered at 1500 ℃ and 1700 ℃.

4.4.3. Young's Modulus

As the elastic modulus (E) identifies the stiffness of material, it was measured in the range between 240 and 260 GPa (Figure 4.16). The elastic modulus depends on porosity, grain boundary phases, texture, and relative contents of α and β phases. The value for the samples sintered at 1500 ˚C was almost relative, and no effect of oxidation time on the elastic modulus was observed as compared to samples sintered at 1700°C. The elastic modulus of 1700/0, 1700/10h, and 1700/20h decreased with the increase in oxidation time. It was witnessed a similar decreasing tendency with the increasing oxidation time as the samples' bending strength values.

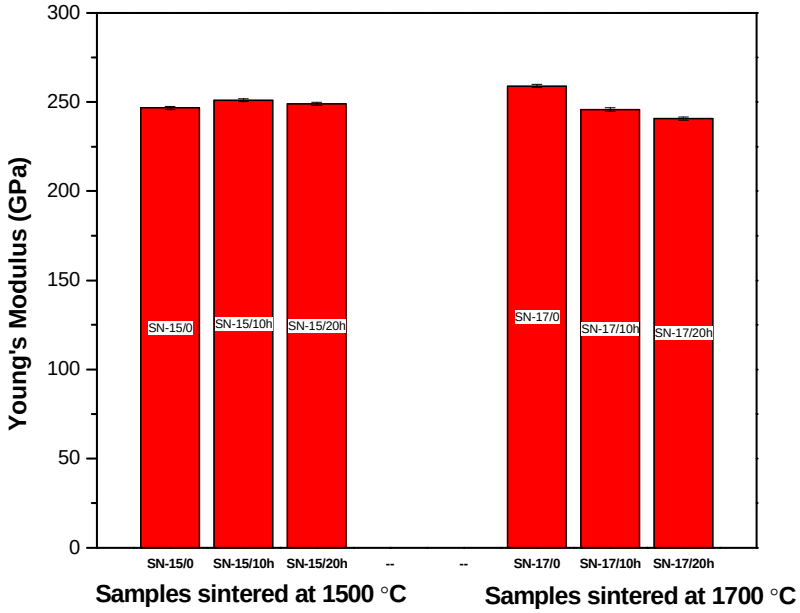

Figure 4.16 - Young's modulus (E) of samples sintered at 1500 ℃ and 1700 ℃.

4.4.4. Indentation fracture resistance (K_{IIFR})

The indentation fracture resistance (K_{IIFR}) values of all the samples sintered at 1500 ˚C were in the range of 10 ÷ 11 MPa·m$^{1/2}$ (Figure 4.17). The sample SN-1500/20h showed the highest fracture resistance among the samples sintered at 1500 ˚C.

The systems sintered at 1700 ˚C exhibited fracture resistance in the range of 8 ÷ 13 MPa·m$^{1/2}$. The sample SN-1700/0 presented the highest fracture resistance, 13 MPa·m$^{1/2}$, among all the samples. The reason for the highest resistance might be the maximum amount of β phase (78 wt%) present in the sample SN-1500/20h among all samples (Figure 4.11 – b). β - Si_3N_4 phase contributes to toughness due to its elongated hexagonal structure. At the same time, SN-17/20h possess a higher amount of β phase (56.4 wt%) than the systems sintered at 1500 ˚C but displayed the lowest value of fracture resistance. In general, high density and high amount β phase in the structure result in higher fracture resistance. Here, the obtained results have significant scattering, and it is difficult to conclude the relation of these values with microstructure features or processing techniques.

Park et al. [118] reported the higher indentation fracture resistance (K_{IIFR}) with a higher amount of Si_2N_2O in the sample, but this study disagreed with this fact and reported the decrease in indentation fracture resistance with increasing content of Si_2N_2O. The obtained values of samples sintered at 1700 °C are higher than the reported values of silicon nitride ceramics in the literature [71] [52][46].

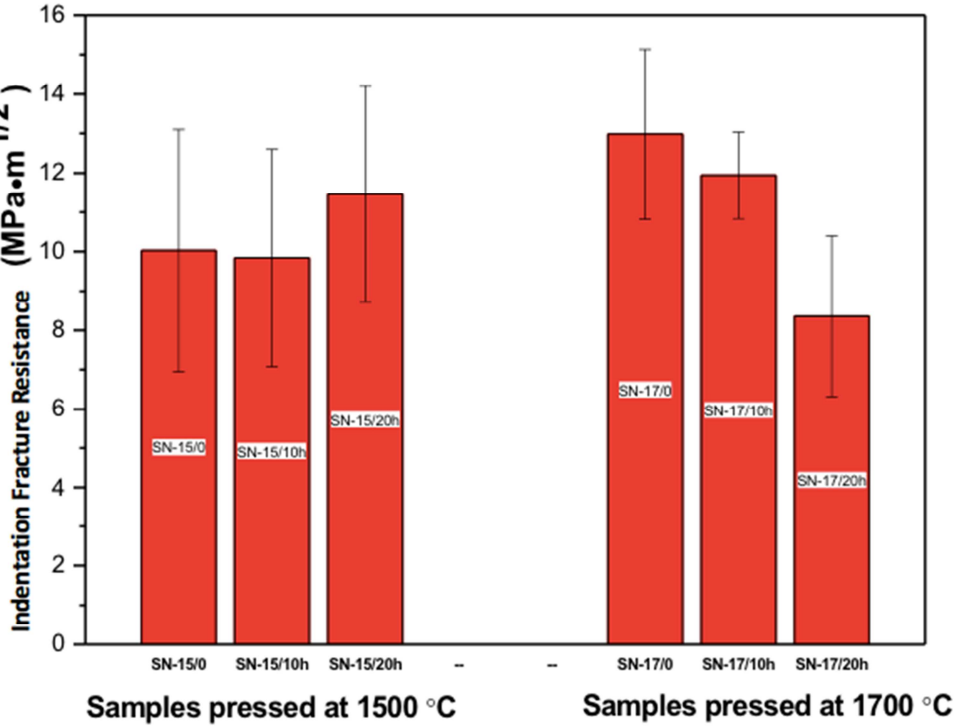

Figure 4.17 – Indentation fracture resistance of systems sintered at 1500 ℃ and 1700 ℃.

4.4.5. Fractographic analysis of sintered samples

Figure 4.18 shows the SEM images of fractured surfaces of sintered samples during the bending tests. Samples sintered at 1500 °C consists mainly of α-Si_3N_4, Si_2N_2O and traces of β-Si_3N_4 grains. In comparison, samples sintered at 1700 °C consists mainly of β- Si_3N_4 grains and Si_2N_2O. It is evident that samples sintered at 1500 °C contains more porosity than that of samples sintered at 1700 °C. The SEM images also reveal the nature of fracture while measuring the flexural strength. The fracture was inter- and transgranular. Due to the smaller grain size and porosity in samples sintered at 1500 °C, the crack-path was shorter than that of samples contain larger grains like β- Si_3N_4. Overall β- Si_3N_4 is tougher than α- Si_3N_4, β-Si_3N_4 grains act as reinforcement in the matrix. There is also evidence of pulling-out of β grains. The β grains fractured when the stress reached the threshold value of the strength of β grains.

SEM images of fractured surfaces of samples sintered at 1500 °C	SEM images of fractured surfaces of samples sintered at 1700 °C

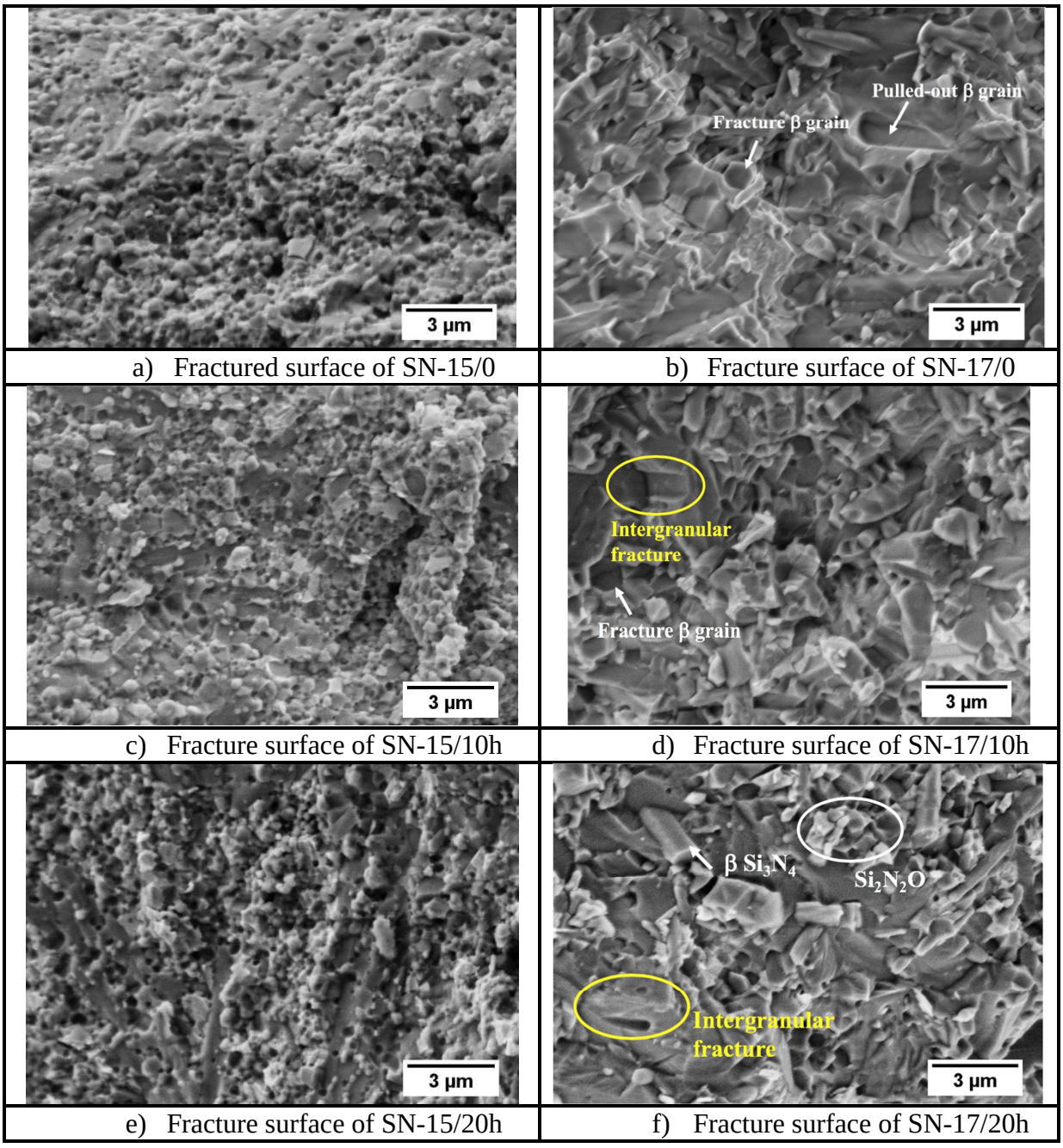

a) Fractured surface of SN-15/0

b) Fracture surface of SN-17/0

c) Fracture surface of SN-15/10h

d) Fracture surface of SN-17/10h

e) Fracture surface of SN-15/20h

f) Fracture surface of SN-17/20h

Figure 4.18 – SEM images of fractured surfaces of sintered samples

4.5. Tribological Properties

4.5.1. Coefficient of friction (COF)

Figure 4.19 shows the coefficient of friction (COF) values as a function of sliding distance for six types of samples. The sample sintered at 1500˚C (SN-15/0) showed the maximum friction coefficient of 0.809 ± 0.019. In contrast, the sample sintered at 1700˚C (SN-17/0) exhibited the minimum friction coefficient of 0.650 ± 0.041. In general, there are three identified stages

in the tribological process as sliding proceeds, and those stages are the so-called *run-in stage*, *steady-state stage*, and *catastrophic stage* [125]. The *run-in stage* is the first stage that occurs when the wear process starts, and this stage lasts for a short period of time. During this stage, the sliding surfaces act in accordance with each other, that normal load is evenly distributed over the surfaces. The wear rate is relatively high during this stage of the tribological process. During the *steady-state stage*, the friction and wear rate are usually low and almost stable and last until the severe surface damage starts. During this stage, the measured frictional forces and wear rate are considered important in characterizing the mating-surfaces' long-standing tribological properties. In the *catastrophic stage*, the wear rate and surface damage become severe, and consequently, components fail.

In my case, I defined 0 - 40 m of sliding distance as a *run-in* stage and 40 – 1000 m as a steady-state. The average friction coefficients and average wear rates were measured not only in the running stage, but in the steady state conditions, as well. In the case of systems sintered at 1500 ˚C (SN-15/0, SN-15/10h, and SN-15/20h), the friction coefficient (COF) during the *run-in* stage was lower than the COF during the *steady-state* conditions (Figure 4.19 – c).
In the case of systems sintered at 1700 ˚C (SN-17/0, SN-17/10h, and SN-17/20h), the situation was the opposite; the COF during the run-in stage was higher than the COF during the steady-state conditions (Figure 4.19 - c).

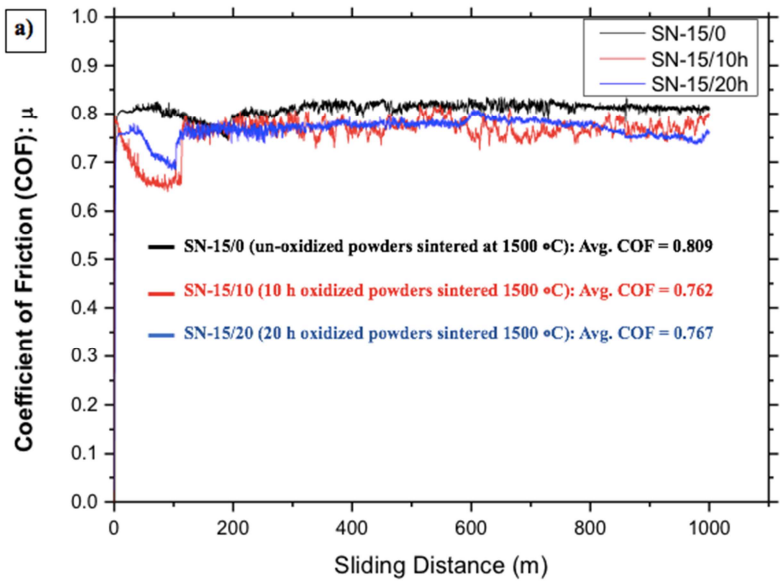

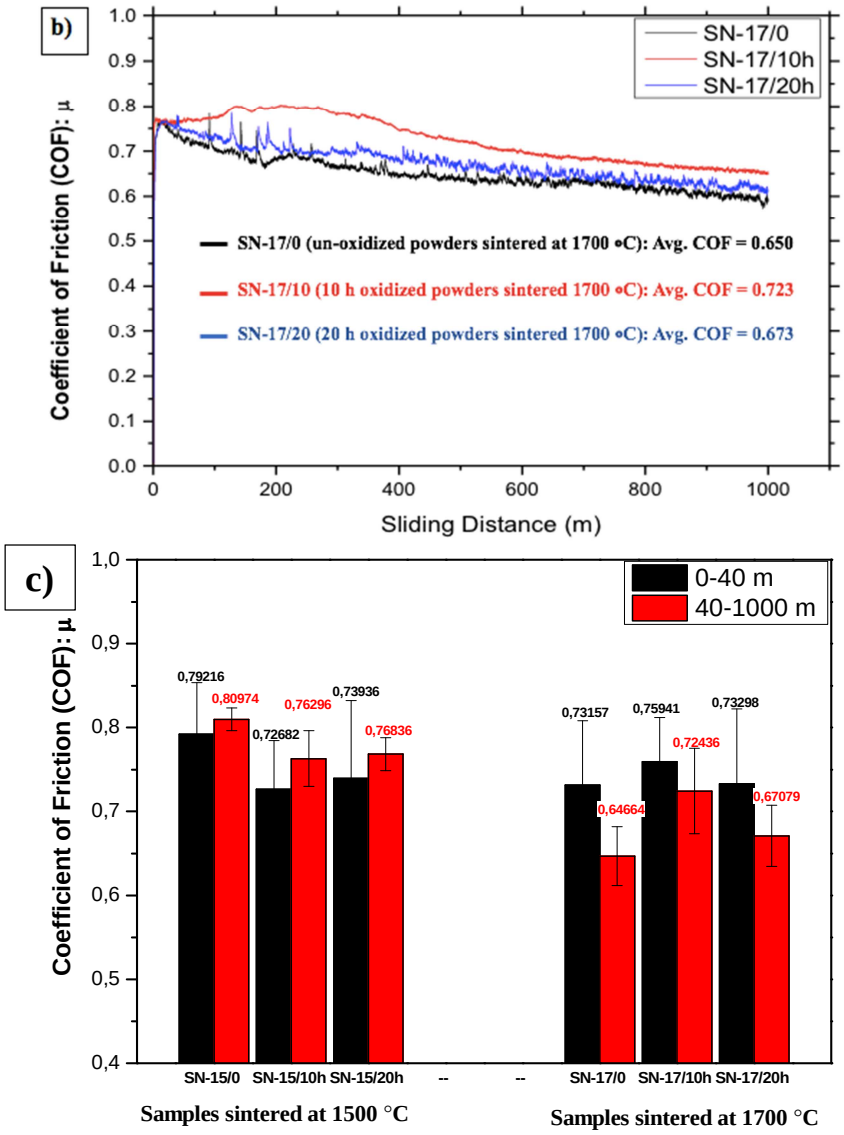

Figure 4.19 - Coefficient of friction (COF) of sintered samples: a) COF of samples sintered at 1500 ℃ SN-15/0, SN-15/10h and SN-15/20h; b) COF of samples sintered at 1700 ℃ SN-17/0, SN-17/10h and SN-17/20h; c) COF of sintered samples in run-in (0-40 m) and steady-state stage (40-1000 m).

4.5.2. Wear rate

The average wear rate during the run-in stage (0 – 40 m) was seven times higher than the wear rate during steady-state conditions (40 – 1000 m). The wear rates of the investigated systems are given in (Figure 4.20). It was observed that the steady-state conditions were dominant from 40 – 1000 m in the sliding distance and the catastrophic stage is far from this point.

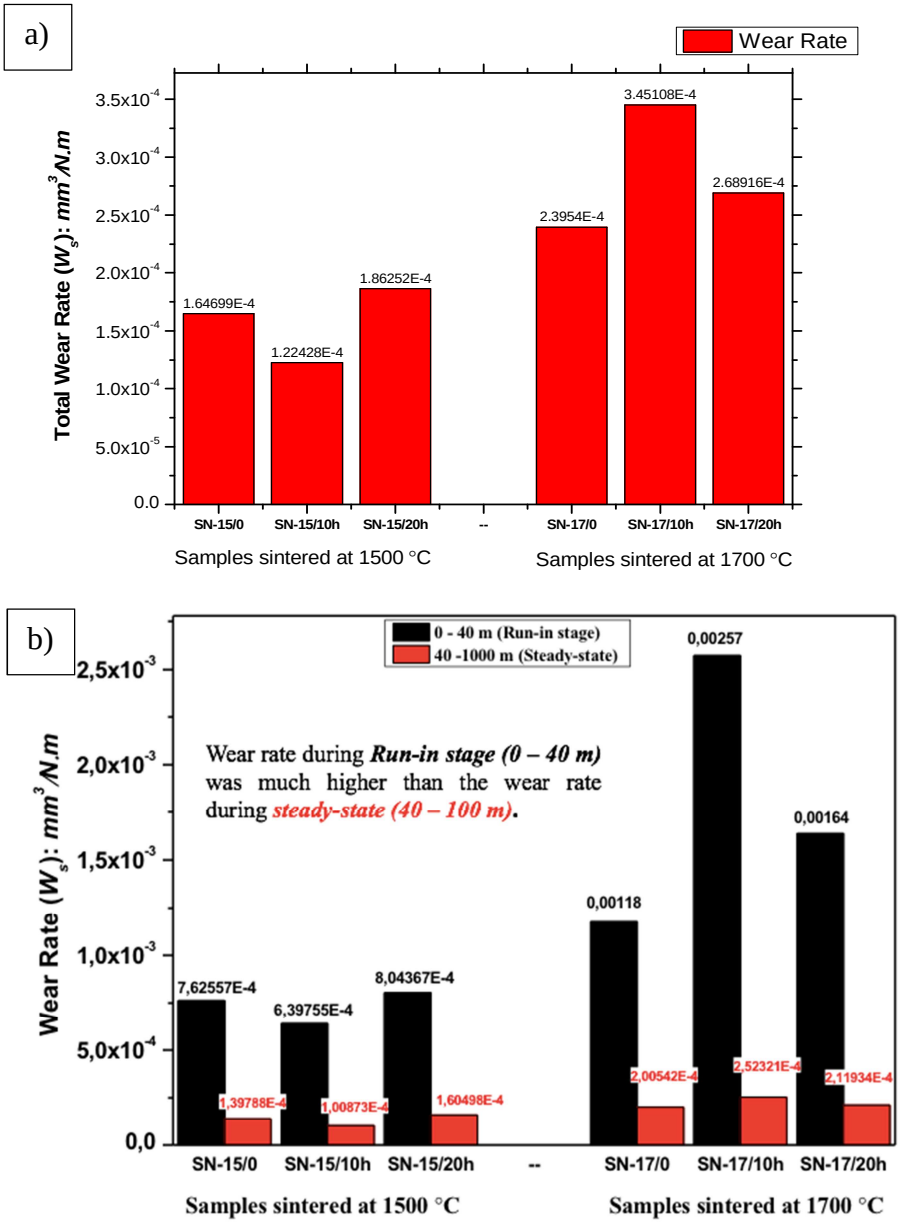

Figure 4.20 - Wear rate of sintered samples: a) Total wear rate of samples; b) Wear rates during the run-in stage (0-40 m) and steady state (40-1000m).

The wear rate was calculated for every 100 m of sliding distance. The wear rate was very high during the *run-in* stage (0-40 m), and it decreased exponentially after the run-in stage (Figure 4.21). Stable wear started at 400 m of sliding in systems sintered at 1500 ˚C, while in the case of samples sintered at 1700 ˚C, the constant wear began after 200 m of sliding. The primary reason for the constant wear was the Hertzian contact pressure, which decreased due to the increase of the total contact area, resulting in a lower wear rate and kept the systems operating in a steady wear stage. The secondary reason was the formation of tribo-film, which was worn-out when the frictional forces exceeded the critical limit. Throughout the sliding distance, the wear rate was constantly low. Overall, the wear rates for samples sintered at 1500 ˚C were lower than that of samples sintered at 1700 ˚C. The lowest wear rate with the

value of 1.224 x 10^{-4} was measured for sample SN-15/10h, and the highest wear rate with the value of 3.451 x 10^{-4} was observed for sample SN-17/10h. The lower wear rate may be due to the amount of α - Si_3N_4 phase in the structure. For instance, the fraction of α phase was highest in the sample SN-15/10h, and its wear rate was the lowest among all systems.

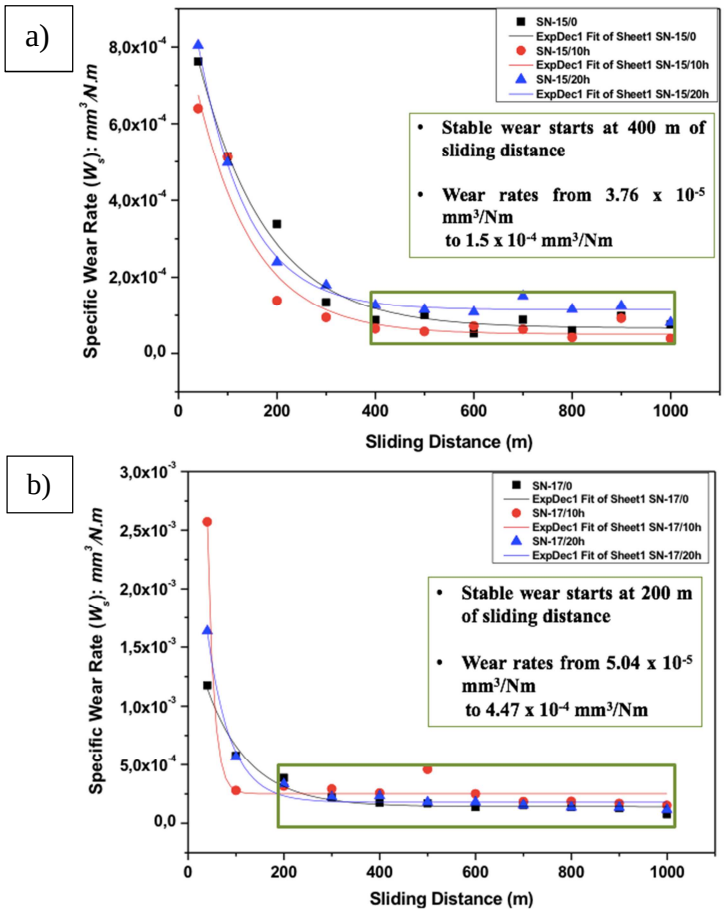

Figure 4.21 - Wear rates at every 100 m distance up to 1000 m, the wear rate decreased exponentially after 100 m sliding distance: a) samples sintered at 1500 ℃ and b) samples sintered at 1700 ℃.

4.5.3. Wear Mechanism

Figure 4.22 is a SEM image of the wear track, and the labeled areas identify the types of wear occurred. The main identified wear mechanisms in all examined samples were a tribo-chemical reaction and a mechanical wear (abrasive wear). Similar wear mechanisms were observed in all systems, so only a few SEM images of wear tracks were presented here. The tribo-film was formed due to the tribo-chemical reaction, and the area is characterized by a relatively flat surface. The mechanical wear (abrasive wear) area is characterized by a rough surface and accumulated wear debris. The tribo-chemical reactions form a tribo-film on the surface, and that film was partially removed when the load and frictional forces exceeded the

threshold limit during the sliding. Figure 4.22 shows the example of such tribo-film and their following fracture on the worn surfaces.

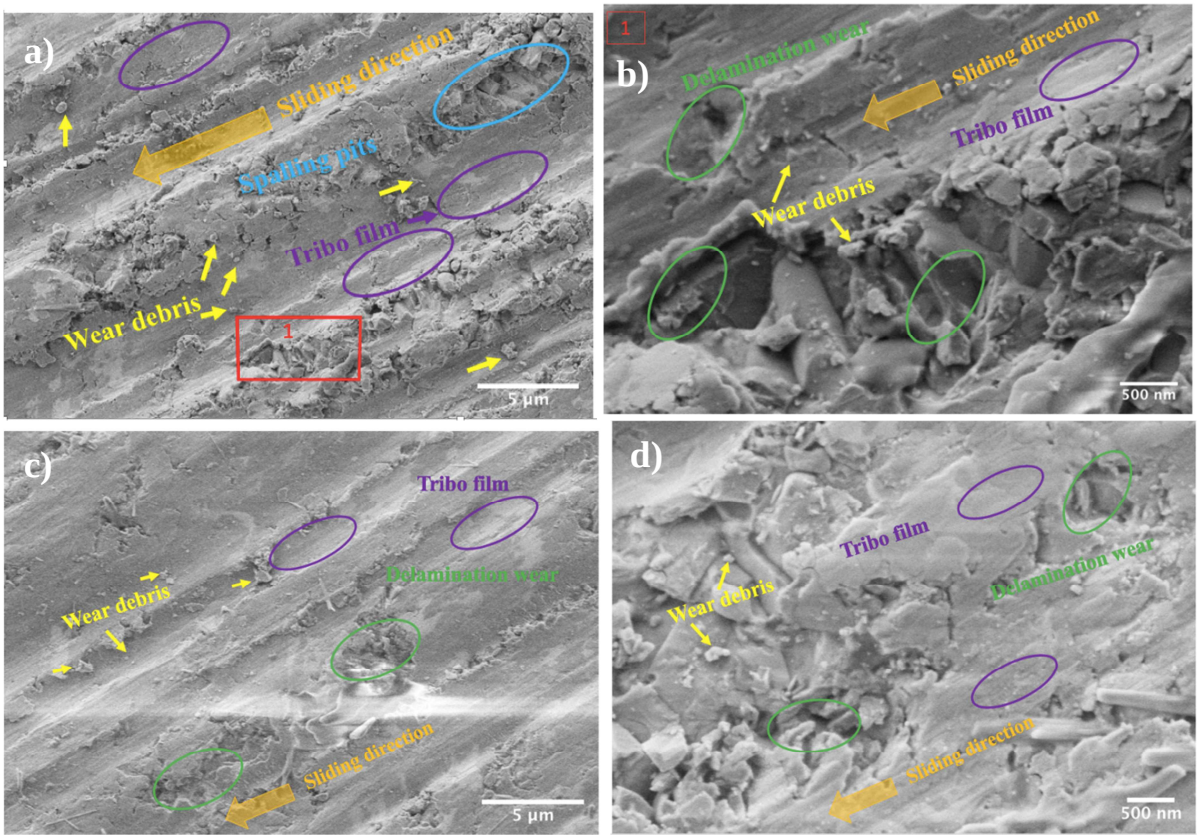

Figure 4.22 - SEM image of wear track and the worn areas are labeled with arrows and elliptical circles to identify its respective wear mechanisms: a) wear track of SN-17/0 and b) wear track of SN-17/0 at higher magnification; c) wear track of SN-17/20h and d) wear track of SN-17/20h at higher magnification.

A material's reaction to a wear environment does not merely depend on its intrinsic properties. Rather, it is a response to the complex chemistry of stresses imposed by a counter-part in the tribological environment [126]. The contact geometry, speed, load, temperature, lubrication, and humidity are also important variables in the tribosystem to measure the wear properties of a material. Materials engineers need some models to predict the response of a material in a tribological system. For this purpose, several analytical models have been developed to rank materials based on their intrinsic properties [127][128][129][130][131]. All the models are similar and assume that subsurface lateral fracture is responsible for material removal during abrasive wear. Evans and Marshall [128] developed an analytical model for lateral-cracks chipping to analyze the mechanism of material removal rate (ΔV) in brittle ceramics, in which material removal is caused by abrasive wear. The model is described by the following equation (Equation 4.5):

$$V = \alpha \frac{P_N^{9/8}}{K_{IIFR}^{1/2} H_V^{5/8}} \left(E/H_V\right)^{4/5} \ell$$ ---------- Equation 4.5

Where, V is material removal rate (volume loss), α is the material-independent constant, P_N is the normal load, K_{IIFR}, H_V, and E are the indentation fracture resistance, Vickers hardness, and Young's modulus, respectively, of the abraded material, and ℓ is the sliding distance. By gathering all of the material-specific constants into one parameter, β, the equation (Equation 4.5) can be expressed as:

$$V = \alpha P_N^{9/8} \ell \beta$$ ---------- Equation 4.6

Where,

$$\beta = \frac{\left(E/H_V\right)^{4/5}}{K_{IIFR}^{1/2} H_V^{5/8}}$$ ---------- Equation 4.7

The relationship between the parameter β and the wear rate is shown in Figure 4.23.

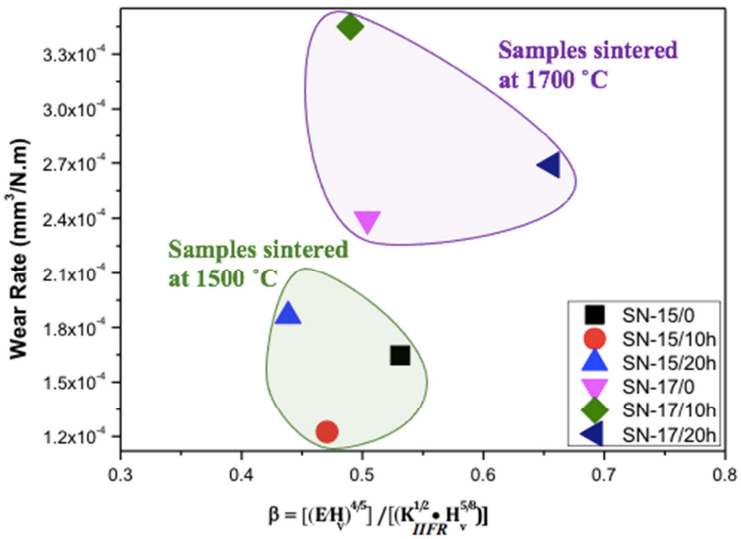

Figure 4.23 - Wear rate vs β parameter of sintered samples.

The graph shows that examined systems have no consistent correlation between wear rate and β parameter. Some researchers have found a good correlation between wear rate and the β parameter of the investigated systems [132]. My findings on the correlation between wear rate and β parameter have a good agreement with the studies of Doğan and Hawk [126]. They also found deviations from this model in their studies. It is difficult to conclude that the wear rate

is dependent on one property of the system. It is also noted that the systems with low COF did not demonstrate a lower wear rate. The samples which contained a comparatively higher amount of α-Si_3N_4 showed a high COF, but at the same time, they exhibited a low wear rate. The low wear rate was probably due to the high hardness of α - Si_3N_4 present in the samples.

5. Si_3N_4 + 3 wt% MWCNTs composites

After developing and investigating monolithic silicon nitride systems (as discussed in previous chapter 4), this chapter is dedicated to the development of silicon nitride reinforced with multi-walled carbon nanotubes (MWCNTs). This chapter will give an overview on the preparation method, microstructural analysis, mechanical and tribological properties of composites.

5.1. Preparation of Si_3N_4 + 3 wt% MWCNTs composites by HIP

5.1.1. Starting powders

The starting powders, α-Si_3N_4 (Ube, SN-ESP) [107], used for the development of this composite, were in three forms:

a) As received, α-Si_3N_4 powder (un-oxidized) used as a reference (SN-CNT/0).
b) 10 h oxidation of α-Si_3N_4 powder at 1000 ˚C in ambient air environment (SN-CNT/10).
c) 20 h oxidation of α-Si_3N_4 powder at 1000 ˚C in ambient air environment (SN-CNT/20).

The oxidation process of starting powders has been discussed in chapter 5.

5.1.2. Sintering aids

Similar to previous composites, Al_2O_3 (supplier company: Alcoa, A16) and Y_2O_3 (supplier company: H.C. Starck, grade C) were used as sintering additives for the development of MWCNTs added composites. Before the milling process, the three powder mixtures were prepared. For each powder mixture, 4 wt% Al_2O_3, 6 wt% Y_2O_3, polyethylene glycol (PEG) surfactants, and ethanol were added.

5.1.3. Milling process

The wet milling process was carried out in a high attritor mill. Each batch was milled separately in a 750 cm^3 zirconia tank. The grinding media was ZrO_2 made balls with a diameter of 1 mm and the agitator discs. This milling process was performed with a high

rotation speed of 4000 rpm for 4 hours. The 3 wt% multi-walled carbon nanotubes (MWCNTs) were added in each batch of mixtures and mixed them for 30 minutes on the 600 rpm in attritor mill. After the addition of MWCNTs, the mixture was milled on a low rpm to avoid carbon nanotubes' damage. The MWCNTs were produced by the catalytic chemical vapor deposition (CCVD) method [133]. The amount of MWCNTs was chosen carefully. A large number of nanotubes may cause densification inhibition [58] [47], hinder α- to β-transformation of Si_3N_4, agglomeration of nanotubes, and induce porosity in sintered samples. The details of Si_3N_4 powders and their characteristics are given in Table 5.1.

Table 5.1 – Detailed information about the Si_3N_4 powders and their characteristics.

	SN-CNT/0	**SN-CNT/10**	**SN-CNT/20**
Oxidation time (h)	0	10	20
Oxidation temperature (˚C)	0	1000	1000
α–phase content (wt%)	>95	>95	>95
Crystallinity (wt%)	>99.5	>99.5	>99.5

5.1.4. Fabrication of green samples

Like previous composites, the powders were pressed in a metallic tool die by a hydraulic pressing under 200 MPa pressure for 5 seconds. These prepared samples are called green samples (bodies) before a firing process to eliminate retained ethanol (C_2H_6O) and PEG in samples. The green bodies process has been described by a schematic diagram above in chapter 4 and Figure 4.2.

5.1.5. Densification of powders by hot isostatic pressing (HIP)

The green bodies were subjected to the sintering process. The green bodies were sintered at 1700 °C under 20 MPa pressure in an N_2 gas environment for 3 hours as a holding time. The heating regime has been described earlier in chapter 4 and Figure 4.3. The heating rate was 25 °C/min. The detail of the sintered samples is given in Table 5.2.

These composite systems were sintered only at 1700 °C because this sintering temperature 1700 °C was optimum in achieving complete α-Si_3N_4 to β-Si_3N_4 transformation and better mechanical properties than that of applying lower sintering temperature.

Table 5.2 – Detailed information about the sintered samples of 3 wt% reinforced Si_3N_4 composites.

No.	SN-CNT/0	SN-CNT/10	SN-CNT/20
Oxidation Time (hrs)	0	10	20
Sintering Temperature (˚C)	1700	1700	1700
Apparent Density (g/cm^3)	3.161	3.199	3.235
Average size of β-Si_3N_4 (nm)	46.6 ± 4.4	48.1 ± 4.9	44.8 ± 4.8

5.2. Investigation of starting powders

5.2.1. Structural investigation

The X-ray diffractogram of starting α-Si_3N_4 powders with 3 wt% MWCNTs before and after oxidation are shown in Figure 5.1. No structural changes were observed, including phase transformation from α to β-Si_3N_4 before and after oxidation of starting powders at 1000 °C. The structural peaks correspond mainly to α-Si_3N_4 ZrO_2 and Y_2O_3, according to the JCPDS PDF (01-076-1407), JCPDS PDF (00-83-0944), and JCPDS PDF (01-089-5591), respectively. MWCNTs were supposed to have a peak at 2θ = 26.228 position according to JCP2:01-075-162, but the present amount of MWCNTs was below the detection limit of XRD. The zirconia (ZrO_2) contamination was originated from the grinding media during the milling process.

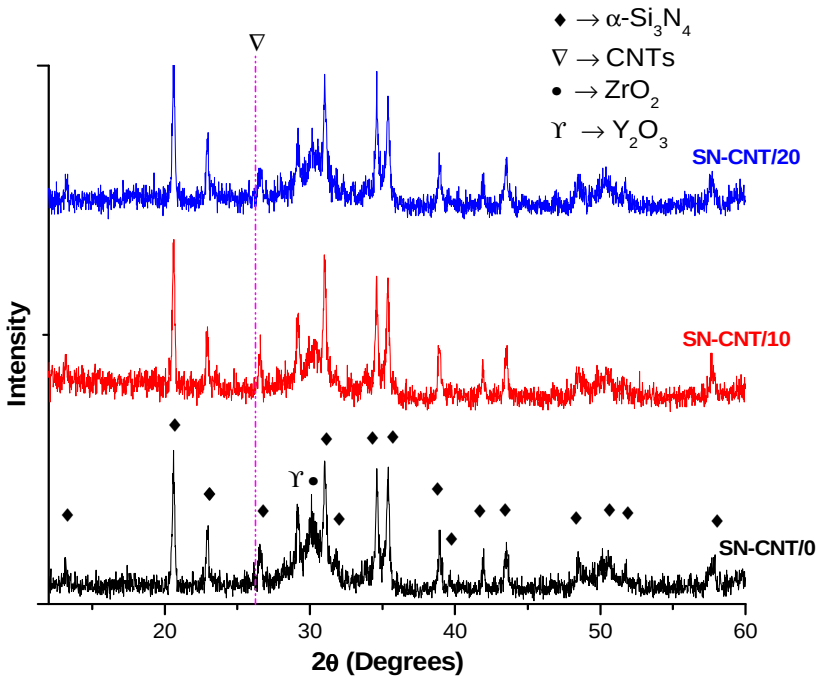

Figure 5.1 - X-ray diffractogram of starting powders after milling process.

5.2.2. Microstructural analysis of starting powders

Although XRD did not detect the presence of MWCNTs in the starting powder, while SEM image evidenced the incorporation of MWCNTs in the starting powders (Figure 5.2). SEM images showed no significant damage of MWCNTs, and the length of MWCNTs fibers is up to 8 to 10 µm, and the diameter is 10 to 30 nm (Figure 5.2). The particle size of silicon nitride was reduced from 50 ÷ 500 nm to 30 ÷ 300 nm after milling. The agglomerations of powders' small particles might be a mixture of sintering additives and zirconia (Figure 5.2). The agglomeration, clustering of MWCNTs, and network of MWCNTs around α - Si_3N_4 grains were also observed in some areas of starting powders (Figure 5.2).

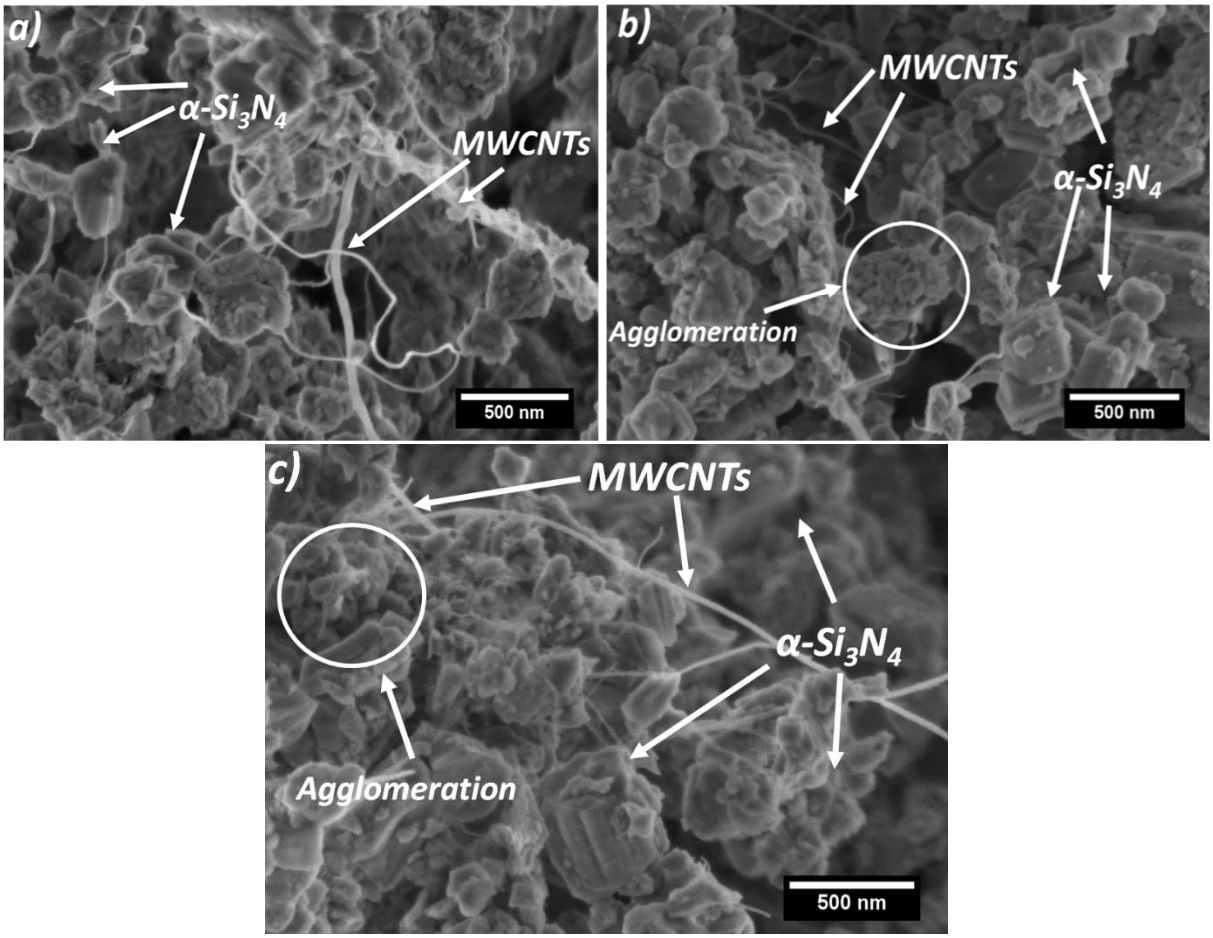

Figure 5.2 – SEM images of starting powders after milling process, MWCNTs presence are evident in all powders: a) SN-CNT/0; b) SN-CNT/10; c) SN-CNT/20.

5.3. Investigation of sintered samples

5.3.1. Structural investigation

Figure 5.3 presents the XRD analysis of sintered samples. XRD diffractogram revealed the complete α to β transformation of Si_3N_4 after sintering at 1700 ˚C for 3 hours holding time in the nitrogen environment (Figure 5.3). Two main phases, β- Si_3N_4 (JCPDS PDF-00-33-1160) and Y-ZrO_2 (JCPDS PDF-00-83-0944), were identified by XRD diffractogram of all sintered composites (Figure 5.3). Other phases, including carbon, was not detected by XRD due to their lower amount than the detection limit. SEM technique was again helpful; the SEM of fractured surfaces revealed the presence of MWCNTs (Figure 5.7). Surprisingly, Si_2N_2O was not found in any of the sintered samples. Si_2N_2O was supposed to be formed during sintering because of the presence of SiO_2 content in starting powders. Previously, Si_2N_2O was formed

by the oxidization of starting powders, and its effects on the mechanical properties were observed. The reason for disappearing of Si_2N_2O might be the reaction occurred between the SiO_2 and carbon nanotubes. According to Equation 2.2, CO/CO_2 might be at a higher temperature during sintering, which reduced the amount of carbon in the sintered samples. The release of carbon by the oxidation in the composite has been reported by other researchers, too [134] [108].

The SiO_2 was more likely consumed in the partial oxidation of MWCNTs during sintering and did not form Si_2N_2O phase.

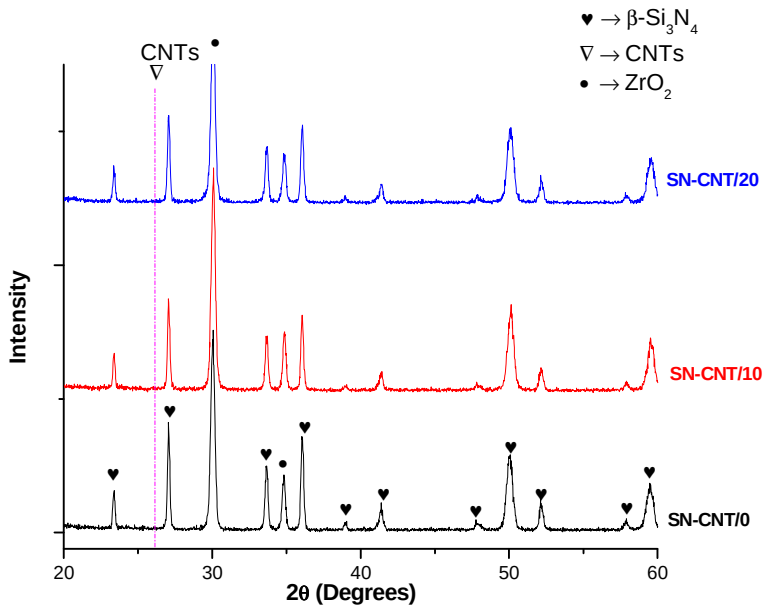

Figure 5.3 - X-ray diffractogram of sintered samples: black diffractogram represents SN-CNT/0, red diffractogram represents SN-CNT/10 and blue diffractogram represents SN-CNT/20.

5.3.2. Apparent Density

The apparent density of sintered samples was measured by the Archimedes method and given in Table 5.2. Apparent density increased slightly with the oxidation time, which attributes to the gases in the form of CO/CO_2 escaped from the bulk during the sintering process.

5.4. Mechanical properties

5.4.1. Vickers hardness

Figure 5.4 illustrates the Vickers hardness of 3 wt% MWCNTs reinforced Si_3N_4 composites. The hardness of the investigated composites increased with increasing oxidation time of the Si_3N_4 powder. The maximum hardness was measured for samples containing 20 hours-

oxidized powders, and the lowest hardness value was measured for the reference sample (SN-CNT/0). The low hardness values compared to the monolithic ceramics prepared using the same oxidized Si_3N_4 powders (~17 GPa) can be explained by a low density and relatively high porosity present in the composites after processing.

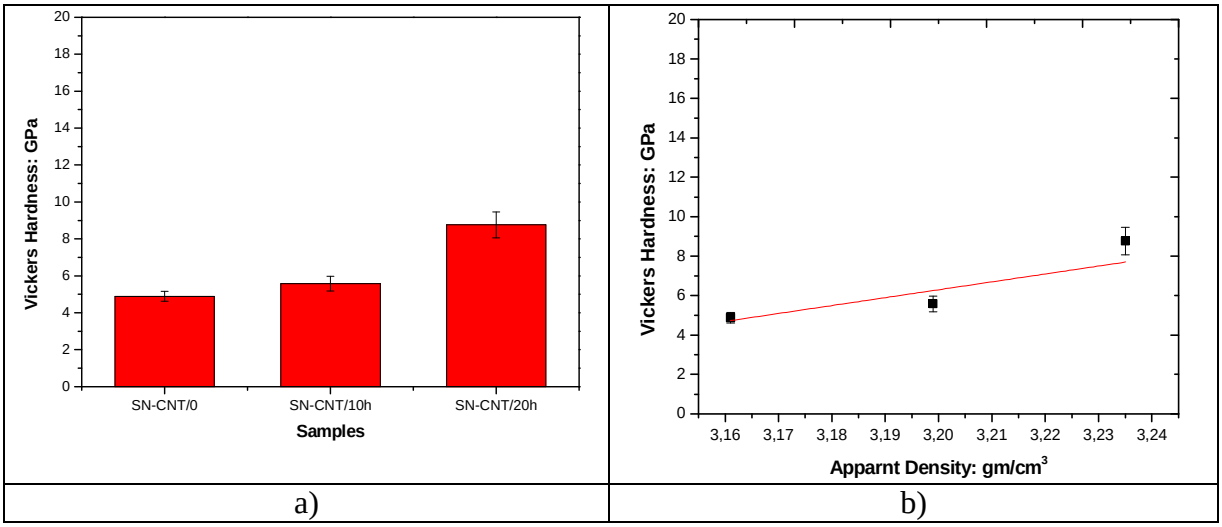

Figure 5.4 – Vickers hardness of sintered composites: a) Vickers hardness increased slightly with the oxidation tine; b) the influence of apparent density on the hardness of the investigated systems.

5.4.2. Flexural Strength

A similar tendency was found for bending strength values. The powders' oxidation time positively influences the density of the investigated systems, which has a positive influence not only on hardness but also on bending strength values.

The 4 – point bending strength of samples SN-CNT/0 (un-oxidized), SN-CNT/10, and SN-CNT/20 were 249.5 MPa, 263.25 MPa, and 296.6 MPa, respectively (Fig 6.5-a). The composite SN-CNT/20h showed almost 2% higher density than that of SN-CNT/0, which resulted in 16% higher flexural strength (Figure 5.5 – c).

A similar tendency was found in the 3 – point bending strength of samples SN-CNT/0 (un-oxidized), SN-CNT/10, and SN-CNT/20 was 313.25 MPa, 332.0 MPa, and 360.4 MPa, respectively (Figure 5.5 - b). Relatively low bending strength was caused by the present porosity and agglomeration/clusters of MWCNTs in the composites and the MWCNTs located between β-Si_3N_4 grains and weakened the bonding between the grains. A higher strength value in the case of 3 – point bending mode can be explained by a lower effective volume in 3 – point bending mode compared to the 4 – point mode and with a lower

probability of presence strength decreasing-defects close to the tensile surface of the samples. Balazsi et al. [135] reported a similar relation between density and flexural strength. They reported that flexural strength of investigated composites increased with the increase of density.

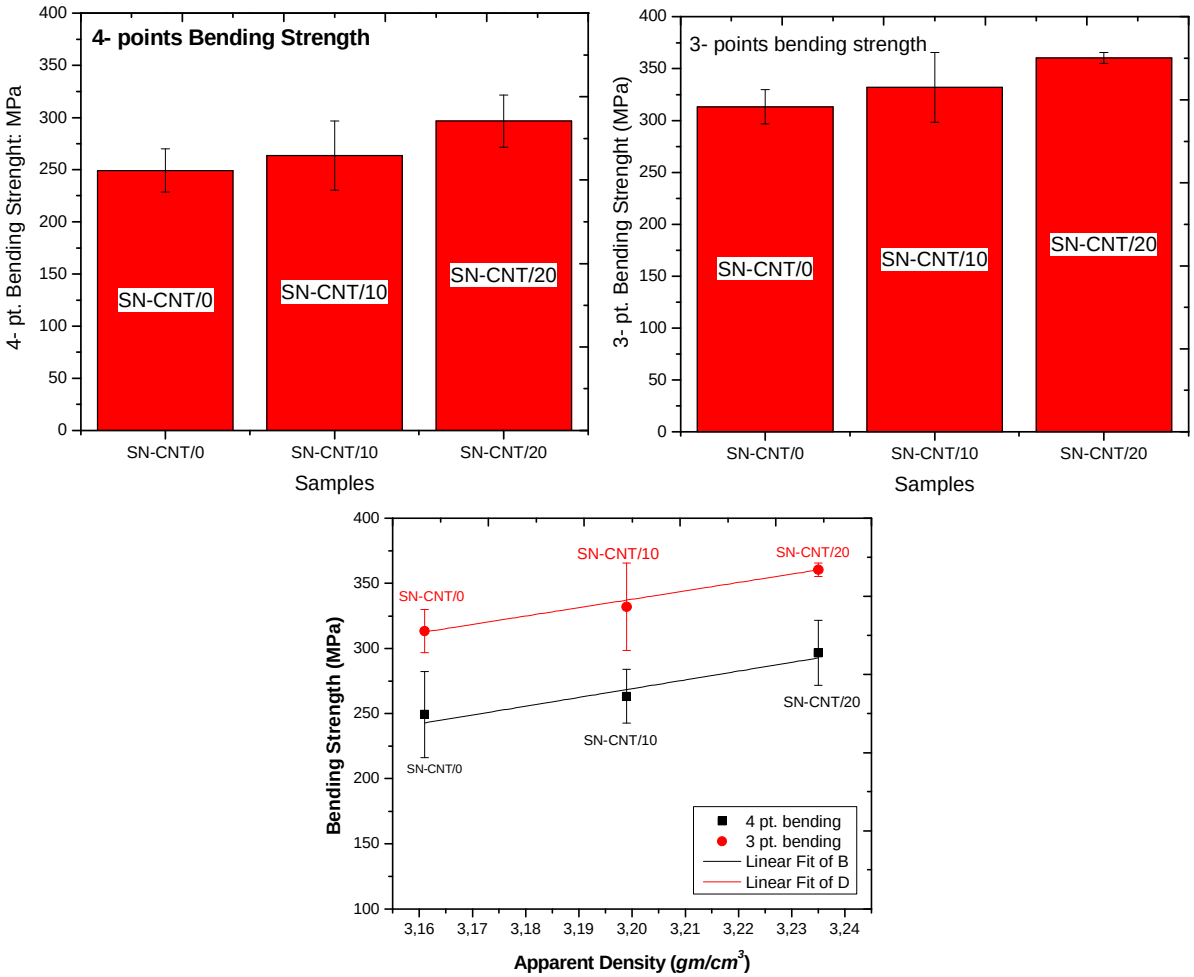

Figure 5.5 – Flexural strength of sintered samples: a) 4 – point bending strength; b) 3 – point bending strength and c) 4 – and 3 – point bending strength with respect to apparent density of sintered samples.

5.4.3. Young's Modulus

The values of Young's modulus of sintered samples also showed a relationship with the apparent density of sintered samples. Young's modulus of sintered samples increased with the increasing value of samples' densities (Figure 5.6).

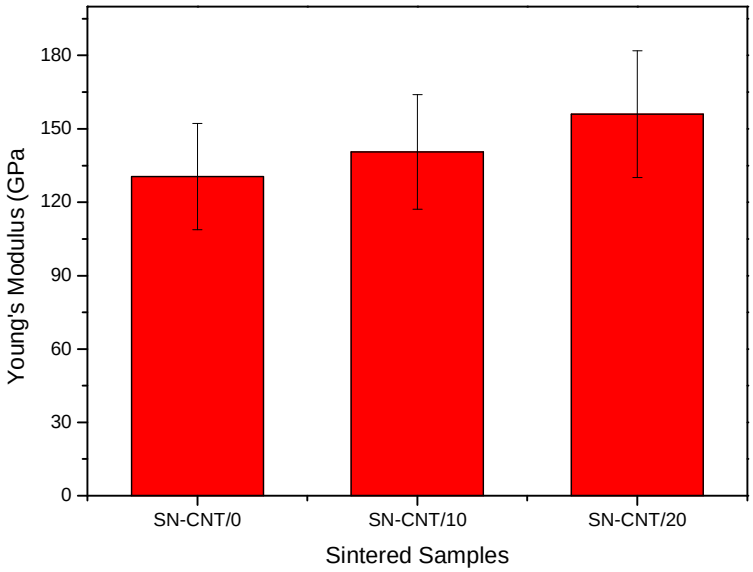

Figure 5.6 – Young's modulus of investigated system increased with the oxidation time.

5.4.4. Fractographic analysis of fractured surfaces

Fractographic analyses have been performed on the specimens' fracture surfaces after the bending strength test (Figure 5.7). Micro-fractography revealed no such areas as fracture origin, mist, mirror, and hackle are present in any of the fractured surfaces. Usually, in high strength structural ceramics, such characteristics regions (mist, mirror, and hackle) appeared around the fracture origin [136]. Due to such areas, this is easy to identify the fracture origin. It would be worth to mention what are these characteristic regions. A flat area immediately surrounding the fracture origin is called a mirror. An outer region of the mirror looks like a halo is called a mist. A region with ridges outside the mist region is called a hackle. One of the reasons behind such areas' appearance is the release of strain energy during crack propagation [136].

Micro-fractography shows no significant differences in the microstructure and fracture of investigated composites. These composites' microstructure consists of $\beta - Si_3N_4$ grains with an average grain diameter of approximately 0.35 μm and with an average length of 1.1 μm similar to the grain dimension for the systems prepared without CNTs addition. The composites contain pores with size approximately 1 to 10 μm often filled with bundles of CNTs. The composite with more prolonged oxidation of starting powders has less porosity. The fracture's characteristic is mixed inter and intragranular, pulled out of CNTs bundles with length up to 20 μm.

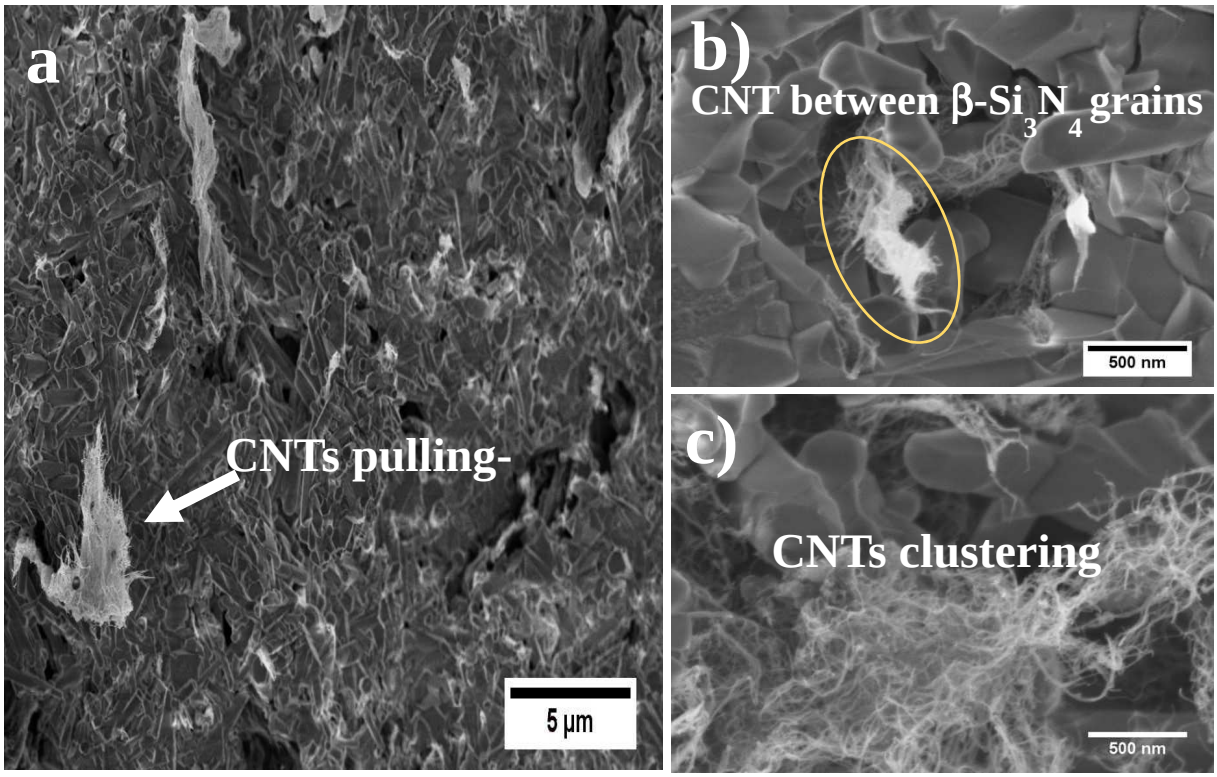

Figure 5.7 – Fracture's characteristics of investigated composites: a) SN-CNT/0; b) SN-CNT/10h and c) SN-CNT/20h.

5.5. Tribological properties

5.5.1. Coefficient of friction (COF)

The wear test revealed that in all cases was friction after a short initial stage (in order of meters) rather stable and reproducible. There are no significant differences in the investigated composites' friction coefficients over the test running distance and show values between 0.6 and 0.7 during the sliding distance (Figure 5.8). The COF is in the *run-in* stage and *steady-state* stage, almost relatively similar. This result is in very good agreement with the work by Hvizdos et al. [66]. They found a similar or even higher coefficient of friction for Si_3N_4/MWCNTs composites, and the COF started to decrease only when the MWCNT content reached 5 wt% [66].

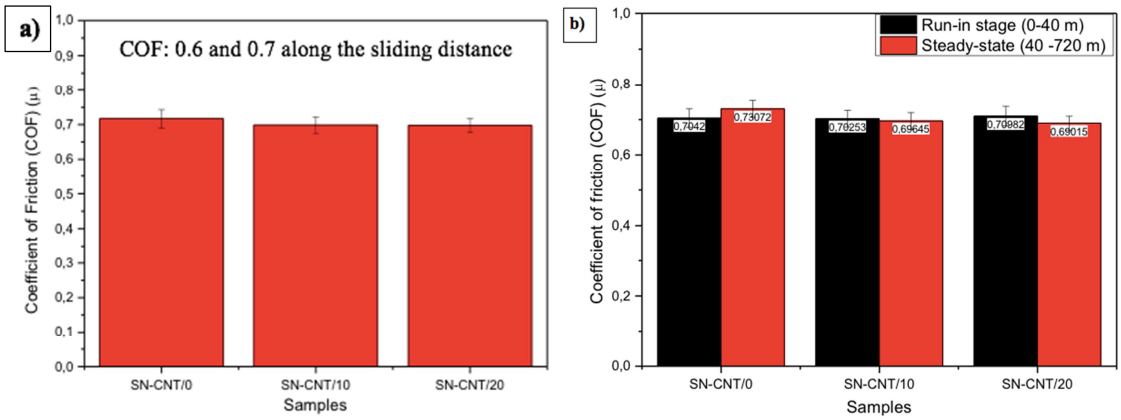

Figure 5.8 - Coefficient of friction of investigated systems: a) Overall average COF along the sliding distance, and b) Average COF in run-in stage and steady state stage.

5.5.2. Wear Rate

Figure 5.9 shows the wear rate of all the systems. The wear rate decreased with the oxidation time, and this improvement is attributed to the increase of apparent density. Due to the different technicality of tribo-machine, Wear rate during the *run-in*, and *steady-state* could not be calculated. Still, the overall wear rate is lower than that of monolithic systems. Similarly, as in the case of hardness and bending strength, the increased density had a positive influence on the wear resistance of the investigated composites, and with increasing density, the wear volume was decreasing.

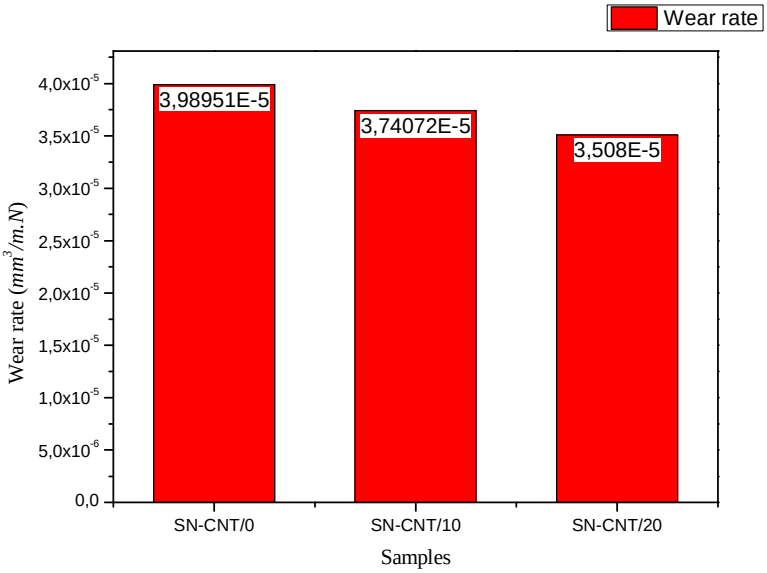

Figure 5.9 - Wear rate of investigated systems.

6. Si_3N_4 + 1 wt% graphene composites

After discussing the monolithic and MWCNTs reinforced silicon nitride systems in chapters 4 and 5, this chapter will comprise the graphene reinforced silicon nitride systems.

6.1. Preparation of Si_3N_4 + 1 wt% graphene composites

The starting powder 90 wt% α - Si_3N_4 (Ube, SN-ESP), and sintering aids 4 wt% Al_2O_3 (Alcoa, A16) and 6 wt% Y_2O_3 (H.C. Starck, grade C), polyethyleneglycol (PEG) surfactants, and ethanol were added to the powder mixture. These mixtures were milled in a highly efficient attritor mill (Union Process, type 01-HD/HDDM) equipped with zirconia agitator delta discs (volume of 1400 cm^3) and zirconia grinding media (diameter of 1 mm) in a 750 ml tank. Each batch contained ZrO_2 as contamination, which originated from the grinding media. The milling process was performed with a high rotation speed of 3000 rpm until 4.5 h.

Three types of commercially available graphene nanoplatelets were added as reinforcements (Figure 6.1):

1. exfoliated graphene nanoplatelets (xGnP-M-5) [137]
2. exfoliated graphene nanoplatelets (xGnP-M-25) [137]
3. nano graphene platelets (Angstron N006-010-P) [138]

1 wt% of each graphene's type was added to α-Si_3N_4 powders and milled with low rotational speed, 600 rpm until 30 min. The milling with low rpm and shorter time was performed to avoid damaging the graphene reinforcements particles.

The substance was dried and sieved with a filter with a mesh size of 150 mm. Green samples (green bodies) were obtained by dry pressing at 220 MPa. Before sintering processing, the green bodies were heat treated at 400 °C for 4 hours.

Two different sintering processes were performed to densify the powder compacts to observe the effect of the sintering process on the prepared composites' mechanical and tribological properties. The sintering processes are given below:

1. Hot isostatic pressing (HIP): Hot isostatic pressing (HIP) was performed at 1700 °C in high purity nitrogen by a two-step sinter-HIP method using BN embedding powder at

20 MPa, with 3 h holding time. The heating rate did not exceed 25 °C/ min. The dimensions of the as-sintered specimens were 3.5mm x 5mm x 50mm.

2. Gas pressure sintering (GPS): Gas pressure sintering (GPS) was performed at 1700 °C in high purity nitrogen using BN embedding powder at 2 MPa, with no holding time. The heating rate did not exceed 25 °C/min. The dimensions of the as-sintered specimens were 3.5 mm × 5 mm × 50 mm.

Detailed information about the prepared composites are given in Table 6.1.

Table 6.1 - Details of materials and parameters of preparation

No.	Starting Powders (wt%)			Carbon (wt%)	Type of additives	Sintering Conditions			Sintering Technique
	Si_3N_4	Al_2O_3	Y_2O_3			T (°C)	Holding time	Pressure (MPa)	
SN-1	90	4	6	0	-	1700	-	2	GPS
SN-2	90	4	6	1	xGnP-M-25	1700	-	2	GPS
SN-3	90	4	6	1	Angstron N006-010-P	1700	-	2	GPS
SN-4	90	4	6	1	xGnP-M-25	1700	3 h	20	HIP
SN-5	90	4	6	1	xGnP-M-5	1700	3 h	20	HIP

6.2. Investigation of starting powders

6.2.1. Microstructural analysis

Figure 6.1 presents the morphology of graphene added in the Si_3N_4 matrix [139]. According to the technical data sheet provided by the supplier, the particles have an average thickness of approximately 6 to 8 nanometers and a typical surface area of 120 to 150 m^2/g. These commercial graphene platelets are exfoliated. Exfoliation is vital for graphene, as its precursors have layered structures held together through ionic and van der Waals forces [140]. Exfoliation involves the separation of platelets from one another, and it enhances the degree of dispersion and integration in the matrix.

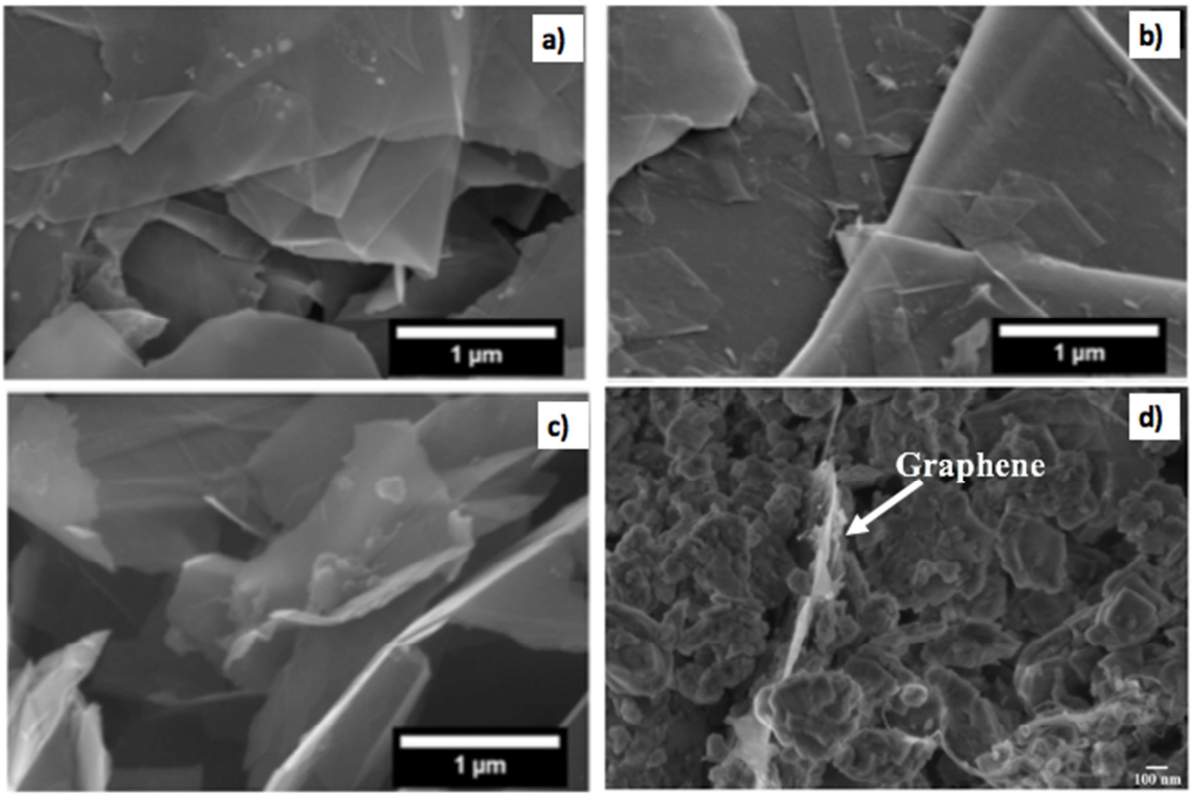

Figure 6.1 – SEM images of reinforcements: a) exfoliated graphene nanoplatelets (xGnP-M-5) with 5 µm particle size; b) exfoliated graphene nanoplatelets (xGnP-M-25 with 25 µm particle size); c) nano graphene platelets (Angstron N006-010-P) [139]*; d) graphene platelets in starting powders.*

6.3. Investigation of sintered samples

6.3.1. Apparent density

The apparent densities of sintered samples were measured by the Archimedes method. The hot isostatic pressed (HIP) samples showed a slightly higher density than samples sintered by gas pressure sintering (GPS). The HIP is preferred to achieve full density during the sintering process. Table 7.2 shows the values of the density of sintered samples. The 1 wt% graphene added Si_3N_4 composites have higher density, and it shows that 1 wt% of reinforcement is an optimum choice to achieve high density. As many properties depend on density, the positive effect of high density should be realized in mechanical and tribological properties.

Table 6.2 – Apparent density of sintered samples.

Materials	Apparent Density (g/cm^3)
SN-1	3.329
SN-2	3.301
SN-3	3.297
SN-4	3.375
SN-5	3.379

6.4. Mechanical Properties

6.4.1. Micro Vickers Hardness

Figure 6.2 shows the Vickers hardness values of sintered samples. The hardness values of all the samples are relative to each other. The highest values were observed for the SN-1 sample, and the hardness slightly decreased with the addition of 1 wt% graphene nanoplatelets. As compared to MWCNTs added silicon nitride composites, these hardness values are higher. Based on these values, the material can be applied to the engineering sector under the load. Higher addition (above 1 wt%) of graphene may inhibit the densification process and induce more porosity, which results in lower mechanical properties as lower mechanical properties of 3 wt% MCWNTs reinforced silicon nitride composites [141].

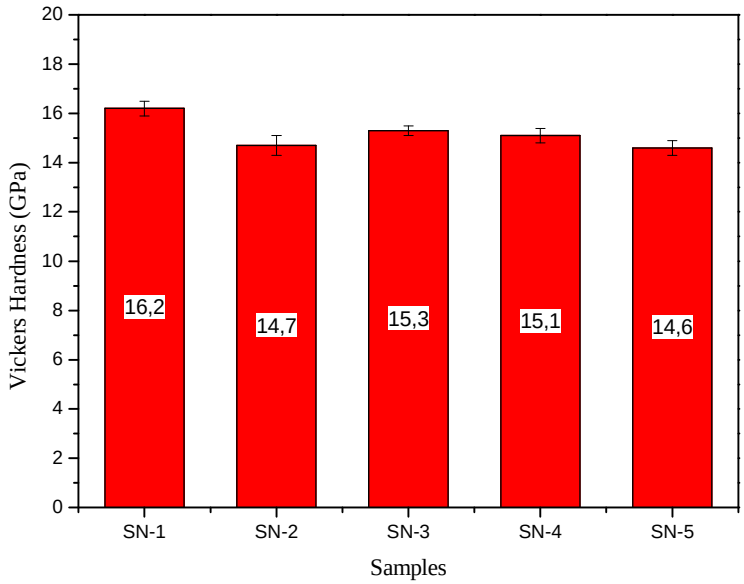

Figure 6.2 – Vickers hardness of investigated systems.

6.4.2. Indentation fracture resistance (K_{IIFR})

The indentation method was used to measure the composites' fracture resistance. This method was used because of the smaller size of specimen size than the required size for a standard fracture toughness test. Figure 6.3 presents the fracture resistance values for the sintered samples. The GPS silicon nitride shows slightly lower fracture resistance in comparison to the silicon nitride prepared by the HIP. The highest value of fracture resistance was recorded for the sample SN-4 reinforced with exfoliated graphene nanoplatelets with 25 μm particle size densified by the HIP. The high value may tribute the uniform dispersion of graphene, larger particle size, high density and good bonding with the silicon nitride matrix grains due to the processing technique. However, this is early to conclude what did parameter contribute to fracture resistance because the SN-2 also contains the same type of graphene but exhibited the lowest fracture resistance.

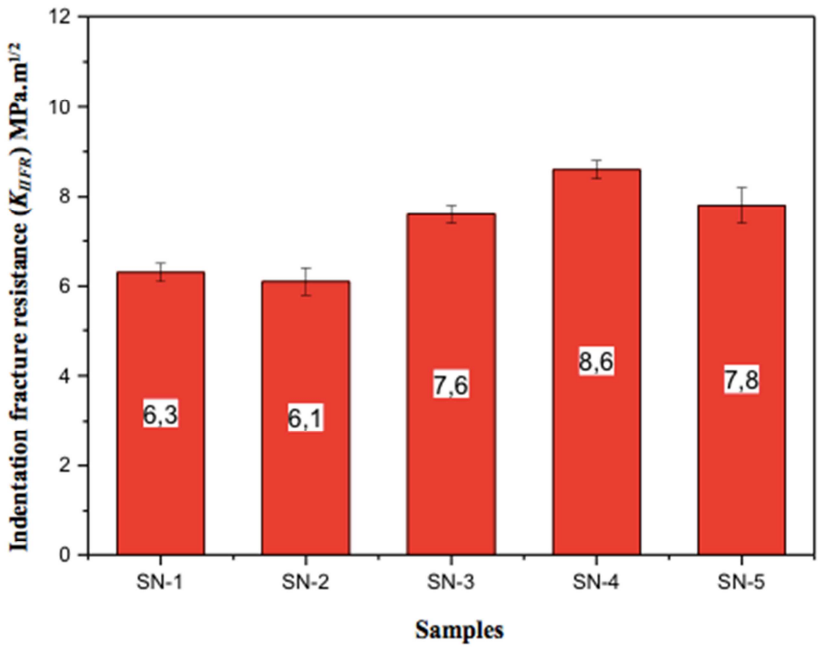

Figure 6.3 – Indentation fracture resistance (K_{IIFR}) of investigated systems.

6.4.3. Fractographic analysis

Analysis of fractured surfaces is essential to identify the nature of cracks and their propagation, microstructure, and bonding between reinforcement particles and matrix. The scanning electron micrographs reveal the fracture surfaces (Figure 6.4) [139]. These micrographs show not only the dispersion but the local contacts between the β - Si_3N_4 grains and graphene platelets. Here, only selected results for samples sintered at HIP are presented.

The white arrows show embedded graphene's location in the matrix β - Si_3N_4 grains in the micrographs. Uniform dispersion of graphene was observed in the composites. 1 wt% of reinforcement is a small amount, and the uniform dispersion is easier, but it is difficult to realize its influence on the properties. Despite uniform dispersion of graphene, the graphene particles induced porosity in the matrix as well. A possible solution to this issue is to separate the nanosheets and prevent agglomeration during the process.

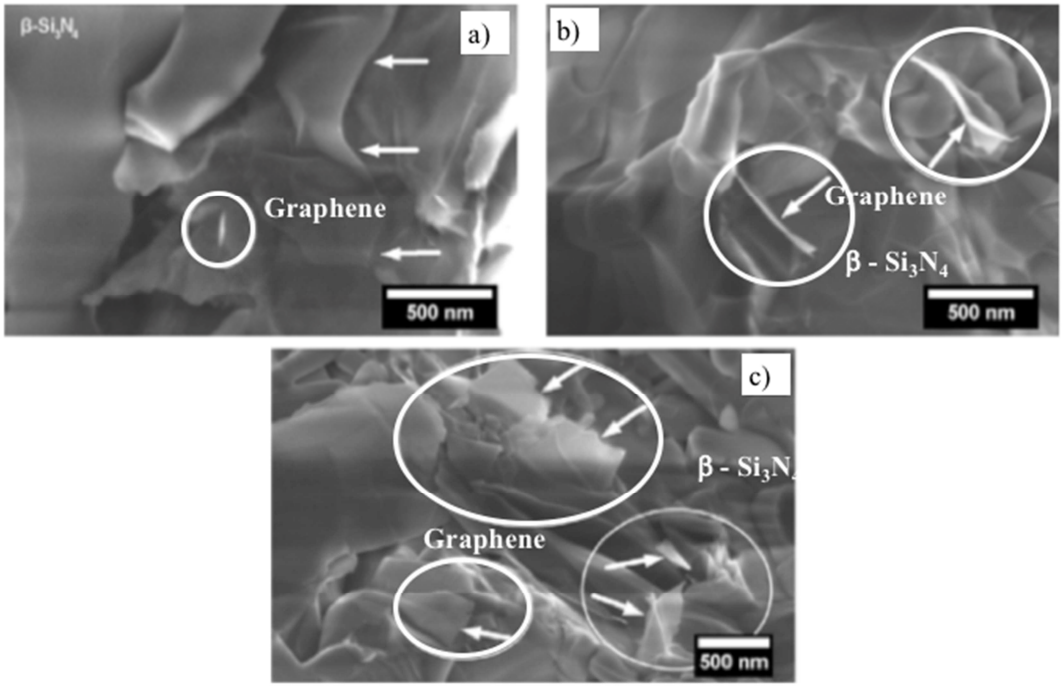

Figure 6.4 – SEM fractured surfaces of sintered materials: a) SN-5 ; b) SN-4 and C) SN-3. [139].

6.5. Tribological Properties

6.5.1. Coefficient of friction (COF)

Figure 6.5 demonstrates the coefficient of friction (COF) under 5 N and 13.5 N loads in the *run-in* stage (0 – 40 m) and *steady-state stage* (40 – 720 m) for the investigated systems. After the *run-in* stage, the coefficient of friction under the testing conditions was stable for all studied systems. The average coefficient of friction in steady – state was between 0.40 to 0.47 under a 5 N load. In the case of an experiment under 13.5 N, average COF was perceived in the range of 0.55 ~ 0.69. Generally, higher COF under higher load and lower COF under lower load might be due to the Hertzian contact pressure. Higher load exerts higher contact pressure which response to high COF.

The lowest coefficient of friction under both loads, 5 N and 13.5 N, was recorded for SN-1 prepared by gas pressure sintering. At the same time, SN-5 responded with the highest COF under both loads, 5 N and 13.5 N.

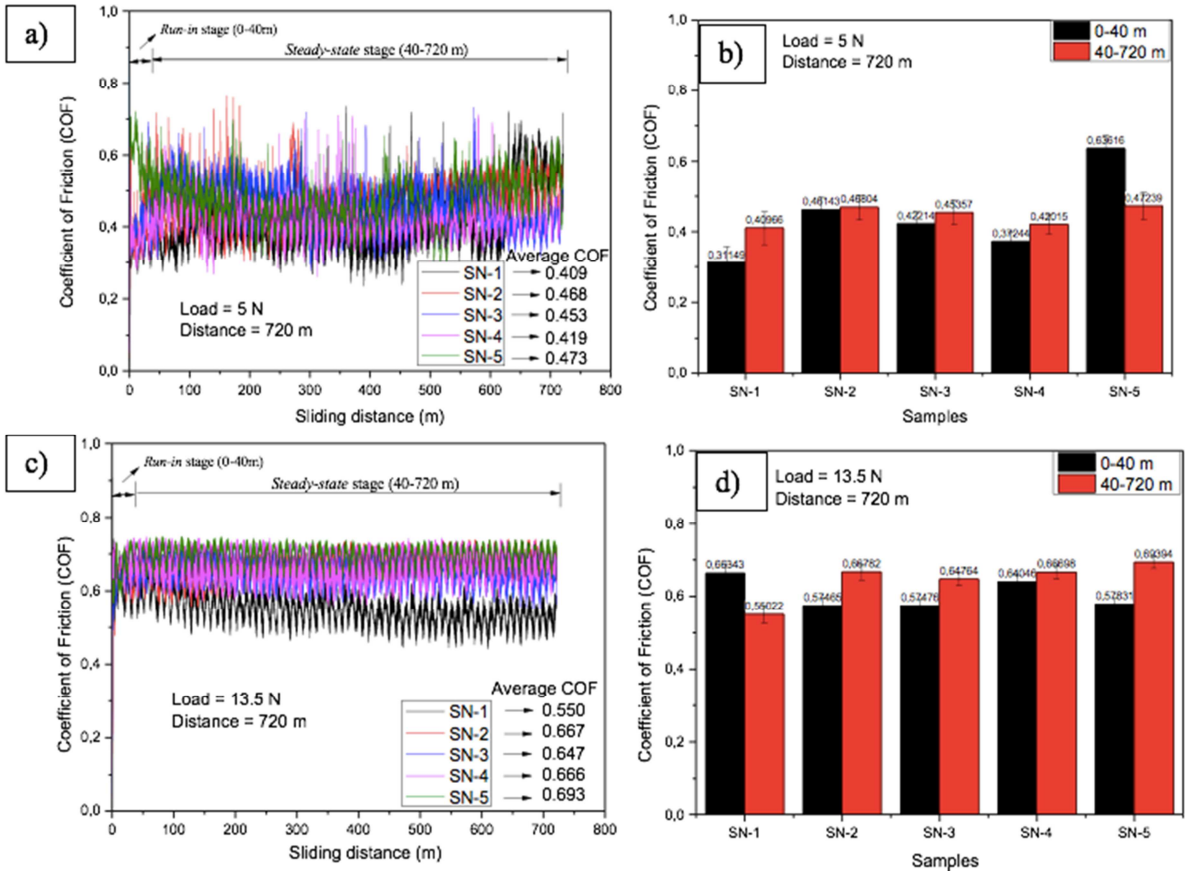

Figure 6.5 – Coefficient of friction of investigated composites: a) COF under 5 N loads; b) COF of composites during (0-40 m) and 40-720 m) under 5 N load; c) COF under 13.5 N loads; d) COF of composites during (0-40 m) and 40-720 m) under 13.5 N load.

6.5.2. Wear rate

Figure 6.6 shows the wear rates under loads of 5 N and 13.5 N for the investigated systems. The investigated systems' wear rates are in the range of 10^{-6} ~ 10^{-7} mm^3/N.m. Overall, the wear rates of systems under 5N loads are lower than that of systems under 13.5 N. The lowest wear rate was observed for SN-1 under both loads 5 N and 13.5 N. The highest wear rate was recorded for SN-4 under the load of 13.5 N. The obtained results do not show a correlation with the microstructure features, reinforcements impact, or processing technique. Further investigation is needed to prove the effect of reinforcements or processing techniques on the composites' wear properties.

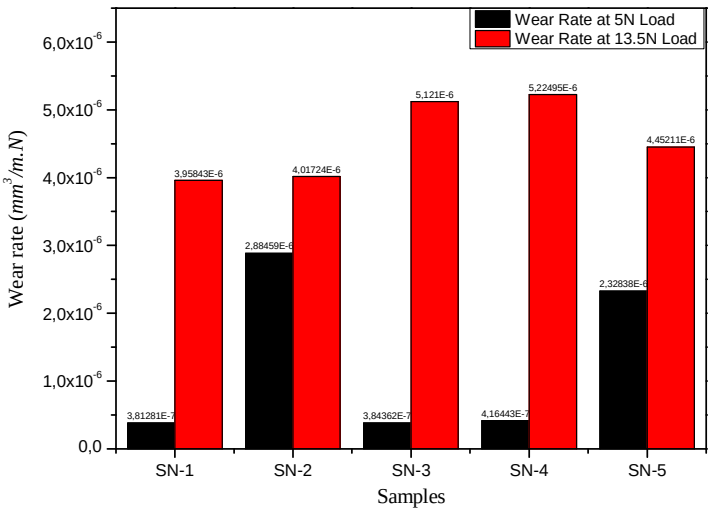

Figure 6.6 – Wear rates of silicon nitride composites with 1 wt% of different types of graphene under 5 N loads and 13.5 N loads.

6.5.3. Wear Mechanism

The investigated composites' wear tracks were analyzed by SEM to identify wear mechanisms. Identical wear mechanisms were identified in all investigated systems, so selected images are presented here (Figure 6.7). The worn surface of the SN-1 was relatively smooth, with only a small amount of abrasion groves and adhered debris. Under the higher load (13.5 N), micro-crack formation and spalling layers were also observed. Based on SEM-EDX results, the white spots correspond to ZrO_2 containing phase, and the ZrO_2 was originated from milling media.

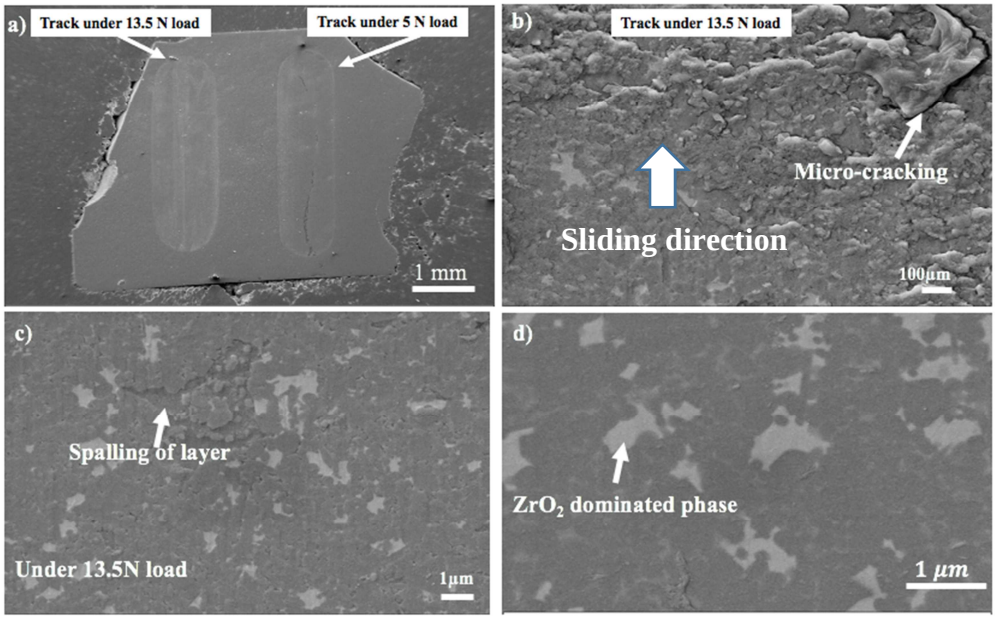

Figure 6.7 – Wear mechanisms identified by SEM: a) wear tracks for SN-1 under 5 N and 13.5 N; b) wear track under 13.5 N with higher magnification, microcracking; c) wear track under 5 N load with higher magnification; d) wear track of SN-4 under 5 N load.

Figure 6.8 reveals the inside of wear track of sample SN-5 under 5 N load prepared by the HIP with the reinforcement of 1 wt% exfoliated graphene nanoplatelets with a particle size of 5 μm. SEM image of the wear track reveals it seems to contain more plastic deformation in the wear tracks. It was also observed that tribo-film was formed and broken. It can be seen the worn-out particle's composition shows the formation of tribo-film and its removal when the frictional forces surpassed the threshold value (Figure 6.8). The SEM image also revealed that graphene platelets integrated well and bonded strongly with the Si_3N_4 grains.

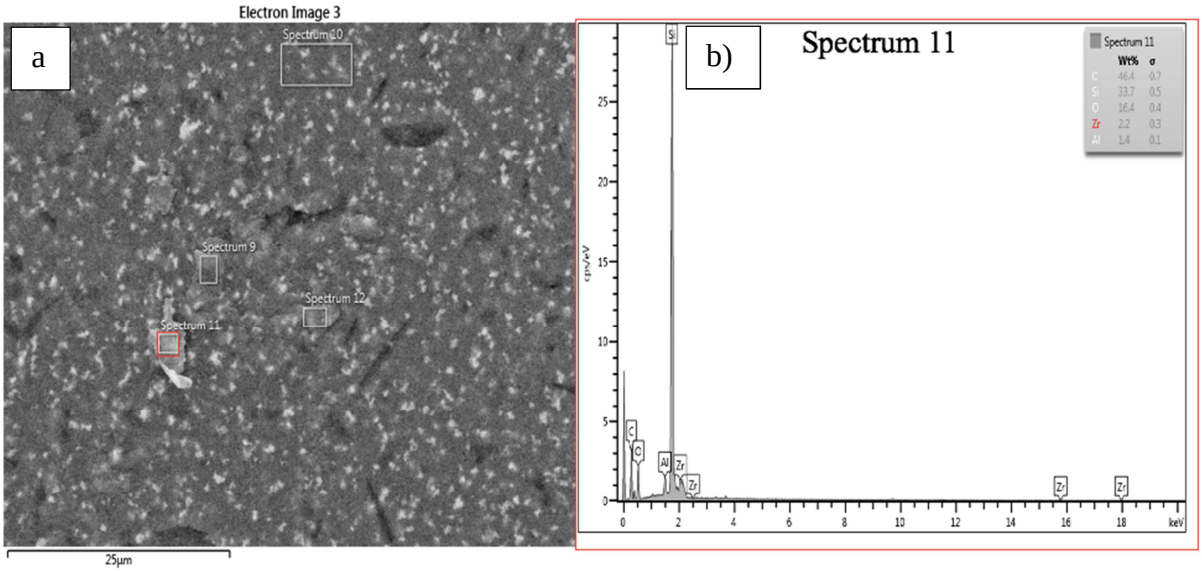

Figure 6.8 – Wear mechanisms in sample SN-5 under 5 N load identified by SEM: a) a worn film on the surface; and b) elemental composition of worn film.

7. Conclusion

Novel findings are summarized as follows:

1. **I demonstrated that in-situ Si_2N_2O could be produced in the Si_3N_4 matrix by oxidizing the starting powders at 1000 ˚C, adding oxides (4 wt % Al_2O_3, 6 wt% Y_2O_3) as sintering aids, and densifying the powders compacts by hot isostatic pressing (HIP) at 1500 or 1700 ˚C in an N_2 gas environment under 20 MPa pressure for 3 hours.**

It was demonstrated successfully that the production of in-situ Si_2N_2O is feasible by oxidizing the starting powders. For the first time, the in-situ Si_2N_2O was produced by adopting the techniques described earlier in the Chapter 4. The starting powders α - Si_3N_4 were oxidized at 1000 °C in an ambient environment for 10 and 20 hours. As a result of oxidation, a nanolayer of amorphous SiO_2 was formed on α - Si_3N_4 particles, according to the **Equation 4.1**.
The formation of the SiO_2 layer was confirmed by HRTEM results **(Figure 4.7)** and EDX analysis **(Figures 4.5 and 4.6)**.
During the sintering process, the Si_2N_2O was nucleated due to a reaction between Si_3N_4 and SiO_2 **(Equation 4.2)**.
The presence of the Si_2N_2O phase was confirmed by XRD analysis **(Figure 4.9)**. The mechanism of the in-situ growth of Si_2N_2O has been described in **Figure 4.10**. The amount of Si_2N_2O increased with an increasing amount of oxygen content in starting powders, which is a function of oxidation time **(Figure 4.11 – b).**

2. **I demonstrated that the Si_2N_2O phase could be preserved above 1500 °C by applying a high pressure of N_2 (20 MPa) gas during sintering and a suitable selection of sintering aids (Al_2O_3 and Y_2O_3).**

It has been proved here that the formation of Si_2N_2O started at a lower temperature than the α to β- transformation temperature, and the higher concentration of oxygen in starting powders favored the formation of Si_2N_2O and hindered the crystallite growth of β- Si_3N_4 **(Figure 4.12 – b).** Contrary to other researchers' findings, Si_2N_2O was found stable above 1500 °C in the current work. A few researchers reported the decomposition of Si_2N_2O phase above 1500 °C

(according to Equations 4.3 and 4.4) due to the addition of sintering aids of Li_2O above their threshold amount.

The Si_2N_2O phase above 1500 °C can be preserved by adopting a high pressure of N_2 (20 MPa) gas during sintering and a suitable selection of sintering aids (Al_2O_3 and Y_2O_3). XRD spectra of sintered composites confirms the presence of Si_2N_2O phase **(Figure 4.9)**.

3. **I demonstrated that α - Si_3N_4 can be fully transformed to β - Si_3N_4 phase during hot isostatic pressing at 1700 °C under a pressure of 20 MPa of N_2 gas.**

The complete transformation of phase α-Si_3N_4 to phase β-Si_3N_4 is possible by optimum conditions hot isostatic pressing (HIP) at 1700 °C for 3 hours holding time under a pressure of 20 MPa of N_2 gas. β-Si_3N_4 is tougher than that of α-Si_3N_4 because of its elongated hexagonal structure and β phase acts a self-reinforcing agent in the matrix and its presence induced the toughening effect and enhanced the fracture toughness. The amount of β phase is crucial to improve the fracture toughness. The β phase was decreased, and the indentation fracture resistance (K_{IIFR}) was also decreased in the samples produced by HIP at 1700 °C **(Figure 4.17).** The highest indentation fracture resistance (K_{IIFR}) values were achieved in the sample, which contained the highest amount of β phase. Here, it was proven that sintering temperature 1500 °C is lower for the complete phase transformation and mixed α and β phases were achieved **(Figure 4.9 – b)**. By optimizing the sintering temperature, the mixed phases α and β can be achieved in the composite, and the desired ration of α/β can be achieved by optimizing the sintering temperature, holding time, and gas pressure.

4. **Monolithic Si_3N_4 – processed from oxidized and un-oxidized α-Si_3N_4 powders sintered at 1500 °C and 1700 °C by HIP under a pressure of 20 MPa of N_2 gas – exhibited higher values of Vickers hardness, flexural strength and Young's modulus as compared to MWCNTs reinforced silicon nitride composites processed from oxidized and un-oxidized α-Si_3N_4 powders sintered at 1700 °C by HIP under a pressure of 20 MPa of N_2 gas. The addition of carbon nanotubes was detrimental to the mechanical properties of silicon nitride.**

Comparatively, higher mechanical properties (Vickers hardness, flexural strength, Young's modulus) were achieved in the case of monolithic silicon nitride systems, and the mechanical

properties were decreased with the addition of 3 wt% multi-walled carbon nanotubes (MWCNTs).

Figure 7.1 shows that all monolithic silicon nitride systems densified by HIP either at 1500 or 1700 °C exhibited higher Vickers hardness under 10 N applied load than the silicon nitride with 3 wt% MWCNTs prepared by HIP at 1700 °C.

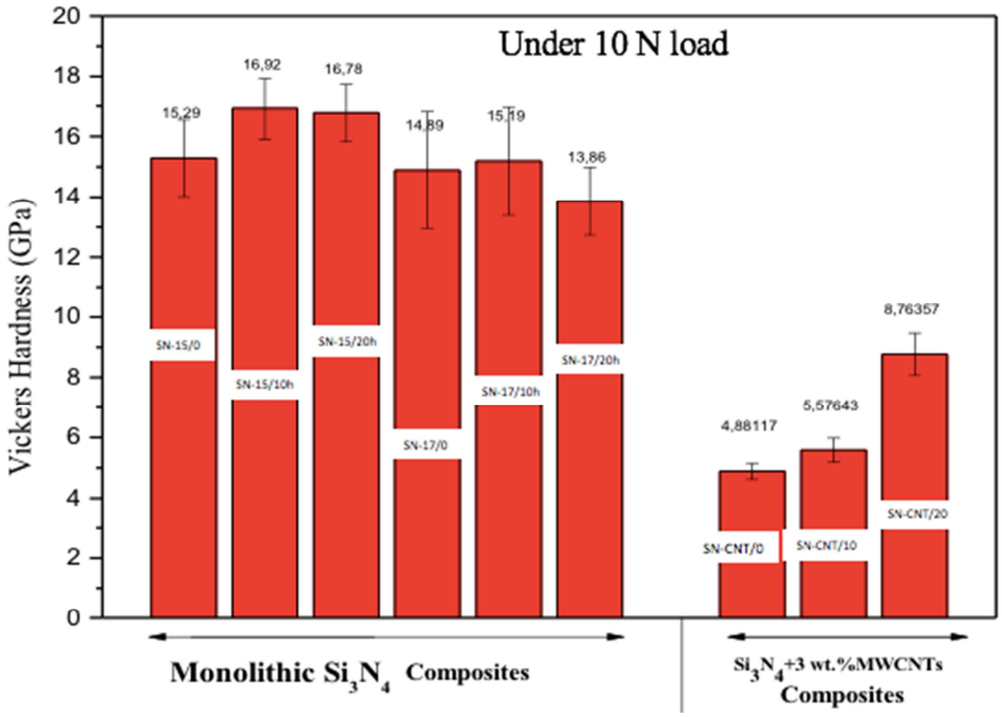

Figure 7.1 – Vickers hardness of monolithic and MWCNTs reinforced silicon nitride composites.

Monolithic Si_3N_4 systems showed higher Flexural strength (based on 4 – point bending strength) than that of 3 wt% MWCNTs reinforced silicon nitride composites **(Figure 7.2)**.

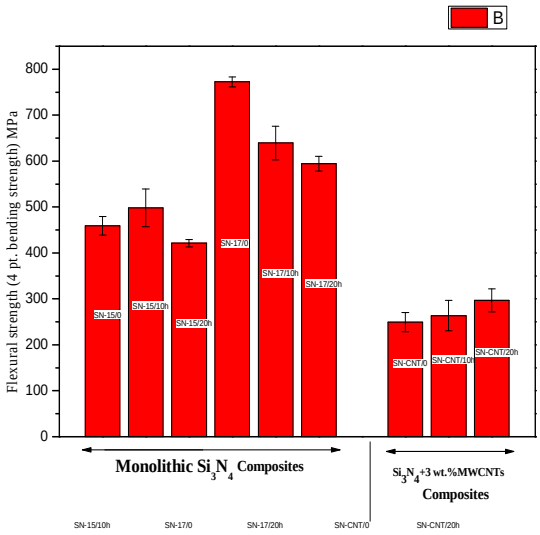

Figure 7.2 – Flexural strength of monolithic systems and 3 wt % MWCNTs added silicon nitride systems.

Monolithic silicon nitride systems exhibited the higher Young's modulus than that of 3 wt% MWCNTs reinforced silicon nitride composites, respectively **(Figure 7.3).**

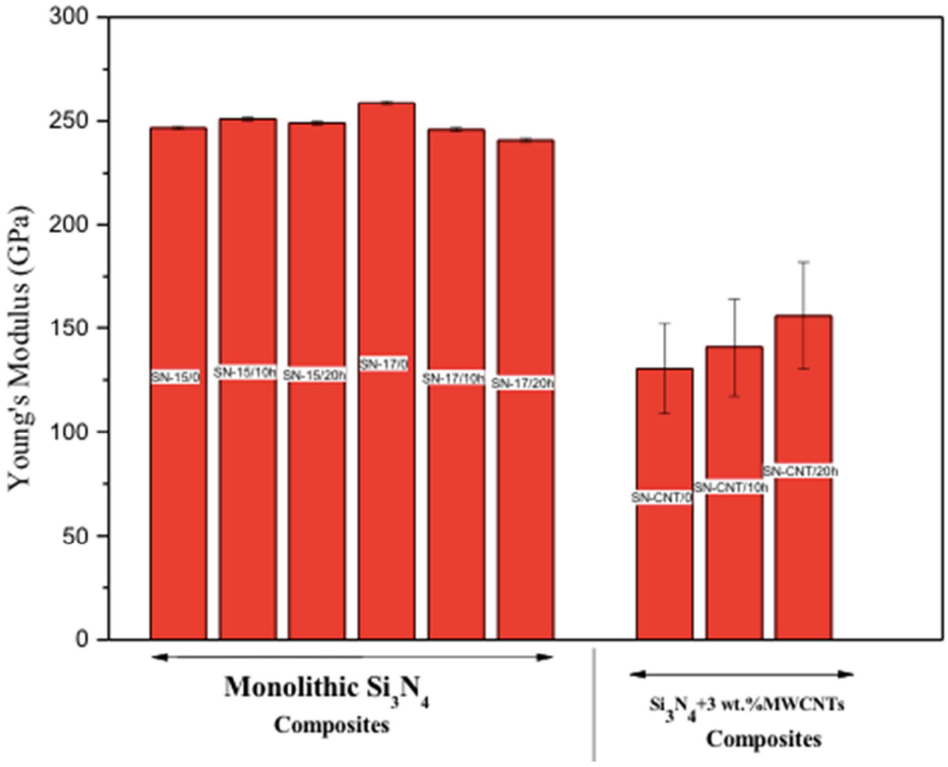

Figure 7.3 – Young's modulus of composites: monolithic Si_3N_4 and Si_3N_4 + 3 wt% MWCNTs.

5. **I reported the detailed study of wear characteristics of monolithic Si_3N_4 ceramics containing in-situ grown Si_2N_2O processed from oxidized α - Si_3N_4 powders for the first time. Monolithic Si_3N_4 with in-situ grown Si_2N_2O prepared by HIP at 1500 °C under 20 MPa pressure of N_2 for 3 hours have lower wear rates in dry conditions that that of monolithic Si_3N_4 with in-situ grown Si_2N_2O prepared by HIP at 1700 °C under 20 MPa pressure of N_2 for 3 hours.**

Best to author's knowledge, the tribological behavior of silicon nitride systems containing in-situ grown Si_2N_2O is not reported yet in the literature. Following main findings have been reported:

1. The wear rates of the systems sintered at 1500 °C were lower in comparison to the wear rates for the systems sintered at 1700 °C.
2. The lowest wear rate, 1.224 x 10^{-4} $mm^3/N•m$, was measured for the system with 10 hours oxidized α -Si_3N_4 powder sintered at 1500 ºC.
3. The wear rates decreased exponentially after the running-in stage for all investigated systems.
4. The main wear mechanisms were identified in the form of abrasive wear with grain pull-out, micro-cracking, and debris formation together with tribo-film formation.

The study of these composites' tribological behavior is in **section 4.5** and **figures 4.19, 4.20, 4.21, 4.22, 4.23**.

6. **Based on results, 1 wt % graphene nanoplates (GnPs) are more promising candidates than 3 wt% MWCNTs as reinforcements in the silicon nitride matrix for robust tribological properties tested by identical parameters.**

Based on available tribological results for MWCNT and graphene reinforced Si_3N_4 systems, the 1 wt% graphene reinforced Si_3N_4 composites showed lower wear rates under identical testing parameters **(Figure 7.4)**. Tribological properties for both systems were tested under the same parameters as follows:

- Test configuration = Ball-on-Plate.
- Tribometer = UMT 3 (Bruker),
- Counter body = Si_3N_4 ball (D=6.35 mm),

- Sliding Conditions = dry,
- Load = 13.5 N & 5 N,
- Sliding speed = 0.1 m/s,
- Total sliding Distance = 720 m,
- Average Hertzian pressure ~ 2 GPa.

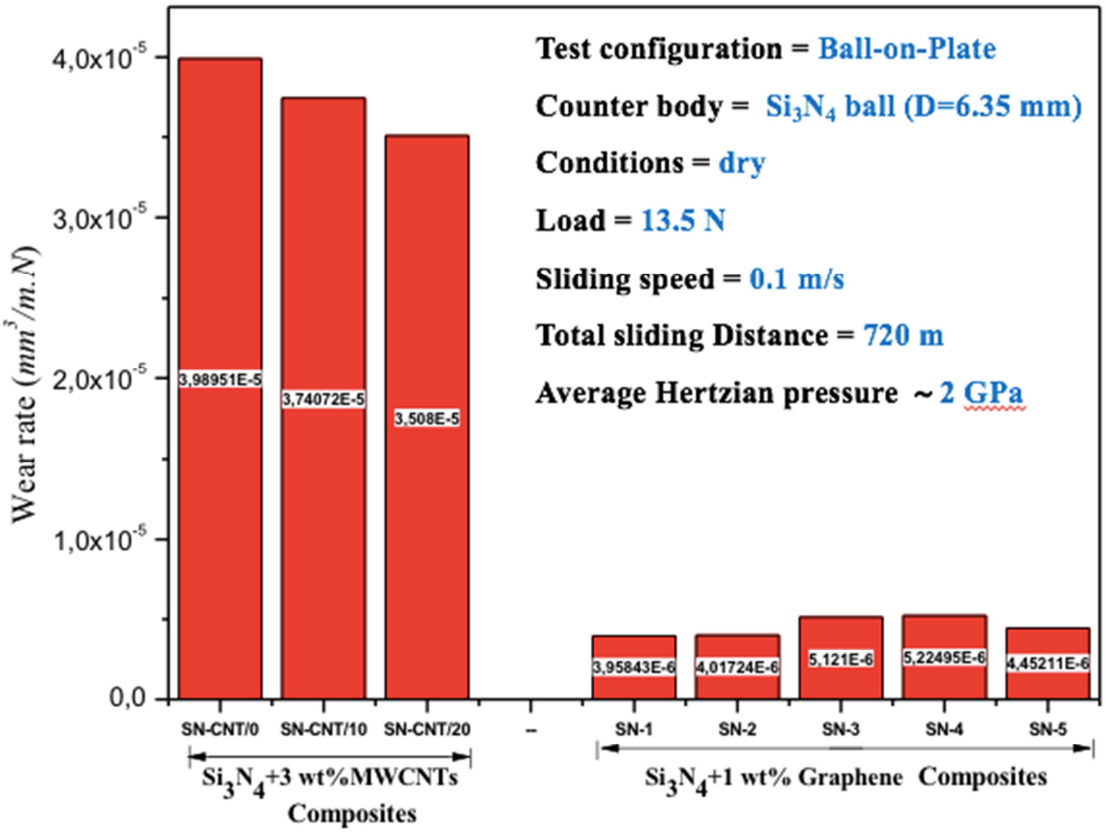

Figure 7.4- Wear rates of investigated systems.

7.1. Further challenges

Further progress is expected in the development of monolithic and carbon nanofillers reinforced Si_3N_4 composites with the aim:

- Further investigative study is needed for graphene reinforced silicon nitride systems in order to define the wear mechanisms,
- To achieve an optimized amount of in-situ Si_2N_2O can be possible by optimizing the oxidation of starting powders. The desired amount of Si_2N_2O can be achieved by optimizing the oxidation of starting powders. In other words, the amount of the desired

Si_2N_2O can be achieved by optimizing the amount of oxide phase (SiO_2) in the starting powders,

- To achieve the desired amount of β-Si_3N_4 can be possible by optimizing the sintering parameters such as sintering technique, temperature, pressure, and holding time,
- To solve the problem of difficulties relating to dispersing carbon nanofillers mainly with an increasing concentration of nanofillers by the help of advanced processing such as colloidal processing, etc. This will help not only in the elimination/limitation of strength-decreasing defects in the composites, but also in increasing the number of active nanofillers in the toughening process and an increased number of constituents for increasing the tribological and functional properties as well,
- To realize an effective carbon nanofillers reinforcement strategy while optimizing the nanofillers/matrix interface in such a way as to have the adhesion between the nanotube and the matrix be not so strong as to introduce nanotube failure before debonding, but to have the adhesion be not so weak that the frictional resistance to sliding is minimal,
- To make advances in improving the properties of modified carbon nanofillers and in the field of *in-situ* reinforced composites with the aim to offer processing of Si_3N_4 + CNT/graphene composites with improved functional, tribological and mechanical properties,
- To improve the most promising processing methods such as aqueous colloidal processing, ultrasonication, bead milling, improved SPS, electric field-assisted pressure-less sintering, usually named flash sintering, etc,
- To introduce new characterization and testing methods in the area of Raman spectroscopy, focused ion–beam (FIB) technique, microcantilever technique for fracture toughness testing, etc,
- To design new systems in the form of carbon nanofillers-concentrated, functionally graded and layered carbon–ceramic composites, etc., in combination with other carbon-based fillers as graphene platelets which would surely offer multi-functional properties for challenging functional, bio-medical and structural applications,
- To improve the applications of carbon-ceramic matrix nanocomposites such as: load-bearing structural parts, wear or friction surfaces, medical devices and implants, automotive, aerospace, power generation applications, tool and die materials, and military field applications.

8. Publications

8.1. Publications related to PhD topic

[S-1] **Awais Qadir**, Zsolt Fogarassy, Zsolt E. Horvath, Katalin Balazsi, Csaba Balazsi, Effect of the oxidization of Si3N4 powder on the microstructural and mechanical properties of hot isostatic pressed silicon nitride, ***Ceramics International***, 2018 Aug 15;44(12):14601-9
Impact Factor: 3.830 (Q1)
DOI: https://doi.org/10.1016/j.ceramint.2018.05.081

[S-2] **Awais Qadir**, B. H Rachid, P. Pinke, J. Dusza, Tribology of Si_3N_4 containing in-situ grown Si_2N_2O processed from oxidized α - Si3N4 powders, ***Ceramics International***, 2021 (***In Press***)
Impact Factor: 3.830 (Q1)
DOI: https://doi.org/10.1016/j.ceramint.2021.03.058

[S-3] **Awais Qadir**, Pinke Peter, Jan Dusza, Silicon nitride with the addition of carbon nanotubes: A review of progress, challenges and future prospects, ***Materials*** 2020, 13, 2799.
Impact Factor: 3.057 (Q2)
DOI: https://doi.org/10.3390/ma13122799

[S-4] **Awais Qadir**, Katalin Balazsi, Csaba Balazsi, Michal Ivor, Jan Dusza, Properties of MWCNTs added Si3N4 composites processed from oxidized silicon nitride powders. ***Processing and Application of Ceramics***. 2020;14(1):25-31
Impact Factor: 0.968 (Q3)
DOI: https://doi.org/10.2298/PAC2001025Q

[S-5] **Awais Qadir**, Jan Dusza, Pinke Péter, Tribological Behavior of Silicon Nitride and Carbon Based Filler Composites – a Review, In: Horváth, Richárd; Beke, Éva; Stadler, Róbert Gábor (szerk.) Mérnöki Szimpózium a Bánkin előadásai: Proceedings of the Engineering Symposium at Bánki (ESB 2019), Budapest, Magyarország : Óbudai Egyetem, (2019) pp. 7-16. , 10 p.

[S-6] **Awais Qadir**, Jan Dusza, Pinke Péter, Tribological behavior of graphene reinforced silicon nitride composites, In: Horváth, Richárd; Beke, Éva; Stadler, Róbert Gábor (szerk.) Mérnöki Szimpózium a Bánkin előadásai: Proceedings of the Engineering Symposium at Bánki (ESB 2020), Budapest, Magyarország : Óbudai Egyetem, (2020) pp. 48-53.

[S-7] **Awais Qadir**, Pinke Péter, Jan Dusza, Graphene reinforced silicon nitride composites – A review, 2021 **(In progress)**.

8.2. Other publications

[S-5] Kumar Sunil, **Qadir Awais**, Maury Francis, Bahlawane Naoufal, "Visible thermochromism in vanadium pentaoxide coatings", ACS Appl. Mater. Interfaces, 2017, 9 (25), pp 21447–21456

Impact Factor: 7.145 (Q1)

DOI: https://pubs.acs.org/doi/abs/10.1021/acsami.7b04484

[S-6] Pozdniakov, A. V., A. Lotfy, **A. Qadir**, E. Shalaby, M. G. Khomutov, A. Yu Churyumov, and V. S. Zolotorevskiy. "Development of Al-5Cu/B4C Composites with low Coefficient of Thermal Expansion for Automotive Application." Materials Science and Engineering: A (2017).

Impact Factor: 4.652 (Q1)

DOI: https://doi.org/10.1016/j.msea.2017.01.075

[S-7] Pozdniakov, A. V., A. Lotfy, A. Qadir, and V. S. Zolotorevskiy. "Effect of the B4C content on the structure and thermal expansion coefficient of the Al–5% Cu alloy-based metal-matrix composite material." The Physics of Metals and Metallography 117, no. 8 (2016): 783-788.

Impact Factor: 1.064 (Q2)

DOI: https://link.springer.com/article/10.1134/S0031918X16060107

8.3. PhD work presentation in conferences

[C – 1] **Awais Qadir**, Katalin Balazsi, Csaba Balazsi, Poster Presentation, Development of silicon nitride-based CNT/graphene composite using hot isostatic pressing (HIP) technique

(Poster Presentation), ECerS 2017, 15th Conference & Exhibition of the European Ceramic Society, Budapest, Hungary, July 9-13, 2017. page 98. http://static.akcongress.com/downloads/ecers/ecers2017-programme-book.pdf

[C – 2] **Awais Qadir**, Zsolt Fogarassy, Zsolt E. Horváth, Katalin Balázsi, Csaba Balázsi, Poster: Effect of oxidized Si_3N_4 powder particles on mechanical properties of sintered Si_3N_4 material ***(Poster Presentation)***, International Conference Deformation and Fracture in PM Materials, High Tatras, 2017. Oct. 22-25. http://www.imr.saske.sk/confer/dfpm2017/dfpm2017.html

[C – 3] **Awais Qadir**, Zsolt Fogarassy, Zsolt E. Horváth, Katalin Balázsi, Csaba Balázsi, Poster: Effect of oxidized Si_3N_4 powder particles on mechanical properties of sintered Si_3N_4 material ***(Poster Presentation)***, Joint ICTP-IAEA Workshop on Fundamentals of Vitrification and Vitreous Materials for Nuclear Waste Immobilization, The Abdus Salam Centre for Theoritical Physics (ICTP), Trieste Italy. Nov. 06 -10, 2017. http://indico.ictp.it/event/8002/session/41/contribution/303

[C – 4] **Awais Qadir**, Zsolt Fogarassy, Zsolt E. Horvath, Katalin Balazsi , Csaba Balazsi, The effect of oxidized nanosized silicon nitride powder particles on the structural and mechanical properties of Si_3N_4/CNTs composite by hot isostatic pressing ***(Oral Talk)***, FEMS JUNIOR EUROMAT CONFERENCE 2018, Budapest, Hungary, July 8 –12, 2018, page 64. https://static.akcongress.com/downloads/euromat/JuniorEuromat2018_Bookofabstracts.pdf

[C – 5] **Awais Qadir**, Zsolt Fogarassy, Zsolt E. Horváth, Katalin Balázsi, Csaba Balázsi, Effect of oxidized Si_3N_4 powder particles on structural and mechanical properties of sintered Si_3N_4 material ***(Oral Talk)***, Fine Ceramics Day 2018, Hungarian Academy of Sciences, Budapest, Hungary, April 12, 2018.

[C – 6] **Awais Qadir**, Zsolt Fogarassy, Zsolt E. Horváth, Katalin Balázsi, Csaba Balázsi, Effect of oxidized Si_3N_4 powder particles on structural and mechanical properties of sintered Si_3N_4 material ***(Oral Talk)***, "17th PhD Students Materials Science Day", University of Pannon, Veszprem, Hungary, Dec. 4. 2017.

[C – 7] **Awais Qadir**, Jan Dusza, Processing and properties of silicon nitride + MWCNTs composites prepared from oxidized α-Si3N4 starting powder, ***(Poster Presentation)*** 6th international conference "Fractography of Advanced Ceramics" in the Smolenice Castle Congress Center, Smolenice SAS on September 08 - 11, 2019. http://www.imr.saske.sk/confer/fac2019/index.htm

[S – 8]_**Awais Qadir**, Jan Dusza, Processing and properties of silicon nitride + MWCNTs composites prepared from oxidized α-Si3N4 starting powder, 13th Conference for Young Scientists in Ceramics, CYSC-2019, Novi Sad, Serbia, October 16-19, 2019 http://cysc.mima.solutions/wp-content/uploads/2019/10/Book-of-Abstarcts-CYSC-2019.pdf

8.4. Scientific Impact of my research

Impact of research has been calculated and presented below.

Total Publications = 9	PhD work-related Publications = 6
Cumulative Impact Factor = 24.546	PhD work Cumulative Impact Factor = 11.685
All Citations = 64	PhD work-related Citations = 10

9. Reference

[1] H. Deville and F. Wöhler, “On the direct compound silicon nitride,” *Liebigs Ann. der Chemie*, vol. 110, pp. 248–250, 1859, Accessed: Apr. 22, 2020. [Online]. Available: https://scholar.google.com/scholar?hl=en&as_sdt=0%2C5&q=Deville%2C+H.S.-C.%3B+Wöhler%2C+F.+On+the+direct+compound+silicon+nitride.+Liebigs+Ann.+Chem.+Pharm+1859%2C+110%2C+248–250.&btnG=.

[2] J. F. Collins and R. W. Gerby, “New Refractory Uses For Silicon Nitride Reported,” *JOM*, vol. 7, no. 5, pp. 612–615, May 1955, doi: 10.1007/bf03377548.

[3] G. G. Deeley, J. M. Herbert, and N. C. Moore, “Dense silicon nitride,” *Powder Metall.*, vol. 4, no. 8, pp. 145–151, 1961, doi: 10.1179/pom.1961.4.8.011.

[4] M. MITOMO and Y. TAJIMA, “Sintering, Properties and Applications of Silicon Nitride and Sialon Ceramics,” *J. Ceram. Soc. Japan*, vol. 99, no. 1154, pp. 1014–1025, 1991, doi: 10.2109/jcersj.99.1014.

[5] G. R. TERWILLIGER, “Properties of Sintered Si3N4,” *J. Am. Ceram. Soc.*, vol. 57, no. 1, pp. 48–49, Jan. 1974, doi: 10.1111/j.1151-2916.1974.tb11368.x.

[6] M. Mitomo, “Pressure sintering of Si3N4,” *J. Mater. Sci.*, vol. 11, no. 6, pp. 1103–1107, Jun. 1976, doi: 10.1007/BF00553119.

[7] D. R. U. W. D. Kingery, H.K. Bowen, *Introduction to ceramics*, 2nd Editio. New York: John Wiley & Sons, 1976.

[8] C. B. Carter and M. G. Norton, “Ceramic Materials,” in *Ceramic Materials*, 2nd ed., New York: Springer New York, 2013, pp. 3–15.

[9] X. Ma, C. Li, F. Wang, and W. Zhang, “Thermodynamic assessment of the Si–N system,” *Calphad*, vol. 27, no. 4, pp. 383–388, Apr. 2003, doi: 10.1016/j.calphad.2003.12.005.

[10] W. Kaiser and C. D. Thurmond, “Nitrogen in silicon,” *J. Appl. Phys.*, vol. 30, no. 3, pp. 427–431, 1959, doi: 10.1063/1.1735180.

[11] J. M. Arrowsmith, “A new silicon nitride phase in commercial silicon killed steels,” *J. Iron Steel Inst.*, vol. 201, no. 8, p. 699, 1963.

[12] E. Hengge, “Über die Darstellung eines neuen Siliciumsubnitrides (Si6N2)n,” *Zeitschrift für Anorg. und Allg. Chemie*, vol. 315, no. 5–6, pp. 298–304, Apr. 1962, doi: 10.1002/zaac.19623150509.

[13] D. Hardie and K. H. Jack, “Crystal structures of silicon nitride,” *Nature*, vol. 180, no.

4581, pp. 332–333, Aug. 1957, doi: 10.1038/180332a0.

[14] A. Zerr, G. Miehe, G. Serghiou, M. Schwarz, E. Kroke, R. Riedel, H. Fueß, P. Kroll, and R. Boehler, “Synthesis of cubic silicon nitride,” *Nature*, vol. 400, no. 6742, pp. 340–342, Jul. 1999, doi: 10.1038/22493.

[15] J. Z. Jiang, F. Kragh, D. J. Frost, K. StÃ¥hl, and H. Lindelov, “Hardness and thermal stability of cubic silicon nitride,” *J. Phys. Condens. Matter*, vol. 13, no. 22, pp. L515–L520, 2001, doi: 10.1088/0953-8984/13/22/111.

[16] G. Petzow and M. Herrmann, “Silicon Nitride Ceramics,” 2002, pp. 47–167.

[17] S. Hampshire, “Silicon Nitride Ceramics,” in *Engineered Ceramics: Current Status and Future Prospects*, Jansen M., Heidelberg: Springer, Berlin, Heidelberg, 2016, pp. 77–97.

[18] H. Klemm, “Silicon Nitride for High-Temperature Applications,” *J. Am. Ceram. Soc.*, vol. 93, no. 6, pp. 1501–1522, Jun. 2010, doi: 10.1111/j.1551-2916.2010.03839.x.

[19] G. Wötting, J. Hennicke, H. Feuer, K.-H. Thiemann, D. Vollmer, E. Fechter, F. Sticher, and A. Geyer, “Reliability and reproducibility of silicon nitride valves: experiences of a field test,” *Ceram. Mater. components engines*, pp. 181–185, 2001, [Online]. Available: http://files/183/books.html.

[20] T. F. Ariff, N. S. Shafie, and Z. M. Zahir, “Wear Analysis of Silicon Nitride (Si3N4) Cutting Tool in Dry Machining of T6061 Aluminium Alloy,” *Applied Mechanics and Materials*. Mar. 24, 2013, [Online]. Available: https://www.scientific.net/AMM.268-270.563.

[21] R. Haubner, M. Herrmann, B. Lux, G. Petzow, R. Weissenbacher, and M. Wilhelm, *High performance non-oxide ceramics II*, vol. 102. Springer, 2003.

[22] F. L. Riley, “Silicon Nitride and Related Materials,” *J. Am. Ceram. Soc.*, vol. 83, no. 2, pp. 245–265, Dec. 2004, doi: 10.1111/j.1151-2916.2000.tb01182.x.

[23] B. I. Kharisov and O. V. Kharissova, “Classic Carbon Nanostructures,” in *Carbon Allotropes: Metal-Complex Chemistry, Properties and Applications*, Springer International Publishing, 2019, pp. 35–109.

[24] H. W. Kroto, J. R. Heath, S. C. O’Brien, R. F. Curl, and R. E. Smalley, “C60: Buckminsterfullerene,” *Nature*, vol. 318, no. 6042, pp. 162–163, 1985, doi: 10.1038/318162a0.

[25] S. Iijima, “Helical microtubules of graphitic carbon,” *Nature*, vol. 354, no. 6348, pp. 56–58, 1991, doi: 10.1038/354056a0.

[26] K. S. Novoselov, A. K. Geim, S. V. Morozov, D. Jiang, M. I. Katsnelson, I. V.

Grigorieva, S. V. Dubonos, and A. A. Firsov, “Two-dimensional gas of massless Dirac fermions in graphene,” *Nature*, vol. 438, no. 7065, pp. 197–200, Nov. 2005, doi: 10.1038/nature04233.

[27] P. J. Harris, “F. Carbon nanotube composites,” *Int. Mater. Rev.*, vol. 49, no. 1, pp. 31–43, 2004.

[28] R. H. Baughman, A. A. Zakhidov, and W. A. de Heer, “Carbon Nanotubes--the Route Toward Applications,” *Science (80-.).*, vol. 297, no. 5582, pp. 787–792, Mar. 2002, doi: 10.1126/science.1060928.

[29] S. Iijima, C. Brabec, A. Maiti, and J. Bernholc, “Structural flexibility of carbon nanotubes,” *J. Chem. Phys.*, vol. 104, no. 5, pp. 2089–2092, Mar. 1996, doi: 10.1063/1.470966.

[30] L. X. Zheng, M. J. O’Connell, S. K. Doorn, X. Z. Liao, Y. H. Zhao, E. A. Akhadov, M. A. Hoffbauer, B. J. Roop, Q. X. Jia, R. C. Dye, D. E. Peterson, S. M. Huang, J. Liu, and Y. T. Zhu, “Ultralong single-wall carbon nanotubes,” *Nat. Mater.*, vol. 3, no. 10, pp. 673–676, Mar. 2004, doi: 10.1038/nmat1216.

[31] R. S. Ruoff and D. C. Lorents, “Mechanical and thermal properties of carbon nanotubes,” *Carbon N. Y.*, vol. 33, no. 7, pp. 925–930, Mar. 1995, doi: 10.1016/0008-6223(95)00021-5.

[32] M. M. J. Treacy, T. W. Ebbesen, and J. M. Gibson, “Exceptionally high Young’s modulus observed for individual carbon nanotubes,” *Nature*, vol. 381, no. 6584, p. 678, Mar. 1996, doi: 10.1038/381678a0.

[33] K. Varshney, “Carbon Nanotubes: A Review on Synthesis, Properties and Applications,” *Int. J. Eng. Res. Gen. Sci.*, vol. 2, no. 4, 2014, Accessed: Apr. 22, 2020. [Online]. Available: www.ijergs.org.

[34] C. Laurent, A. Peigney, O. Dumortier, and A. Rousset, “Carbon nanotubes–Fe–Alumina nanocomposites. Part II: microstructure and mechanical properties of the hot-Pressed composites,” *J. Eur. Ceram. Soc.*, vol. 18, no. 14, pp. 2005–2013, Mar. 1998, doi: 10.1016/S0955-2219(98)00142-3.

[35] Y. Huh, J. Y. Lee, J. Cheon, Y. K. Hong, J. Y. Koo, T. J. Lee, and C. J. Lee, “Controlled growth of carbon nanotubes over cobalt nanoparticles by thermal chemical vapor deposition,” *J. Mater. Chem.*, vol. 13, no. 9, pp. 2297–2300, Mar. 2003, doi: 10.1039/B304582J.

[36] M. Endo, R. Saito, M. S. Dresselhaus, and G. Dresselhaus, “Carbon nanotubes: preparation and properties,” *Ed. by TW Ebbesen*, pp. 35–110, 1997.

[37] K. S. Novoselov, D. Jiang, F. Schedin, T. J. Booth, V. V. Khotkevich, S. V. Morozov, and A. K. Geim, “Two-dimensional atomic crystals,” *Proc. Natl. Acad. Sci. U. S. A.*, vol. 102, no. 30, pp. 10451–10453, Jul. 2005, doi: 10.1073/pnas.0502848102.

[38] M. Notarianni, J. Liu, K. Vernon, and N. Motta, “Synthesis and applications of carbon nanomaterials for energy generation and storage,” *Beilstein Journal of Nanotechnology*, vol. 7, no. 1. Beilstein-Institut Zur Forderung der Chemischen Wissenschaften, pp. 149–196, Feb. 01, 2016, doi: 10.3762/bjnano.7.17.

[39] C. Lee, X. Wei, J. W. Kysar, and J. Hone, “Measurement of the Elastic Properties and Intrinsic Strength of Monolayer Graphene,” *Science (80-.).*, vol. 321, no. 5887, pp. 385–388, 2008, doi: 10.1126/science.1157996.

[40] K. Cao, S. Feng, Y. Han, L. Gao, T. Hue Ly, Z. Xu, and Y. Lu, “Elastic straining of free-standing monolayer graphene,” *Nat. Commun.*, vol. 11, no. 1, pp. 1–7, Dec. 2020, doi: 10.1038/s41467-019-14130-0.

[41] “Nobel Prize ® and the Nobel Prize ® medal design mark are registrated trademarks of the Nobel Foundation Scientific Background on the Nobel Prize in Physics 2010 G R A P H E N E compiled by the Class for Physics of the Royal Swedish Academy of Sciences,” 2010.

[42] P. Šajgalik, J. Dusza, and M. J. Hoffmann, “Relationship between Microstructure, Toughening Mechanisms, and Fracture Toughness of Reinforced Silicon Nitride Ceramics,” *J. Am. Ceram. Soc.*, vol. 78, no. 10, pp. 2619–2624, Oct. 1995, doi: 10.1111/j.1151-2916.1995.tb08031.x.

[43] J. Dusza and P. Šajgalík, “Mechanical properties of Si3N4 + β-Si3N4 whisker reinforced ceramics,” *J. Eur. Ceram. Soc.*, vol. 9, no. 1, pp. 9–17, 1992, doi: 10.1016/0955-2219(92)90071-K.

[44] J. J. Kruzic, R. L. Satet, M. J. Hoffmann, R. M. Cannon, and R. O. Ritchie, “The Utility of R-Curves for Understanding Fracture Toughness-Strength Relations in Bridging Ceramics,” *J. Am. Ceram. Soc.*, vol. 91, no. 6, pp. 1986–1994, Jun. 2008, doi: 10.1111/j.1551-2916.2008.02380.x.

[45] T. Fett, S. Fünfschilling, M. J. Hoffmann, R. Oberacker, H. Jelitto, and G. A. Schneider, “R-Curve Determination for the Initial Stage of Crack Extension in Si3N4,” *J. Am. Ceram. Soc.*, vol. 91, no. 11, pp. 3638–3642, Nov. 2008, doi: 10.1111/j.1551-2916.2008.02750.x.

[46] S. Pasupuleti, R. Peddetti, S. Santhanam, K.-P. Jen, Z. N. Wing, M. Hecht, and J. P. Halloran, “Toughening behavior in a carbon nanotube reinforced silicon nitride

composite," *Mater. Sci. Eng. A*, vol. 491, no. 1, pp. 224–229, Mar. 2008, doi: 10.1016/j.msea.2008.04.058.

[47] M. Matsuoka, J. Tatami, T. Wakihara, K. Komeya, and T. Meguro, "Improvement of strength of carbon nanotube-dispersed Si3N4 ceramics by bead milling and adding lower-temperature sintering aids," *J. Asian Ceram. Soc.*, vol. 2, no. 3, pp. 199–203, May 2014, doi: 10.1016/j.jascer.2014.02.005.

[48] O. Tapasztó, P. Kun, F. Wéber, G. Gergely, K. Balázsi, J. Pfeifer, P. Arató, A. Kidari, S. Hampshire, and C. Balázsi, "Silicon nitride based nanocomposites produced by two different sintering methods," *Ceram. Int.*, vol. 37, no. 8, pp. 3457–3461, Mar. 2011, doi: 10.1016/j.ceramint.2011.05.150.

[49] C. Y. Tian and H. Jiang, "Preparation and mechanical properties of carbon nanotube-silicon nitride nano-ceramic matrix composites," *IOP Conf. Ser. Mater. Sci. Eng.*, vol. 292, p. 12076, May 2018, doi: 10.1088/1757-899X/292/1/012076.

[50] P. Rutkowski, L. Stobierski, D. Zientara, L. Jaworska, P. Klimczyk, and M. Urbanik, "The influence of the graphene additive on mechanical properties and wear of hot-pressed Si3N4 matrix composites," *J. Eur. Ceram. Soc.*, vol. 35, no. 1, pp. 87–94, 2015, doi: https://doi.org/10.1016/j.jeurceramsoc.2014.08.004.

[51] L. S. Walker, V. R. Marotto, M. A. Rafiee, N. Koratkar, and E. L. Corral, "Toughening in Graphene Ceramic Composites," *ACS Nano*, vol. 5, no. 4, pp. 3182–3190, Apr. 2011, doi: 10.1021/nn200319d.

[52] Y. Yang, B. Li, C. Zhang, S. Wang, K. Liu, and B. Yang, "Fabrication and properties of graphene reinforced silicon nitride composite materials," *Mater. Sci. Eng. A*, vol. 644, pp. 90–95, 2015, doi: https://doi.org/10.1016/j.msea.2015.07.062.

[53] A. Kovalčíková, C. Balázsi, J. Dusza, and O. Tapasztó, "Mechanical properties and electrical conductivity in a carbon nanotube reinforced silicon nitride composite," *Ceram. Int.*, vol. 38, no. 1, pp. 527–533, Mar. 2012, doi: 10.1016/j.ceramint.2011.07.038.

[54] M. Belmonte, S. M. Vega-Díaz, A. Morelos-Gómez, P. Miranzo, M. I. Osendi, and M. Terrones, "Nitrogen-doped-CNTs/Si3N4 nanocomposites with high electrical conductivity," *J. Eur. Ceram. Soc.*, vol. 34, no. 5, pp. 1097–1104, Mar. 2014, doi: 10.1016/j.jeurceramsoc.2013.11.026.

[55] Z. Y. Huang, X. J. Liu, X. W. Sun, and L. P. Huang, "CNTs/Si3N4 composites fabricated by reaction bonded processing," in *Key Engineering Materials*, 2007, vol. 336-338 II, pp. 1277–1279.

[56] C. Balázsi, F. Wéber, Z. Kövér, Z. Shen, Z. Kónya, Z. Kasztovszky, Z. Vértesy, L. P. Biró, I. Kiricsi, and P. Arató, “Application of carbon nanotubes to silicon nitride matrix reinforcements,” *Curr. Appl. Phys.*, vol. 6, no. 2, pp. 124–130, Mar. 2006, doi: 10.1016/j.cap.2005.07.024.

[57] C. Balázsi, Z. Shen, Z. Kónya, Z. Kasztovszky, F. Wéber, Z. Vértesy, L. P. Biró, I. Kiricsi, and P. Arató, “Processing of carbon nanotube reinforced silicon nitride composites by spark plasma sintering,” *Compos. Sci. Technol.*, vol. 65, no. 5, pp. 727–733, Mar. 2005, doi: 10.1016/j.compscitech.2004.10.006.

[58] E. L. Corral, J. Cesarano, A. Shyam, E. Lara-Curzio, N. Bell, J. Stuecker, N. Perry, M. Di Prima, Z. Munir, J. Garay, and E. V Barrera, “Engineered Nanostructures for Multifunctional Single-Walled Carbon Nanotube Reinforced Silicon Nitride Nanocomposites,” *J. Am. Ceram. Soc.*, vol. 91, no. 10, pp. 3129–3137, Mar. 2008, doi: 10.1111/j.1551-2916.2008.02533.x.

[59] A. Saleem, Y. Zhang, H. Gong, M. K. Majeed, J. Jing, X. Lin, and M. Z. Ashfaq, “Enhanced thermal conductivity and mechanical properties of a GNP reinforced Si3N4 composite,” *RSC Adv.*, vol. 9, no. 68, pp. 39986–39992, 2019, doi: 10.1039/c9ra09286b.

[60] Y. Hu, Z. Chen, J. Zhang, G. Xiao, M. Yi, W. Zhang, and C. Xu, “Preparation and mechanical properties of Si3N4 nanocomposites reinforced by Si3N4@rGO particles,” *J. Am. Ceram. Soc.*, vol. 102, no. 11, pp. 6991–7002, Nov. 2019, doi: 10.1111/jace.16546.

[61] O. Tapasztó, V. Puchy, Z. E. Horváth, Z. Fogarassy, E. Bódis, Z. Károly, K. Balázsi, J. Dusza, and L. Tapasztó, “The effect of graphene nanoplatelet thickness on the fracture toughness of Si 3 N 4 composites,” *Ceram. Int.*, vol. 45, no. 6, pp. 6858–6862, Apr. 2019, doi: 10.1016/j.ceramint.2018.12.180.

[62] C. Ramirez, P. Miranzo, M. Belmonte, M. I. Osendi, P. Poza, S. M. Vega-Diaz, and M. Terrones, “Extraordinary toughening enhancement and flexural strength in Si3N4 composites using graphene sheets,” *J. Eur. Ceram. Soc.*, vol. 34, no. 2, pp. 161–169, Feb. 2014, doi: 10.1016/j.jeurceramsoc.2013.08.039.

[63] E. Bódis, I. Cora, P. Németh, O. Tapasztó, M. Mohai, S. Tóth, Z. Károly, and J. Szépvölgyi, “Toughening of silicon nitride ceramics by addition of multilayer graphene,” *Ceram. Int.*, vol. 45, no. 4, pp. 4810–4816, 2019, doi: https://doi.org/10.1016/j.ceramint.2018.11.176.

[64] E. Bódis, O. Tapasztó, Z. Károly, P. Fazekas, S. Klébert, A. M. Keszler, K. Balázsi,

and J. Szépvölgyi, “Spark plasma sintering of Si3N4/multilayer graphene composites,” *Open Chem.*, vol. 13, no. 1, pp. 484–489, Dec. 2015, doi: 10.1515/chem-2015-0064.

[65] M. Maros B., A. K. Németh, Z. Károly, E. Bódis, Z. Maros, O. Tapasztó, and K. Balázsi, “Tribological characterisation of silicon nitride/multilayer graphene nanocomposites produced by HIP and SPS technology,” *Tribol. Int.*, vol. 93, pp. 269–281, Aug. 2015, doi: 10.1016/j.triboint.2015.08.041.

[66] P. Hvizdoš, V. Puchý, A. Duszová, J. Dusza, and C. Balázsi, “Tribological and electrical properties of ceramic matrix composites with carbon nanotubes,” *Ceram. Int.*, vol. 38, no. 7, pp. 5669–5676, Mar. 2012, doi: 10.1016/j.ceramint.2012.04.010.

[67] J. Gonzalez-Julian, J. Schneider, P. Miranzo, M. I. Osendi, and M. Belmonte, “Enhanced Tribological Performance of Silicon Nitride-Based Materials by Adding Carbon Nanotubes,” *J. Am. Ceram. Soc.*, vol. 94, no. 8, pp. 2542–2548, Mar. 2011, doi: 10.1111/j.1551-2916.2011.04391.x.

[68] O. Koszor, A. Lindemann, F. Davin, and C. Balázsi, “Observation of thermophysical and tribological properties of CNT reinforced Si3N4,” in *Key Engineering Materials*, 2009, vol. 409, pp. 354–357, doi: 10.4028/www.scientific.net/KEM.409.354.

[69] J. Balko, P. Hvizdoš, and C. Balázsi, “WEAR DAMAGE IN SILICON NITRIDE COMPOSITES WITH GRAPHENE AND CARBON NANOTUBES,” *Acta Metall. Slovaca - Conf.*, vol. 3, no. 0, pp. 276–281, May 2013, doi: 10.12776/amsc.v3i0.140.

[70] O. Tapasztó, J. Balko, V. Puchy, P. Kun, G. Dobrik, Z. Fogarassy, Z. E. Horváth, J. Dusza, K. Balázsi, C. Balázsi, and L. Tapasztó, “Highly wear-resistant and low-friction Si3N4 composites by addition of graphene nanoplatelets approaching the 2D limit,” *Sci. Rep.*, vol. 7, no. 1, Dec. 2017, doi: 10.1038/s41598-017-10290-5.

[71] M. Belmonte, C. Ramírez, J. González-Julián, J. Schneider, P. Miranzo, and M. I. Osendi, “The beneficial effect of graphene nanofillers on the tribological performance of ceramics,” *Carbon N. Y.*, vol. 61, pp. 431–435, 2013, doi: https://doi.org/10.1016/j.carbon.2013.04.102.

[72] P. Hvizdoš, J. Dusza, and C. Balázsi, “Tribological properties of Si3N4–graphene nanocomposites,” *J. Eur. Ceram. Soc.*, vol. 33, no. 12, pp. 2359–2364, 2013, doi: https://doi.org/10.1016/j.jeurceramsoc.2013.03.035.

[73] C. Balázsi, Z. Fogarassy, O. Tapasztó, A. Kailer, C. Schröder, M. Parchoviansky, D. Galusek, J. Dusza, and K. Balázsi, “Si3N4/graphene nanocomposites for tribological application in aqueous environments prepared by attritor milling and hot pressing,” *J. Eur. Ceram. Soc.*, vol. 37, no. 12, pp. 3797–3804, Sep. 2017, doi:

10.1016/j.jeurceramsoc.2017.03.022.

[74] S. Yoshio, J. Tatami, T. Yamakawa, T. Wakihara, K. Komeya, T. Meguro, K. Aramaki, and K. Yasuda, “Dispersion of carbon nanotubes in ethanol by a bead milling process,” *Carbon N. Y.*, vol. 49, no. 13, pp. 4131–4137, May 2011, doi: 10.1016/j.carbon.2011.05.033.

[75] M. B.Maros and A. K. Németh, “Wear maps of HIP sintered Si3N4/MLG nanocomposites for unlike paired tribosystems under ball-on-disc dry sliding conditions,” *J. Eur. Ceram. Soc.*, vol. 37, no. 14, pp. 4357–4369, Nov. 2017, doi: 10.1016/j.jeurceramsoc.2017.05.005.

[76] J. Gonzalez-Julian, A. Datye, K.-H. Wu, J. Schneider, and M. Belmonte, “Robust and wear resistant in-situ carbon nanotube/Si3N4 nanocomposites with a high loading of nanotubes,” *Carbon N. Y.*, vol. 72, pp. 338–347, Mar. 2014, doi: 10.1016/j.carbon.2014.02.014.

[77] M. Matsuoka, S. Yoshio, T. Yamakawa, J. Tatami, T. Wakihara, K. Komeya, and T. Meguro, “Development of CNT-Si3N4 Composites with High Strength and Electrical Conductivity by Adding HfO2,” *Trans. Mater. Res. Soc. Japan*, vol. 37, no. 1, pp. 11–14, Mar. 2012, doi: 10.14723/tmrsj.37.11.

[78] C. Balázsi, Z. Kónya, F. Wéber, L. P. Biró, and P. Arató, “Preparation and characterization of carbon nanotube reinforced silicon nitride composites,” *Mater. Sci. Eng. C*, vol. 23, no. 6, pp. 1133–1137, Mar. 2003, doi: 10.1016/j.msec.2003.09.085.

[79] V. Puchý, P. Hvizdoš, M. Ivor, D. Medveď, M. Hnatko, A. Kovalčíková, R. Sedlák, and J. Dusza, “Preparation, friction, wear, and fracture of the Si3N4-Ag-GNPs composites prepared by SPS,” *J. Eur. Ceram. Soc.*, vol. 40, no. 14, pp. 4853–4859, 2020, doi: https://doi.org/10.1016/j.jeurceramsoc.2020.04.056.

[80] P. Rutkowski, “Subtractive laser processing of anisotropic Si3N4- graphene platelet (GPL) materials,” *Mater. Lett.*, vol. 263, p. 127207, 2020, doi: https://doi.org/10.1016/j.matlet.2019.127207.

[81] J. Zhang, J. Zhang, G. Xiao, Z. Chen, M. Yi, Y. Zhang, and C. Xu, “Orentational effect of graphene on the friction and wear behavior of Si3N4/TiC based composite ceramic tool materials,” *Ceram. Int.*, vol. 46, no. 3, pp. 3550–3557, 2020, doi: https://doi.org/10.1016/j.ceramint.2019.10.072.

[82] C. Balázsi, K. Sedláčková, and Z. Czigány, “Structural characterization of Si3N4–carbon nanotube interfaces by transmission electron microscopy,” *Compos. Sci. Technol.*, vol. 68, no. 6, pp. 1596–1599, Mar. 2008, doi:

10.1016/j.compscitech.2007.11.009.

[83] O. Tapasztó and C. Balázsi, “The effect of milling time on the sintering kinetics of Si3N4 based nanocomposites,” *Ceram. Int.*, vol. 36, no. 7, pp. 2247–2251, Mar. 2010, doi: 10.1016/j.ceramint.2010.06.006.

[84] A. Nieto, A. Bisht, D. Lahiri, C. Zhang, and A. Agarwal, “Graphene reinforced metal and ceramic matrix composites: a review,” *Int. Mater. Rev.*, vol. 62, no. 5, pp. 241–302, 2017, doi: 10.1080/09506608.2016.1219481.

[85] J. K. Sonber, T. S. R. Ch. Murthy, C. Subramanian, R. C. Hubli, and A. K. Suri, “Processing Methods for Ultra High Temperature Ceramics,” in *MAX Phases and Ultra-High Temperature Ceramics for Extreme Environments*, IGI Global, 2013, pp. 180–202.

[86] V. Viswanathan, T. Laha, K. Balani, A. Agarwal, and S. Seal, “Challenges and advances in nanocomposite processing techniques,” *Mater. Sci. Eng. R Reports*, vol. 54, no. 5, pp. 121–285, 2006, doi: https://doi.org/10.1016/j.mser.2006.11.002.

[87] J. M. Torralba, “3.11 - Improvement of Mechanical and Physical Properties in Powder Metallurgy,” S. Hashmi, G. F. Batalha, C. J. Van Tyne, and B. B. T.-C. M. P. Yilbas, Eds. Oxford: Elsevier, 2014, pp. 281–294.

[88] V. Tyrpekl, C. Berkmann, M. Holzhäuser, F. Köpp, M. Cologna, T. Wangle, and J. Somers, “Implementation of a spark plasma sintering facility in a hermetic glovebox for compaction of toxic, radiotoxic, and air sensitive materials,” *Rev. Sci. Instrum.*, vol. 86, no. 2, p. 23904, Feb. 2015, doi: 10.1063/1.4913529.

[89] J. Dusza, J. Morgiel, A. Duszová, L. Kvetková, M. Nosko, P. Kun, and C. Balázsi, “Microstructure and fracture toughness of Si 3N 4+graphene platelet composites,” *J. Eur. Ceram. Soc.*, vol. 32, no. 12, pp. 3389–3397, Sep. 2012, doi: 10.1016/j.jeurceramsoc.2012.04.022.

[90] R. L. Smith and G. E. Sandly, “An Accurate Method of Determining the Hardness of Metals, with Particular Reference to Those of a High Degree of Hardness,” *Proc. Inst. Mech. Eng.*, vol. 102, no. 1, pp. 623–641, Jun. 1922, doi: 10.1243/pime_proc_1922_102_033_02.

[91] “BS EN 843-4:2005 - Advanced technical ceramics. Mechanical properties of monolithic ceramics at room temperature. Vickers, Knoop and Rockwell superficial hardness,” 2007. https://shop.bsigroup.com/ProductDetail?pid=000000000030055679 (accessed Aug. 25, 2020).

[92] G. D. Quinn and R. C. Bradt, “On the Vickers Indentation Fracture Toughness Test,” *J.*

Am. Ceram. Soc., vol. 90, no. 3, pp. 673–680, Feb. 2007, doi: 10.1111/j.1551-2916.2006.01482.x.

[93] C. B. Ponton and R. D. Rawlings, "Vickers indentation fracture toughness test Part 1 Review of literature and formulation of standardised indentation toughness equations," *Mater. Sci. Technol.*, vol. 5, no. 9, pp. 865–872, Feb. 1989, doi: 10.1179/mst.1989.5.9.865.

[94] G. D. Quinn, "Fracture Toughness of Ceramics by the Vickers Indentation Crack Length Method: A Critical Review," John Wiley & Sons, Ltd, 2008, pp. 45–62.

[95] A. Moradkhani, H. Baharvandi, M. Tajdari, H. Latifi, and J. Martikainen, "Determination of fracture toughness using the area of micro-crack tracks left in brittle materials by Vickers indentation test," *J. Adv. Ceram.*, vol. 2, no. 1, pp. 87–102, Mar. 2013, doi: 10.1007/s40145-013-0047-z.

[96] G. R. ANSTIS, P. CHANTIKUL, B. R. LAWN, and D. B. MARSHALL, "A Critical Evaluation of Indentation Techniques for Measuring Fracture Toughness: I, Direct Crack Measurements," *J. Am. Ceram. Soc.*, vol. 64, no. 9, pp. 533–538, Sep. 1981, doi: 10.1111/j.1151-2916.1981.tb10320.x.

[97] D. K. Shetty, I. G. Wright, P. N. Mincer, and A. H. Clauer, "Indentation fracture of WC-Co cermets," *J. Mater. Sci.*, vol. 20, no. 5, pp. 1873–1882, May 1985, doi: 10.1007/BF00555296.

[98] M. Ashby, *Materials Selection in Mechanical Design - 5th Edition*. Butterworth-Heinemann, 2016.

[99] S. Affatato and L. Grillini, "Topography in bio-tribocorrosion," in *Bio-Tribocorrosion in Biomaterials and Medical Implants*, Elsevier Inc., 2013, pp. 1–21.

[100] M. Torbacke, Å. K. Rudolphi, and E. Kassfeldt, *Lubricants: Introduction to Properties and Performance*. John Wiley & Sons, 2014.

[101] K. Holmberg and A. Erdemir, "Influence of tribology on global energy consumption, costs and emissions," *Friction*, vol. 5, no. 3. Tsinghua University Press, pp. 263–284, Sep. 01, 2017, doi: 10.1007/s40544-017-0183-5.

[102] W. A. Glaeser, "Friction," *Lubr. Eng.*, vol. 48, no. 2, pp. 129–132, Jan. 1992, doi: 10.1016/b978-0-7506-1683-6.50031-x.

[103] "What is Friction?" https://www.face-kyowa.co.jp/english/en_science/en_what_friction.html (accessed Apr. 22, 2021).

[104] A. Ball, "The mechanisms of wear, and the performance of engineering materials," *J. South. African Inst. Min. Metall.*, vol. 86, no. 1, pp. 1–13, 1986.

[105] P. C. Milak, F. D. Minatto, A. De Noni, and O. R. K. Montedo, “Wear performance of alumina-based ceramics - A review of the influence of microstructure on erosive wear,” *Ceramica*, vol. 61, no. 357, pp. 88–103, Jan. 2015, doi: 10.1590/0366-69132015613571871.

[106] G. Stachowiak, *Wear: materials, mechanisms and practice*. West Sussex, England: John Wiley & Sons, 2006.

[107] “High Purity Silicon Nitride Powder - UBE INDUSTRIES,LTD.” https://www.ube.com/contents/en/chemical/ceramics/ceramics.html (accessed Jun. 29, 2020).

[108] J. Tatami, T. Katashima, K. Komeya, T. Meguro, and T. Wakihara, “Electrically Conductive CNT-Dispersed Silicon Nitride Ceramics,” *J. Am. Ceram. Soc.*, vol. 88, no. 10, pp. 2889–2893, Mar. 2005, doi: 10.1111/j.1551-2916.2005.00539.x.

[109] J. Intrater, “Mechanical Alloying and Milling , C. Suryanarayana,” *Mater. Manuf. Process.*, vol. 22, no. 6, pp. 790–791, Jun. 2007, doi: 10.1080/10426910701416344.

[110] K. H. Stern, “Oxidation of silicon, silicon carbide (SiC) and silicon nitride (Si3N4) (No. NRL-MR-5774),” WASHINGTON DC., 1986.

[111] K. Balázsi, M. Furkó, Z. Liao, J. Gluch, D. Medved, R. Sedlák, J. Dusza, E. Zschech, and C. Balázsi, “Porous sandwich ceramic of layered silicon nitride-zirconia composite with various multilayered graphene content,” *J. Alloys Compd.*, vol. 832, p. 154984, Aug. 2020, doi: 10.1016/j.jallcom.2020.154984.

[112] L. Wang, T.-Y. Tien, and I.-W. Chen, “Formation of β-Silicon Nitride Crystals from (Si,Al,Mg,Y)(O,N) Liquid: I, Phase, Composition, and Shape Evolutions,” *J. Am. Ceram. Soc.*, vol. 86, no. 9, pp. 1578–1585, Sep. 2003, doi: 10.1111/j.1151-2916.2003.tb03517.x.

[113] D. Bučevac, S. Boškovic, and B. Matović, “Kinetics of the α-β phase transformation in seeded Si 3N4 ceramics,” *Sci. Sinter.*, vol. 40, no. 3, pp. 263–270, 2008, doi: 10.2298/SOS0803263B.

[114] R. L. TSAI and R. RAJ, “Dissolution Kinetics of beta-Si3N4 in an Mg-Si-O-N Glass,” *J. Am. Ceram. Soc.*, vol. 65, no. 5, pp. 270–274, May 1982, doi: 10.1111/j.1151-2916.1982.tb10431.x.

[115] B. Bergman and H. Heping, “The influence of different oxides on the formation of Si2N2O from SiO2 and Si3N4,” *J. Eur. Ceram. Soc.*, vol. 6, no. 1, pp. 3–8, Jan. 1990, doi: 10.1016/0955-2219(90)90028-E.

[116] Z. K. Huang, P. Greil, and G. Petzow, “Formation of silicon oxinitride from Si3N4 and

SiO2 in the presence of Al2O3," *Ceram. Int.*, vol. 10, no. 1, pp. 14–17, Jan. 1984, doi: 10.1016/0272-8842(84)90017-8.

[117] s. Hampshire and K. H. Jack, "KINETICS OF DENSIFICATION AND PHASE TRANSFORMATION OF NITROGEN CERAMICS.," in *Proceedings of the British Ceramic Society*, Jun. 1981, no. 31, pp. 37–49.

[118] D. S. Park, H. J. Choi, B. D. Han, H. D. Kim, and D. S. Lim, "Effect of Si2N2O content on the microstructure, properties, and erosion of silicon nitride-Si2N2O in situ composites," *J. Mater. Res.*, vol. 17, no. 9, pp. 2275–2280, 2002, doi: 10.1557/JMR.2002.0334.

[119] B. Fan, W. Li, F. Zhang, H. Li, R. Zhang, G. Liu, F. Qian, and Y. Chen, "Fabrication and properties of Si2N2O ceramics for microwave sintering furnace," *Process. Appl. Ceram.*, vol. 14, no. 1, pp. 32–39, 2020, doi: 10.2298/PAC2001032F.

[120] S. Lin, F. Ye, J. Ma, J. Ding, Q. Liu, and S. Dong, "Fabrication and properties of porous boron nitride/silicon oxynitride ceramic composites via gas pressure sintering," *Mater. Des.*, vol. 87, pp. 272–277, Dec. 2015, doi: 10.1016/j.matdes.2015.08.032.

[121] S. Lin, F. Ye, S. Dong, J. Ma, B. Zhang, and J. Ding, "Mechanical, dielectric properties and thermal shock resistance of porous silicon oxynitride ceramics by gas pressure sintering," *Mater. Sci. Eng. A*, vol. 635, pp. 1–5, May 2015, doi: 10.1016/j.msea.2015.03.064.

[122] M. Mitomo, S. Ono, T. Asami, and S. J. L. Kang, "Effect of atmosphere on the reaction sintering of Si2N2O," *Ceram. Int.*, vol. 15, no. 6, pp. 345–350, Jan. 1989, doi: 10.1016/0272-8842(89)90047-3.

[123] X. Zhu and Y. Sakka, "Textured silicon nitride: processing and anisotropic properties," *Sci. Technol. Adv. Mater.*, vol. 9, no. 3, p. 33001, Mar. 2008, doi: 10.1088/1468-6996/9/3/033001.

[124] O. Tapasztó, L. Tapasztó, M. Markó, F. Kern, R. Gadow, and C. Balázsi, "Dispersion patterns of graphene and carbon nanotubes in ceramic matrix composites," *Chem. Phys. Lett.*, vol. 511, no. 4, pp. 340–343, Mar. 2011, doi: 10.1016/j.cplett.2011.06.047.

[125] N. Axén, S. Hogmark, and S. Jacobson, "Friction and wear measurement techniques," in *Modern Tribology Handbook: Volume One: Principles of Tribology*, CRC Press, 2000, pp. 493–510.

[126] C. P. Doğan and J. A. Hawk, "Microstructure and abrasive wear in silicon nitride ceramics," *Wear*, vol. 250–251, no. PART 1, pp. 256–263, Oct. 2001, doi: 10.1016/S0043-1648(01)00649-4.

[127] A. K. Németh and M. B. Maros, “Wear maps and models in tribological damage analysis of Si3N4 ceramics with special attention to tribochemical wear,” 2017, [Online]. Available: https://www.researchgate.net/profile/Alexandra_Nemeth4/publication/322477582_Wear_Maps_and_Models_in_Tribological_Damage_Analysis_of_Si3N4_Ceramics_with_Special_Attention_to_Tribochemical_Wear/links/5a61a79faca272a158175b2d/Wear-Maps-and-Models-in-Tribolo.

[128] A. G. Evans and D. B. Marshall, “WEAR MECHANISMS IN CERAMICS.,” 1981, pp. 439–452.

[129] M. A. Moore and F. S. King, “Abrasive wear of brittle solids,” *Wear*, vol. 60, no. 1, pp. 123–140, Apr. 1980, doi: 10.1016/0043-1648(80)90253-7.

[130] S. F. Wayne, S. T. Buljan, J. G. Baldoni, and M. L. Huckabee, “Microstructural aspects of Si3N4-TiC composites affecting abrasion and erosion resistance,” *Tribol. Trans.*, vol. 34, no. 4, pp. 553–558, 1991, doi: 10.1080/10402009108982069.

[131] T. Yamamoto, M. Olsson, and S. Hogmark, “Three-body abrasive wear of ceramic materials,” *Wear*, vol. 174, no. 1–2, pp. 21–31, May 1994, doi: 10.1016/0043-1648(94)90082-5.

[132] P. Tatarko, M. Kašiarová, J. Dusza, J. Morgiel, P. Šajgalík, and P. Hvizdoš, “Wear resistance of hot-pressed Si3N4/SiC micro/nanocomposites sintered with rare-earth oxide additives,” *Wear*, vol. 269, no. 11–12, pp. 867–874, Oct. 2010, doi: 10.1016/j.wear.2010.08.020.

[133] Z. Kónya, I. Vesselenyi, K. Niesz, A. Kukovecz, A. Demortier, A. Fonseca, J. Delhalle, Z. Mekhalif, J. B.Nagy, A. A. Koós, Z. Osváth, A. Kocsonya, L. P. Biró, and I. Kiricsi, “Large scale production of short functionalized carbon nanotubes,” *Chem. Phys. Lett.*, vol. 360, no. 5, pp. 429–435, Mar. 2002, doi: 10.1016/S0009-2614(02)00900-4.

[134] C. Balázsi, F. Wéber, and P. Arató, “Investigation of C/Si3N4 Nanocomposites,” *Materwiss. Werksttech.*, vol. 34, no. 4, pp. 332–337, Mar. 2003, doi: 10.1002/mawe.200390070.

[135] C. Balázsi, B. Fényi, N. Hegman, Z. Kövér, F. Wéber, Z. Vértesy, Z. Kónya, I. Kiricsi, L. P. Biró, and P. Arató, “Development of CNT/Si3N4 composites with improved mechanical and electrical properties,” *Compos. Part B Eng.*, vol. 37, no. 6, pp. 418–424, Mar. 2006, doi: 10.1016/j.compositesb.2006.02.006.

[136] M. Steen, “Fractography and fracture mechanics property assessment of advanced

structural ceramics," *Int. Mater. Rev.*, vol. 44, no. 5, pp. 165–216, Mar. 1999, doi: 10.1179/095066099101528270.

[137] "(No Title)." https://xgsciences.com/wp-content/uploads/2018/10/xGnP-M-Grade-XG-Sciences.pdf (accessed Aug. 13, 2020).

[138] "nano graphene platelets, http://angstronmaterials.com." .

[139] P. Kun, O. Tapasztó, F. Wéber, and C. Balázsi, "Determination of structural and mechanical properties of multilayer graphene added silicon nitride-based composites," *Ceram. Int.*, vol. 38, no. 1, pp. 211–216, Jan. 2012, doi: 10.1016/j.ceramint.2011.06.051.

[140] J. M. Tour, "Layered materials: Scaling up exfoliation," *Nature Materials*, vol. 13, no. 6. Nature Publishing Group, pp. 545–546, Apr. 20, 2014, doi: 10.1038/nmat3961.

[141] E. L. Corral, H. Wang, J. Garay, Z. Munir, and E. V Barrera, "Effect of single-walled carbon nanotubes on thermal and electrical properties of silicon nitride processed using spark plasma sintering," *J. Eur. Ceram. Soc.*, vol. 31, no. 3, pp. 391–400, Mar. 2011, doi: 10.1016/j.jeurceramsoc.2010.10.020.